

AD-A258 856

①

AFIT/GEP/ENP/92D-1



DTIC  
ELECTE  
JAN 7 1993  
S C D

A TWO-DIMENSIONAL PARTICLE  
SIMULATION OF PARALLEL PLATE  
RADIO-FREQUENCY (RF)  
GLOW DISCHARGES

THESIS

Eric J. Bennett, Captain, USAF

AFIT/GEP/ENP/92D-1

93-00102

Approved for public release; distribution unlimited

93 1 04 158

A TWO-DIMENSIONAL PARTICLE SIMULATION OF PARALLEL PLATE  
RADIO-FREQUENCY (RF) GLOW DISCHARGES

THESIS

Presented to the Faculty of the School of Engineering  
of the Air Force Institute of Technology

Air University

In Partial Fulfillment of the  
Requirements for the Degree of  
Master of Science in Physics

Eric J. Bennett, B.A., M.S.

Captain, USAF

December 1992

Approved for public release; distribution unlimited

DTIC QUALITY INSPECTED 3

Accession For	
NTIS GRA&I	<input checked="checked" type="checkbox"/>
DTIC TAB	<input type="checkbox"/>
Unannounced	<input type="checkbox"/>
Justification	
By	
Distribution/	
Availability Codes	
Avail and/or	
Dist	Special
A-1	

## Preface

The purpose of this research was to develop a two-dimensional particle simulation of the parallel plate RF glow discharges used by industry in plasma assisted processing. The need for this work arises from the recognized lack of understanding regarding the relationships between the external operating parameters and internal processes in the RF glow discharge (Shohet, 1991:726). The National Research Council has recommended that a national initiative be undertaken to increase the level of scientific knowledge regarding RF glow discharge reactors. In particular, the National Research Council has recommended that multi-dimensional models be developed to study the RF glow discharge and aid in future reactor designs (National Research Council, 1991:51).

Since the calculation is computationally intensive, the initial model was developed with the mind set of including only those processes essential for preliminary testing. Initial testing indicates that the model reproduces many of the qualitative features predicted by some of the existing one-dimensional models and theory. Further work is required to gain a more quantitative agreement. As it now stands, the model runs on a computer which limits the duration of a simulation and the number of particles in the simulation (due to memory constraints). Ultimately, the model should be optimized for run-time and ported to a super computer class machine for computer experiments consisting of longer run times and a larger number of particles.

Chapter one provides background on the RF glow discharge and motivates this work by outlining industrial dependence on plasma assisted processing. A specific example in the microelectronics industry is used. Chapter two outlines the various general methods available for RF glow discharge simulation and reviews some previous models. In addition, the simulation method used in this research (particle simulation) is discussed in detail and the specific algorithms used in the model are described. Chapter three provides

the results of some simple test cases which give confidence in the proper operation of portions of the model. Also, the results of initial experiments conducted using the simulation are discussed. Chapter four provides required changes to the model and suggestions for future work.

I would like to thank my thesis advisor Dr. W. F. Bailey for introducing me to this research topic and for his encouragement and assistance. I would also like to thank my committee members, Dr A. Garscadden and Capt M. Stoecker, for their suggestions and comments on this document. As always, much gratitude goes to my wife Cindy for her patience and understanding.

Eric J. Bennett

# Table of Contents

	Page
Preface .....	ii
List of Figures .....	vii
List of Tables .....	xii
Abstract .....	xiii
I. Background and Motivation .....	1
Characteristics of the RF Glow Discharge .....	1
Industrial Plasma Processing .....	6
II. RF Glow Discharge Simulation .....	12
General Methods .....	12
Fluid Method .....	12
Particle Method .....	12
Previous Simulations.....	15
Unresolved Problems .....	16
Ion Anisotropy and Uniformity.....	16
Surface Inhomogenieties.....	16
Gas Chemistry and Surface-Gas Chemistry.....	17
Model Development.....	17
Coordinate System .....	18
Development and Discretization of the Model Equations .....	18
Normalization of the Model Equations .....	22
Solution of Poisson's Equation on the Grid .....	25
Boundary Conditions .....	25
Particle and Field Weighting.....	27
Monte Carlo Collisions.....	28

Initial Particle Loading .....	32
Computer Code .....	33
Input File Format .....	34
Program Compilation, Linking and Execution. ....	36
Output Files. ....	36
<b>III. Model Verification, Experimental Results and Discussion .....</b>	<b>38</b>
Single Particle Test .....	38
Case 1 .....	38
Case 2 .....	39
Experimental Results and Discussion .....	43
Noise Problem .....	43
Experimental Conditions .....	45
One-Dimensional Results .....	47
Two Dimensional Results .....	52
Summary of Results .....	54
<b>IV. Suggestions and Recommendations.....</b>	<b>55</b>
Incorporate a Non-Uniform Radial Grid .....	55
Incorporate Realistic System Boundaries .....	56
Incorporate Accurate Modeling of Collision Kinetics .....	56
Optimize the Code .....	56
Port the Model to a Faster Computer with Large Main Memory .....	57
Include the Effects of an Externally Applied Magnetic Field .....	57
Add External Circuit Elements .....	57
<b>Appendix A</b>	
Electric Field Within a Semi-Infinite Dielectric .....	59
<b>Appendix B</b>	

Sample Input Data File .....	61
Appendix C	
Diagrams .....	62
Bibliography .....	106
Vita .....	109

## List of Figures

Figure	Page
Figure 1.1. Schematic of a typical RF glow discharge .....	62
Figure 1.2.a. Characteristics of the isotropic, wet etched pattern .....	63
Figure 1.2.b. Characteristics of the anisotropic, dry etched pattern.....	63
Figure 1.3. Schematic of the "Reinberg reactor." .....	64
Figure 1.4. Basic plasma assisted etching mechanisms .....	65
Figure 2.1. Computational cycle used in particle simulations with Monte Carlo collisions .....	66
Figure 2.2. Spatial grid used in the model .....	67
Figure 2.3. Volume elements used in forming the charge density .....	68
Figure 2.4. Pictorial representation of the leapfrog integration scheme .....	69
Figure 2.5. Grid with boundaries shown .....	70
Figure 2.6. Boundary at $r = R$ .....	71
Figure 2.7. Diagram used to explain the bilinear and volume weighting schemes .....	72
Figure 2.8. Form of ionization collision cross-section.....	73
Figure 2.9. Form of elastic collision cross-section .....	74
Figure 3.1. Location of electron, grounded electrodes and first four image .....	75
Figure 3.2. Location of an electron, grounded electrodes, and six image charges for single particle test case 2 .....	76
Figure 3.3. Percent difference between analytically calculated and model calculated acceleration vs simulation time-step for single particle test case 2 using bilinear weighting .....	77



Figure 3.4. Normalized z-component of position vs simulation time-step for single particle test case 2 using bilinear weighting .....	78
Figure 3.5. Percent difference between analytically calculated and model calculated acceleration vs simulation time-step for single particle test case 2 using NGP weighting .....	79
Figure 3.6. Normalized z-component of position vs simulation time-step for single particle test case 2 using NGP weighting .....	80
Figure 3.7.a. Potential at the start of the eleventh RF cycle .....	81
Figure 3.7.b. One dimensional slice at constant radius ( $r = 0$ ) of potential shown in figure 3.7.a. ....	81
Figure 3.8.a. Potential for conditions discussed in chapter three with one particle per grid cell .....	82
Figure 3.8.b. Potential for conditions discussed in chapter three with 100 particles per grid cell .....	82
Figure 3.8.c. Potential for conditions discussed in chapter three with 1000 particles per grid cell .....	83
Figure 3.8.d. Potential for particles placed off-axis with 1000 particles per grid cell .....	83
Figure 3.9.a. Potential as a function of position within the discharge at three times between the beginning and one-quarter of the way through the RF cycle .....	84
Figure 3.9.b. Potential as a function of position within the discharge at three times between one-half and three-quarters of the way through the RF cycle .....	84
Figure 3.10.a. Electric field as a function of position within the discharge at three times between the beginning and one-quarter of the way through the RF cycle .....	85

Figure 3.10.b. Electric field as a function of position within the discharge at three times between one-half and three-quarters of the way through the RF cycle .....	85
Figure 3.11.a. Charged particle densities as a function of position in the discharge at the beginning of an RF cycle .....	86
Figure 3.11.b. Charged particle densities as a function of position in the discharge one-eighth of the way through an RF cycle .....	86
Figure 3.11.c. Charged particle densities as a function of position in the discharge one-quarter of the way through an RF cycle .....	87
Figure 3.12.a. Average electron energy as a function of position within the discharge at $\omega t / 2\pi = 0.0$ .....	88
Figure 3.12.b. Average electron energy as a function of position within the discharge at $\omega t / 2\pi = 0.125$ .....	88
Figure 3.12.c. Average electron energy as a function of position within the discharge at $\omega t / 2\pi = 0.25$ .....	89
Figure 3.12.d. Average electron energy as a function of position within the discharge at $\omega t / 2\pi = 0.375$ .....	89
Figure 3.12.e. Average electron energy as a function of position within the discharge at $\omega t / 2\pi = 0.5$ .....	90
Figure 3.13.a. Average ion energy as a function of position within the discharge at beginning of RF cycle .....	91
Figure 3.13.b. Average ion energy as a function of position within the discharge midway through the RF cycle .....	91
Figure 3.14. Ion $z$ - $v_z$ phase space for the left half of the discharge ( $0 \text{ m} \leq z \leq 0.02 \text{ m}$ ) .....	92
Figure 3.15. Average ion energy at the beginning of the RF cycle as a function of position within the discharge for the case with no ion collisions .....	93

Figure 3.16. Ion $z$ - $v_z$ phase space at the beginning of the RF cycle for the case with no ion collisions for the left half of the discharge ( $0 \text{ m} \leq z \leq 0.02 \text{ m}$ ) .....	94
Figure 3.17. Average ion density at the beginning of the RF cycle as a function of position within the discharge for the case with no ion collisions .....	95
Figure 3.18. Electric field at the beginning of the RF cycle for the case with no ion collisions .....	96
Figure 3.19. Plasma density as a function of applied voltage with the fit line $n \propto V_{RF}$ shown .....	97
Figure 3.20. Sheath length (at $wt / 2\pi = 0$ ) as a function of applied voltage .....	97
Figure 3.21.a. Potential as a function of position within the discharge at $wt / 2\pi = 0.25$ for the two-dimensional case .....	98
Figure 3.21.b. Potential as a function of position within the discharge at $wt / 2\pi = 0.5$ for the two-dimensional case .....	98
Figure 3.21.c. Potential as a function of position within the discharge at $wt / 2\pi = 0.75$ for the two-dimensional case .....	99
Figure 3.22. Average ion radial velocity as a function of position within the discharge at the beginning of an RF cycle for the two-dimensional case .....	100
Figure 3.23. One-dimensional radial profile of the potential at constant $z = 3.5 \text{ cm}$ at $wt / 2\pi = 0.25$ for the two-dimensional case .....	101
Figure 3.24. Average ion energy as a function of axial position within the discharge at constant $r = 2.4 \text{ mm}$ at the beginning of an RF cycle for the two-dimensional case .....	102
Figure 3.25. Average ion energy across the left electrode for the two-dimensional case .....	103

Figure 3.26. Average ratio of the radial and axial velocity components for ions at the left electrode ( $z = 0$ ) at the beginning of an RF cycle for the two- dimensional case .....	104
Figure A.1. Diagram referred to in appendix A .....	105

## List of Tables

Table	Page
1.1. Potential Market Values for Plasma Processing .....	7
2.1. Input Data File Description .....	34

**Abstract**

A two dimensional model of parallel plate RF glow discharges was developed to study discharge phenomena important in plasma assisted processing of materials. The particle-in-cell method is used to calculate the trajectories of computer particles under the influence of both self and applied fields. Monte Carlo methods using the null collision technique are used to model collisions between charged particles and neutral gas atoms. Results of computer experiments are presented with special emphasis placed on ion motion in the sheath regions. Experimental results show some qualitative agreement with one-dimensional model results. Further work required to gain quantitative agreement is outlined.

# **A TWO-DIMENSIONAL PARTICLE SIMULATION OF PARALLEL PLATE RADIO-FREQUENCY (RF) GLOW DISCHARGES**

## **I. Background and Motivation**

Beyond pure scientific curiosity, why study the RF glow discharge? The answer is -- major manufacturing industries have become increasingly dependent upon the RF glow discharge for a wide variety of materials processing techniques (National Research Council, 1991:4-5). Furthermore, basic scientific knowledge of the discharge is seriously lagging the need for technology development. This chapter introduces the physical properties of the RF glow discharge and establishes the growing dependence of industry on plasma processing, as well as the need for increased scientific understanding of RF glow discharge phenomena (specifically, the requirement for multi-dimensional computer models).

### **Characteristics of the RF Glow Discharge**

The typical parallel plate RF glow discharge is shown in figure 1.1 (Flamm and Herb, 1989:14-17). Flamm and Herb provide a good overview of some of the major characteristics of the RF glow discharge. A gas at low pressure (typically ten mtorr to one torr) is introduced into the space between two parallel plate electrodes. A plasma is produced via the application of RF power through the electrodes. The electrodes are typically driven at the industry standard frequency of 13.56 MHz and a peak voltage of a few tens to one thousand volts. The plasma consists of a weakly ionized gas with approximately one charged particle for every  $10^5$  -  $10^6$  neutrals. The applied RF power is the source of energy for the production of charged particles. The charged species consist

of heavy, relatively immobile positive ions (the positive charge carriers) and light, highly mobile electrons (the negative charge carriers), although some plasmas contain negative ions.

Flamm and Herb also describe the two distinct spatial regions which form in the RF glow discharge (Flamm and Herb, 1989:15-17). The majority of the discharge is electrically neutral (the plasma bulk), consisting of approximately equal numbers of positive and negative charges with a number density of  $10^{15} - 10^{18} \text{ m}^{-3}$ . The other region of the discharge is formed between the bulk plasma and any surface which comes into contact with the plasma such as the walls of the discharge tube and the electrodes. These are known as sheath regions. The formation of the sheath which forms between the plasma bulk and the radially bounding glass wall can be described as follows: in the sheath region diffusion of charged particles to the bounding surface severely reduces the charged particle densities. Since the electrons diffuse faster than the ions (owing to their much smaller mass and higher mobility), a net positive space charge region is left behind which forms an electric field that promotes ion diffusion and retards further electron diffusion. Eventually the electrons and ions diffuse to the wall at an equal rate. The potential difference associated with the radial sheath is much smaller than that of the axial sheath which forms between the electrodes and the plasma bulk. Due to the depletion of electrons in the sheath regions, the sheaths are poor conductors as compared to the charge rich plasma bulk. This situation leads to large potential differences across the axial sheaths. In fact, "most of the potential drop appears across the sheath" (Flamm and Herb, 1989:17). Since the sheath region is narrow, it is characterized by high electric field strengths as compared to the bulk.

The axial sheath regions play an important role in the RF glow discharge. The sheaths that form between the electrodes and the plasma bulk in an RF glow discharge vanish and reform once during each RF cycle due to the application of a time varying



voltage to one of the electrodes. This sheath motion imparts energy to the charged particles. Since the ions are much heavier than the electrons, they are unable to respond to the instantaneous potential at high driving frequencies -- the heavy ions respond to a time-averaged potential. Thermal ions entering the sheath are accelerated by the time-average sheath electric field towards the electrode until they consequently strike the electrode. The lighter electrons respond much differently to the time-varying sheath which imparts large amounts of energy to the electrons.

Boeuf and Belenguer explain that electrons can gain energy from the plasma sheath by any of three mechanisms (Boeuf and Belenguer, 1990:164 - 166). Depending upon the discharge conditions any one of these mechanisms may be the dominant one. One way in which electrons gain energy from the sheath is by secondary electron emission due to ion bombardment (Boeuf and Belenguer, 1990: 166). When an ion strikes an electrode a secondary electron may be emitted. This secondary electron created at the surface of the electrode is accelerated through the large sheath field away from the electrode and towards the central region of the plasma. These secondaries enter the bulk with high energies.

A second manner in which electrons gain energy is through what Kushner terms "wave riding" (Kushner, 1986: 188). As described above, during a portion of the RF period the sheath contracts, allowing some higher energy bulk electrons to gain access to the sheath region where they are subsequently pushed back into the bulk as the sheath reforms. The electrons that intrude upon the sheath region may reach high energies as they "surf" on the expanding sheath back to the bulk (Boeuf and Belenguer, 1990: 166).

Lastly, the sheath imparts energy to the electrons through electron-sheath collisions (Boeuf and Belenguer, 1990: 166). As the sheath expands away from the electrode the electrons traveling towards the electrode are reflected by the moving sheath and thus gain energy much as a ping-pong ball would after being struck by a paddle. Vendor and

Boswell provide a simple calculation based on their numerical data and a hard wall model which illustrates the degree of electron energy gain in electron-sheath collisions. In this model of electron-sheath collisions, the resulting velocity of an electron incident upon the moving sheath is given by (Vender and Boswell, 1990:728):

$$v_{electron,final} = -v_{electron,initial} + 2 v_{sheath} \quad (1.1)$$

From their simulation they found a maximum sheath velocity of approximately  $2 \times 10^6$  m/s and the velocity of a thermal electron incident upon the sheath of approximately  $10^6$  m/s (about 3 eV). Using equation 1.1 they found that the incident electron is accelerated to a velocity of approximately  $5 \times 10^6$  m/s. This corresponds to a final energy of roughly 70 eV (Vender and Boswell, 1990:728). This provides a simple numerical example of the role of the sheath and electron energy gain -- one can see that the sheath imparts large amounts of energy to the electrons. This energy is then redistributed within the discharge by electron-neutral collisions. It will be shown below that, through this energy redistribution, the electrons convert "electric power into chemical power" by way of ionization, excitation, and dissociation resulting from the electron-neutral collisions (Boeuf and Belenguer, 1990: 155). This energy conversion is fundamental to many plasma processing applications, but before moving into this area an overview of the various mechanisms for energy deposition within the discharge is warranted.

The electric field resulting from applied RF power imparts energy to charged particles through the methods outlined above. Since the electrons are lighter, they are primarily responsible for the redistribution of the energy within the discharge (Gill and Donaldson, 1931:723). This redistribution takes the form of electron-neutral collisions which may be either elastic or inelastic (Flamm and Herb, 1989:23). The type of any particular collision depends upon the gas involved and the electron energy.

In an elastic collision, the sum of the kinetic energy of the two constituent particles remains a constant before and after the collision (Goldstein, 1980:117). In electron-

neutral elastic collisions a small amount of energy is transferred from the fast electron to the slow neutral particle. On average, this energy is approximately given by :

$$E_{transferred} \approx \frac{2 m_e}{M_n} \Delta E \quad (1.2)$$

where  $\Delta E$  is the initial energy difference,  $m_e$  is the electron mass, and  $M_n$  is the neutral particle mass (McDaniel, 1964:24). Since  $m_e \ll M_n$ , the amount of energy transferred in any individual electron-neutral elastic collision is very small. Thus, the electron-neutral elastic collision is an inefficient energy transfer mechanism (Flamm and Herb, 1989:22). This stated, elastic collisions are still important in the characteristics of the discharge. First, although electron-neutral elastic collisions are inefficient, the energy loss suffered by electrons in this mechanism may be significant, since they can occur most frequently in a discharge (depending upon gas type and operating conditions). Secondly, elastic collisions also transfer momentum. This tends to randomize the motion of the electrons, further increasing their importance to the characteristics of the discharge.

In an inelastic collision, the total kinetic energy of the two particles is not conserved (Goldstein, 1980:117). In electron-neutral inelastic collisions electron kinetic energy goes into changing the internal state of the neutral particle. Since this energy can be quite large, this is often an efficient mechanism for electron energy redistribution. Electron-neutral inelastic collisions describe a wide class of collisions which include ionization, excitation, and dissociation. In this manner, "electron energy, channeled into electron-neutral inelastic collisions, maintains the supply of ions and radical species" in the discharge (Flamm and Herb, 1989:26). The ions and radical species are the chemical agents used in many plasma processing applications (Flamm and Herb, 1989:26).

In electron-neutral impact ionization, an electron provides the energy required to ionize the neutral particle by removing an electron from the neutral, creating an electron and a positive ion. Any electron with kinetic energy greater than the ionization potential

which collides with a neutral gas particle has a chance of ionizing that neutral particle. The electron loses kinetic energy in the process. The electrons that have gained energy from the electric field, as described above, provide this energy to ionization in order to sustain the discharge, creating more electrons and ions which are continually lost to the electrodes and walls of the discharge. As it will be shown below, the ions which are lost to the electrodes are important in many plasma processing applications. In this manner, the electrons provide an energy conversion and transport mechanism, converting electrical energy from the field into the energy required to create new charged particle species.

New particle species are also created via dissociation. In this type of electron-neutral inelastic collision the electron provides the energy required to produce potentially chemically reactive species. Again, these particles are important in many plasma processing applications, providing the plasma chemistry to perform the desired process.

In an electron-neutral inelastic collision that results in excitation, the neutral particle is excited to a higher energy level. The electron supplies the energy required to excite the neutral. This collision process is important in reactors where photons play an important role in the either plasma processing or as a diagnostic means for process control, since the excited state neutrals ultimately decay to a lower energy state, thereby emitting a photon in the process.

Some of the general characteristics of the RF glow discharge have been reviewed. Next, the dependence of industry on plasma processing will be established, as well as the need for an increase in the scientific understanding of these devices in order to optimize their use and aid in future reactor designs.

### **Industrial Plasma Processing**

The National Research Council reports that the following industries rely heavily on plasma processing of one sort or another: national defense, aerospace, optics, solar

energy, telecommunications, textile, paper, waste management, biomedicine, automobile, and microelectronics industries (National Research Council, 1991:9). Shohet emphasizes the importance of plasma processing in industry by estimating the dollar amounts associated with the potential markets for some of the most important industrial applications. A summary of his estimates are shown in table 1.1 (Shohet, 1991:725).

<u>Application</u>	<u>Dollar Value (\$ billion)</u>
Metal Corrosion Protection	50
Plasma Electronics	40
Semiconductor Processing	26
High-Performance Ceramics	5
Tool and Die Hardening	2

**Table 1.1.** Current and Potential market values for plasma processing (Shohet, 1991:725).

The microelectronics industry is perhaps the most dependent on plasma processing for the production of computer chips. One specific example of the microelectronics industry's dependence on plasma assisted processing given by the National Research Council is the construction of the metallic connections on an integrated circuit. This process is comprised of the following steps (all of which depend upon plasma processing to some degree): (1) deposition of a layer of metal on a substrate, (2) application of a pattern on the metal layer (the mask), (3) removal of the metal not covered by the mask leaving the desired connections, and (4) removal of the mask. Step 3, the etching process, is absolutely dependent on plasma processing and serves well to illustrate the need for an increased scientific understanding of RF glow discharge phenomena.

The National Research Council provides a contrast between chemical etching and plasma-assisted etching. Prior to the advent of plasma-assisted etching, reactive chemicals were used to remove the material not protected by the mask (so called "wet" etching). Unfortunately, as the chemical removes the unprotected material, the material underneath the mask is exposed to the chemical and is also etched away causing the etched pattern to take on the appearance in figure 1.2.a. This feature of wet etching is highly undesirable, especially as the size of integrated circuits decrease. Only plasma assisted etching (so called "dry" etching) is capable of producing the high fidelity pattern transfer required for today's devices. Figure 1.2.b contrasts the capability of dry etching over wet etching. The sharp right angle etching shown in figure 1.2.b is referred to as anisotropic etching. The process responsible for this feature will be explained when the etching mechanisms are presented.

Flamm and Herb describe an early parallel plate RF glow reactor patented by Reinberg in 1975 (Flamm and Herb, 1989:65-66). Figure 1.3 shows a schematic of the "Reinberg style reactor." The wafers are placed on the lower electrode, which may be heated or cooled to enhance the chemistry of the particular plasma processing at hand. This system was originally used as a chemical vapor deposition reactor, and is now one of the most common types used in industry.

In his doctoral dissertation, Barnes describes the major categories of plasma assisted etching processes (Barnes, 1988:14-16). They are categorized by the particles responsible for the etching process and, therefore, provide a good introduction to the basic mechanisms of plasma assisted etching. The major categories are: *neutral free radical etching*, *ion-assisted etching*, and *sputter etching* (Barnes, 1988:14-16).

In *neutral free radical etching*, free radicals formed by dissociation in the discharge chemically react with the wafer. This chemical reaction forms a volatile product and results in an etched surface. Note that this is similar to straight chemical etching without

a plasma -- depending upon crystal orientation, there may not be a preferential direction of the etching process so that the resulting etch pattern resembles those found in figure 1.2.a (Barnes, 1988:14).

*Ion-assisted etching* is broken into two subcategories: *ion-assisted free radical etching* and *chemically enhanced sputter etching*. In *ion-assisted free radical etching* the same type of process responsible for chemical etching is at work, the difference being that energetic ions supply "activation energy" which enhances the chemical reaction (Sommerer, 1992: 2). This is the basis for the anisotropic etch patterns shown in figure 1.2.b. The highly anisotropic ions (with velocities primarily directed perpendicular to the electrode surface due to the strong axial sheath fields) promote etching in the direction perpendicular to the electrode surface. Anisotropic etches are also a feature of *chemically enhanced sputter etching*, although here the ions perform most of the work by physically knocking surface atoms off the wafer. In this type of etching, chemically reactive species tend to prepare the surface (via surface heating or bond breaking, for example) so as to make it easier for the ions to do their job. This reduces the requirement for high energy ions which helps reduce the potential for damage to the wafer (Barnes, 1988:15).

Lastly, straight *sputter etching* employs the use of highly energetic (approximately 500 eV) ion bombardment to dislodge surface atoms from the wafer (Barnes, 1988:15). This type of etching also results in the desirable anisotropic etching. One problem with this mechanism is that the high energy ions can result in surface damage to the wafer.

Flamm and Herb provide a diagram (shown in figure 1.4) which summarizes the plasma assisted etching mechanisms described above. Now that the basic mechanisms of plasma assisted etching have been outlined, a review of the major features of plasma etching which one would like to control will help to establish the need for an increased scientific understanding of the discharge.

The National Research Council explains that in any plasma etching process, one would like to control the following characteristics (among other things): *anisotropy*, *selectivity*, *damage*, and *uniformity* (National Research Council, 1991:21-23). As mentioned above, *anisotropy* refers to the type of etching shown in figure 1.2.b. This type of etch is made possible by the presence of highly directional energetic ions which enhance the chemical reaction or dislodge surface atoms. Since the ions are accelerated through the high sheath field toward the electrode, controlling the structure of the plasma sheath is a prerequisite for controlling ion anisotropy. Therefore, scientists would like to determine the sheath structure as a function of operating parameters.

*Selectivity* refers to the desire to remove the etch layer while leaving the mask undamaged. Scientists recognize the fact that selectivity depends upon both ion energy and surface chemistry in ion-assisted etching. However, a trade-off exists between selectivity, anisotropy, and *damage* -- if the same ions that foster anisotropy are too energetic the result is a lack of selectivity, not to mention the potential for damage to the wafer due to the high energy ions.

Lastly, *uniformity* refers to the ability to etch over a wide area at the same rate. This ability depends upon controlling the uniformity of ion flux (which, it has been pointed out, depends upon the sheath structure). This may be further complicated by localized effects. For instance, the specific structure of an individual wafer or the structure of a piece of a single wafer may change the etch rate from wafer to wafer or across a single wafer.

The next logical question is, since we are aware of some of the characteristics that influence the quality of plasma etching (and, in general, any plasma assisted process), how can these characteristics be controlled? Sommerer describes the dilemma plasma processing practitioners find themselves in when trying to influence some of the factors outlined above:



The reactor conditions may be optimized for the desired process by varying the fill gas mixture, flow, pressure, applied voltage, electrode sizes, and substrate temperature. Unfortunately, typical plasma discharges tend to respond in a highly complicated way to adjustments of any one of these parameters. It is therefore difficult to adjust, for example, the ion flux to the wafer or substrate without also affecting the neutral radical flux. This complex interaction stymies intuitive attempts at process optimization, and motivates much of the effort to develop more rigorously-based models (Sommerer: 1992:2).

Shohet points out that "the key to further advances in plasma-aided manufacturing" is the understanding of the complex relationship between the external operating parameters and (in the case of plasma assisted etching) the characteristics described above (Shohet, 1991: 726). To date, trial-and-error has been the method used when attempting to influence many plasma processes (Sommerer, 1992:1). In light of the important role plasma assisted processing plays in industry, the National Research Council has recommended a plan of action to remedy this situation (National Research Council, 1991). Paramount in this plan is the development of multi-dimensional computer models of plasma reactors in order to determine the relationships between external operating parameters and plasma processing mechanisms (National Research Council, 1991:51).

## II. RF Glow Discharge Simulation

### General Methods

In general, there are two primary methods for simulating the RF glow discharge: the fluid method and the particle method. This section briefly discusses the major features of each. Variations of these basic methods exist, as well as methods which combine features of both. These techniques are not discussed here.

**Fluid Method.** Boeuf and Belenguer describe the fluid method which they have used to study the RF glow discharge. In the fluid method the modeler begins by taking a finite number of successive velocity moments of the Boltzmann equation in order to find the time progression of the discharge particle species. Particle species movement within the discharge is accomplished via the use of average quantities obtained from the moment equations. Assumptions and approximations regarding the velocity distribution function of each species must be made in order to close the system of equations (Golant and others, 1980:Ch 6).

One of the major disadvantages of this method is the validity of making apriori assumptions regarding the particle velocity distribution functions. Another short coming of this approach is the inability to predict the non-local effects important in RF glow discharges. Surendra and Graves provide an example (Surendra and Graves, 1991:148). In their particle simulation of a one dimensional RF discharge in helium they observed that the peak electron heating rate and ionization rate did not occur at the same point in the discharge due to the long mean free path for electron-neutral collisions. They point out that fluid models are hard pressed to predict this type of non-local behavior. Nevertheless, fluid model results similar to those found by way of particle based methods have been obtained in much shorter computer run-times (Sommerer, 1992:8).

**Particle Method.** In the particle method (sometimes referred to as the particle-in-cell (PIC) method for reasons that will become apparent) the trajectories of computer particles

(called super particles) representing many real particles are simulated (Sommerer, 1992:4). The particle method makes use of a spatial and temporal grid. The basic computational cycle is shown in figure 2.1 (Birdsall, 1991:81). In this method Maxwell's equations are used to solve for the fields generated by the charged particles and the applied voltage on the electrodes. Given the fields, the Newton-Lorentz equation of motion is then used to update the trajectories of the charged particles (Birdsall, 1991:65). As noted in chapter one, charged particle collisions are important in RF glow discharges. Collisions with neutral atoms are incorporated via the Monte Carlo method. The fact that the particle motion and calculation of the fields is self-consistent is an attractive feature of particle simulation -- it "allows the model to 'make up its own mind' about the nature of its macroscopic and collective behavior" (Hockney, 1966:1826). Note that by using Maxwell's equations and a spatial grid, the requirement of calculating the force on each charged particle due to every other charged particle and the electrodes is negated -- a computationally impossible task for even a moderate number of particles (Birdsall and Langdon, 1991:9). Furthermore, in simulating the discharge we are interested in the collective behavior of the plasma down to the plasma's characteristic length, the Debye length. By using the spatial grid the unwanted detail (not to mention the trouble associated with singularities as the distance between particles approaches zero) is not calculated (Birdsall and Langdon, 1991:9). The spatial grid is used to calculate the charge and current densities and corresponding fields while the temporal grid is used to advance the simulation from time-step to time-step. Both grids must be of sufficient resolution (small enough spacing between successive grid points) to maintain numerical accuracy in the simulation. Furthermore, the spatial grid must be fine enough to at least resolve a Debye length, while the time-step size must be small enough to resolve the electron plasma frequency (Hockney and Eastwood, 1988:32, 39, 333-334). It is

important to note that the fields are "grid quantities" while the particle positions may take on continuous values.

Referring to figure 2.1, the particle method consists of five major calculations (Birdsall, 1991:81):

- (1) Weight the particles to the spatial grid to form the densities;
- (2) Calculate the fields at each grid point given the densities on the grid;
- (3) Weight the fields to the particle locations to find the force on each particle;
- (4) Update the particle positions and velocities given the force on each particle;
- (5) Collide charged particles with neutrals.

In figure 2.1 the quantities on the left-hand side of the arrow are transformed by the calculation into the quantities on the right-hand side of the arrow. The subscript  $k$  refers to the  $k_{th}$  particle, while the subscript  $j$  refers to the  $j_{th}$  grid point. Note that a particle's position is not updated as a result of a collision -- only its velocity is changed. The series of computations is carried out once per time-step.

As one can see from the description of the particle method its major advantage is that very little must be assumed in the design of the model -- the electric fields, particle production and loss, and particle motion are calculated using first principles. As alluded to in the description of the fluid method, particle simulations are computationally intensive. In fact, this is their major disadvantage. This disadvantage is becoming less prohibitive as computer speed increases, although at this time parameter studies of two dimensional particle models on all but the fastest of today's computers are impractical. However, this does not preclude the need for two dimensional particle models of RF discharges. At this time, a two dimensional particle model's use will probably be confined to a limited number of runs in order to "double check" fluid model results, validate assumptions and approximations made in the fluid models, or as part of a hybrid model combining features of both methods. Another disadvantage of the particle method

is numerical heating. In order to reduce the computation times it is tempting to reduce the number of simulation particles -- this leads to artificial heating of the charged particles due to noise in the charge density, potential, and electric field.

### **Previous Simulations**

To date, the vast majority of RF glow discharge simulations have been in one spatial dimension (although a number of initial papers on two-dimensional models were included in the technical program of the 45th Annual Gaseous Electronics Conference, 26 - 29 October, 1992). This section will outline a few of them.

Boeuf and Belenguer simulated one-dimensional RF glow discharges in helium, nitrogen, and chlorine using the fluid method (Boeuf and Belenguer, 1990:159). They made observations regarding the electric field, charged particle densities, current densities, and plasma potential at various points in an RF cycle for various discharge conditions and geometries. Special emphasis was put on characterizing the mechanisms responsible for sustaining the discharge (as discussed in chapter one) for various discharge conditions. Boeuf and Belenguer used a "two electron group fluid model." In this method, two separate groups of electrons are governed by their own set of (coupled) moment equations. One group represents the "beam electrons" which gain high energy from the sheath field and the other represents the slower bulk electrons in the center of the discharge (Boeuf and Belenguer, 1990:158).

Surendra and Graves simulated one-dimensional parallel plate RF glow discharges in helium using the particle method with Monte Carlo collisions (Surendra and Graves, 1991). They also made observations regarding the discharge sustaining mechanisms (Surendra and Graves, 1991:146-150). A result of their simulation runs are electron and ion energy and velocity distribution functions for various discharge conditions.

Vender and Boswell simulated one-dimensional parallel plate RF glow discharges in an atomic hydrogen-like gas using the particle method with Monte Carlo collisions

(Vender and Boswell, 1991). They found that the scaling of the sheath length and number density with applied voltage was consistent with the Child-Langmuir relation, namely

$$d_s \propto V_s^{\frac{3}{4}} n_e^{-\frac{1}{2}} \quad (2.0)$$

where  $d_s$  is the sheath length,  $V_s$  is the maximum voltage across the sheath, and  $n_e$  is the electron density. In their simulation, they found that the sheath length was practically independent of applied RF voltage, so that  $n_e \propto V_s^{\frac{3}{2}}$ . They also obtained electron and ion energy distribution functions as a result of their calculation. This work was based on a previous model by Boswell and Morey (Boswell and Morey, 1987).

### **Unresolved Problems**

There are many unresolved problems concerning RF discharge reactors (in terms of their application to plasma processing) which have not yet been fully addressed by either particle or fluid models. Some of these problems require multidimensional models and are thus model limited since multidimensional RF discharge models are only now beginning to be developed. Other problems are data limited where basic cross-section and gas chemistry data is required. A few of these unresolved problems are discussed below.

**Ion Anisotropy and Uniformity.** The characteristics of the ion flux to electrodes is of paramount importance since they play a pivotal role in plasma processing. In order to examine the effects of bounding surfaces (container walls) on the uniformity of the ion flux across an electrode surface or the anisotropy of ions bombarding a surface, a two dimensional model is required. Also of interest is the ratio of radial ion flux to axial ion flux. This requires a two-dimensional model.

**Surface Inhomogeneties.** Studying the effects of the macroscopic (wafer-electrode) and microscopic (within an individual wafer) surface inhomogeneties on plasma

processing characteristics requires at least a two-dimensional model. Differences in the secondary emission coefficient of the wafer and electrode and a change in the boundary conditions on the potential due to the presence of the wafer have not yet been investigated. Likewise, the microstructure of the wafer affects the boundary conditions on the potential, thus altering the fields and the plasma processing characteristics of the discharge. A two dimensional model is required to study these effects.

**Gas Chemistry and Surface-Gas Chemistry.** In general, current simulations do not model the neutral gas chemistry (not to mention the more complicated gases used in the plasma processing) nor do the current simulations model surface-gas chemistry. For instance, much is unknown about the role of excited state neutrals in the discharge. Some of the limitation in this case is model limited and requires the incorporation of neutral particle diffusion models into the charged particle codes and some may be data limited for some gases where collision cross-sections may be unknown.

### **Model Development**

The particle method with Monte-Carlo collisions was chosen for this research. Although the inherently long computer runs are unattractive, a particle model is perhaps the easiest way to get started in the simulation of RF discharges due to the straightforward modeling techniques and the lack of uncertainty regarding the validity of assumptions and approximations required in the fluid method. Ultimately, a suite of models consisting of particle models (single and multidimensional) and fluid models (single and multidimensional) is an ideal goal. Thus, the particle models can be used to test the validity of the assumptions made in the fluid models. On the other hand, the fluid model can be used to perform parameter studies which may be impossible to do with the particle model. Both models can be used to check to the results of the other. Also, hybrid particle-fluid models may be possible. The determination of how to partition the

model can be based on either particle species or discharge region (sheath vs. bulk), depending upon which is more suitable to either method.

**Coordinate System.** Given the decision to use the particle method, the next step in designing the simulation is the choice of coordinate system. In order to address topics such as those outlined in chapter one (anisotropy, uniformity, etc.) a multidimensional model is required. The cylindrical discharges shown in figure 1.1 and 1.4 suggest that cylindrical coordinates are an appropriate choice. Therefore, two-dimensional (2D) cylindrical coordinates ( $r$ - $z$ , no theta variations) were chosen. This coordinate system is attractive in two respects. First, it allows one to study the radial variations across the electrodes (for studying anisotropy and uniformity) while also being able to compare the axial variations to existing one-dimensional models. Secondly, this coordinate system serves as a good starting point towards a full three-dimensional particle simulation of cylindrical parallel plate discharges.

The particle shape in a particular coordinate system is conceptually important in the development of the model equations. As an example, take one-dimensional cylindrical coordinates in  $r$  only (no  $z$  or theta variations). The particle shapes are infinite uniform cylindrical shells, centered on  $r = 0$  (Birdsall and Langdon, 1991:332). Particle motion corresponds to a change in the radius of this infinite cylinder of charge. In the coordinate system chosen for this model, the particle shapes are uniform rings of charge (Birdsall and Langdon, 1991:333). Particle motion consists of a combination of axial motion and a change in the radius of the ring of charge.

**Development and Discretization of the Model Equations** (Hockney and Eastwood, 1988:26-32, 305-309). The next step in the development of the model is the discretization of the pertinent equations. Hockney and Eastwood provide a method for doing so. Once the applicable set of equations has been developed the particular algorithms for solving the equations will be described. As stated above, Maxwell's



equations are used to solve for the fields and the Newton-Lorentz equation of motion is used to advance the velocity and position of the particles given the fields. Maxwell's equations are solved for the fields given the charge and current densities:

$$\text{div } \vec{B} = 0 \quad (2.1.a)$$

$$\text{curl } \vec{B} = \mu_0 \vec{j} + \frac{1}{c^2} \frac{\partial \vec{E}}{\partial t} \quad (2.1.b)$$

$$\text{div } \vec{E} = \frac{\rho}{\epsilon_0} \quad (2.1.c)$$

$$\text{curl } \vec{E} = -\frac{\partial \vec{B}}{\partial t} \quad (2.1.d)$$

where  $\vec{B}$  and  $\vec{E}$  are the magnetic and electric field vectors, respectively,  $\rho$  is the charge density, and  $\vec{j}$  is the current density. The force on a particle of charge  $q$  and mass  $m$  under the influence of both magnetic and electric fields is given by the Newton-Lorentz equation of motion:

$$\vec{F} = m \frac{d\vec{v}}{dt} = q (\vec{E} + \vec{v} \times \vec{B}) \quad (2.2)$$

where  $\vec{v}$  is the particle's velocity. Equation 2.2 can then be integrated to solve for the particle's trajectory.

In the electrostatic plasma approximation, the magnetic field due to the moving charges is assumed small so that Maxwell's equations reduce to Poisson's equation:

$$\nabla^2 \phi = -\frac{\rho}{\epsilon_0} \quad (2.3)$$

where  $\phi$  is the electrostatic potential. The electric field is then given by:

$$\vec{E} = -\text{grad } \phi \quad (2.4)$$

The particle trajectories can be computed by integrating:

$$m \frac{\partial \bar{v}}{\partial t} = q \bar{E} \quad (2.5)$$

and

$$\frac{\partial \bar{x}}{\partial t} = \bar{v} \quad (2.6)$$

Equations 2.3 through 2.6 are the model equations which must be discretized for solution on the computer. In the chosen coordinate system Poisson's equation takes on the following form:

$$\frac{1}{r} \frac{\partial}{\partial r} \left( r \frac{\partial \phi}{\partial r} \right) + \frac{\partial^2 \phi}{\partial z^2} = - \frac{\rho(r, z)}{\epsilon_0} \quad (2.7)$$

An approximate solution to equation 2.7 can be obtained on a spatial grid with uniform grid spacing  $\Delta r$  and  $\Delta z$  ( $\Delta r \neq \Delta z$ ) via the following centered finite difference equation (Swarztrauber and Sweet, 1975:45):

$$\begin{aligned} & \frac{1}{(\Delta r)^2 r_i} \left\{ \left( r_i + \frac{\Delta r}{2} \right) (\phi_{i+1,j} - \phi_{i,j}) - \left( r_i - \frac{\Delta r}{2} \right) (\phi_{i,j} - \phi_{i-1,j}) \right\} + \\ & \frac{1}{(\Delta z)^2} \{ \phi_{i-1,j} - 2 \phi_{i,j} + \phi_{i,j+1} \} = - \frac{\rho_{i,j}}{\epsilon_0} \end{aligned} \quad (2.8)$$

The continuous variables of equation 2.7 have been replaced by their discrete counterparts. The potential and charge density are now grid quantities indexed by grid point. The index  $i$  refers to  $r$  grid points and the index  $j$  refers to  $z$  grid points. The grid is shown in figure 2.2. Specific software for solving equation 2.8 is discussed below.

The right hand side of equation 2.8 is formed by weighting the charge from the continuous particle positions to the spatial grid. Next, the charge weighted to the grid is divided by the appropriate volume element to form the charge density at the grid points. The notation used here is similar to that used by Hockney and Eastwood in the development of a one-dimensional periodic plasma model (Hockney and Eastwood, 1988:31). The weighted charge at each grid point can be expressed as:

$$\rho_{i,j} = \frac{q N_s}{V_{i,j}} \sum_{k=0}^{N_p} W(r_k, z_k, r_i, z_j) \quad (2.9)$$

where  $q$  is the particle's charge,  $N_s$  is the number of "real" charged particles per computer (or super) particle,  $N_p$  is the total number of particles, and  $W(r_k, z_k, r_i, z_j)$  is some function which weights the charge at the particle positions  $(r_k, z_k)$  to the grid positions  $(r_i, z_j)$ . In practice, the sum over all particles in equation 2.9 is generally done only over those particles in the grid cells centered on the grid point  $(i, j)$ . Specific methods for doing the charge weighting are discussed below. The divisor in equation 2.9 is the volume of a grid cell centered on grid point  $(i, j)$  (Birdsall and Langdon, 1990:333-334). In 2D  $r$ - $z$  cylindrical coordinates the volumes are rings  $\Delta z$  by  $\Delta r$ . Referring to figure 2.3, for  $i \neq 0$  the volume elements are given by:

$$V_{i,j} = 2 \pi r_i (\Delta r)(\Delta z) \quad (2.10)$$

and for  $i = 0$ ,

$$V_{0,j} = \frac{\pi}{4} (\Delta r)^2 (\Delta z) \quad (2.11)$$

Once the potential is found on the grid, the electric field components can be found by finite differencing equation 2.4 which, in our coordinate system, takes on the form:

$$\begin{aligned} E_r &= -\frac{\partial \phi}{\partial r} \\ E_z &= -\frac{\partial \phi}{\partial z} \end{aligned} \quad (2.12)$$

Equations 2.12 have the following centered finite difference approximations (Hockney and Eastwood, 1988: 30):

$$\begin{aligned} E_{r,i,j} &= \frac{\phi_{i-1,j} - \phi_{i+1,j}}{2(\Delta r)} \\ E_{z,i,j} &= \frac{\phi_{i,j-1} - \phi_{i,j+1}}{2(\Delta z)} \end{aligned} \quad (2.13)$$

Now that the field equations have been put in their discrete forms, a method for integrating the equations of motion must be decided upon in order to discretize the equations of motion (equations 2.5 and 2.6). The leapfrog finite difference approximation offers an efficient way to integrate equations 2.5 and 2.6 (Hockney and Eastwood, 1988:28). It is called the leapfrog method because the position and velocity are known at alternating half time-steps as shown in figure 2.4 (Birdsall and Langdon, 1991:13). The positions and forces on the particles are known at integer time-steps while the particle velocities are known at half time-steps. The particle positions and velocities are updated via (Hockney and Eastwood, 1988:32):

$$\begin{aligned}
 v_{r,k,t+\frac{1}{2}} &= v_{r,k,t-\frac{1}{2}} + \frac{F_{r,k,t}(\Delta t)}{N_s m_k} \\
 v_{z,k,t+\frac{1}{2}} &= v_{z,k,t-\frac{1}{2}} + \frac{F_{z,k,t}(\Delta t)}{N_s m_k} \\
 r_{k,t+1} &= r_{k,t} + v_{r,k,t+\frac{1}{2}}(\Delta t) \\
 z_{k,t+1} &= z_{k,t} + v_{z,k,t+\frac{1}{2}}(\Delta t)
 \end{aligned} \tag{2.14}$$

where  $k$  is the particle index,  $\Delta t$  is the size of the time-step,  $t$  is the time-step index, and  $F$  is the force on the particle. Note that since the force is known on the grid, it must be weighted back to the particle (with the same weighting used for forming the charge density).

#### **Normalization of the Model Equations** (Hockney and Eastwood, 1988:33 - 34).

Now that the model equations have been discretized, some simplifications can be made by the introduction of dimensionless and normalized variables. Starting with the leapfrog equations of motion, if one introduces the following dimensionless variables (tilded quantities are either dimensionless or normalized):

$$\begin{aligned}
\tilde{r} &= r / \Delta r \\
\tilde{z} &= z / \Delta z \\
\tilde{t} &= t / \Delta t \\
\tilde{v}_r &= v_r (\Delta t) / \Delta r \\
\tilde{v}_z &= v_z (\Delta t) / \Delta z \\
\tilde{a}_r &= \frac{F_r (\Delta t)^2}{N_s m (\Delta r)} \\
\tilde{a}_z &= \frac{F_z (\Delta t)^2}{N_s m (\Delta z)}
\end{aligned} \tag{2.15}$$

where  $\tilde{a}_r$  and  $\tilde{a}_z$  are dimensionless acceleration components, the equations of motions simplify to (Hockney and Eastwood, 1988:33):

$$\begin{aligned}
\tilde{v}_{r,k,t+\frac{1}{2}} &= \tilde{v}_{r,k,t-\frac{1}{2}} + \tilde{a}_{r,k,t} \\
\tilde{v}_{z,k,t+\frac{1}{2}} &= \tilde{v}_{z,k,t-\frac{1}{2}} + \tilde{a}_{z,k,t} \\
\tilde{r}_{k,t+1} &= \tilde{r}_{k,t} + \tilde{v}_{r,k,t+\frac{1}{2}} \\
\tilde{z}_{k,t+1} &= \tilde{z}_{k,t} + \tilde{v}_{z,k,t+\frac{1}{2}}
\end{aligned} \tag{2.16}$$

Note that integrating the equations of motion has been reduced to four additions per time-step (aside from the particle weighting).

In order to complete the process, the electric field components will be normalized. First, substituting the expression for weighting the electric field components to the particles (the force on the particle) into the normalized acceleration components gives the following:

$$\begin{aligned}\tilde{a}_{r_{k,t}} &= \frac{q_k \left\{ \sum_{i,j} W(r_k, z_k, r_i, z_j) E_{r_{i,j,t}} \right\} (\Delta t)^2}{m_k (\Delta r)} \\ \tilde{a}_{z_{k,t}} &= \frac{q_k \left\{ \sum_{i,j} W(r_k, z_k, r_i, z_j) E_{z_{i,j,t}} \right\} (\Delta t)^2}{m_k (\Delta z)}\end{aligned}\quad (2.17)$$

Equations 2.13 and 2.17 suggest the following normalization for the electric field components:

$$\begin{aligned}\tilde{E}_{r_{i,j,t}} &= \frac{q_k (\Delta t)^2}{2 m_k (\Delta r)^2} (\phi_{i-1,j,t} - \phi_{i+1,j,t}) \\ \tilde{E}_{z_{i,j,t}} &= \frac{q_k (\Delta t)^2}{2 m_k (\Delta z)^2} (\phi_{i,j-1,t} - \phi_{i,j+1,t})\end{aligned}\quad (2.18)$$

Now that the model equations have been simplified it is useful to summarize the final equations and their use before moving on. First, equation 2.9 through 2.11 are used to form the charge density on the grid (using specific weighting schemes discussed below). Second, Poisson's equation (equation 2.8) is solved to find the potential on the grid. Equations 2.18 are then used to find the normalized electric field components on the grid. The leapfrog integration method is then used to update each particle's position and velocity components. Rewriting equations 2.16 in terms of the normalized electric field components gives:

$$\begin{aligned}\tilde{v}_{r_{k,t+\frac{1}{2}}} &= \tilde{v}_{r_{k,t-\frac{1}{2}}} + \sum_{i,j} W(\tilde{r}_{k,t}, \tilde{z}_{k,t}, i, j) \tilde{E}_{r_{i,j,t}} \\ \tilde{v}_{z_{k,t+\frac{1}{2}}} &= \tilde{v}_{z_{k,t-\frac{1}{2}}} + \sum_{i,j} W(\tilde{r}_{k,t}, \tilde{z}_{k,t}, i, j) \tilde{E}_{z_{i,j,t}} \\ \tilde{r}_{k,t+1} &= \tilde{r}_{k,t} + \tilde{v}_{r_{k,t+\frac{1}{2}}} \\ \tilde{z}_{k,t+1} &= \tilde{z}_{k,t} + \tilde{v}_{z_{k,t+\frac{1}{2}}}\end{aligned}\quad (2.19)$$

In practice, the sum over all grid points in equation 2.19 is done over only the nearest one or four grid points, depending upon the weighting method used. This sequence is

accomplished once per time-step. The above equations do not completely describe the model. The solution of Poisson's equation, boundary conditions, particle and field weighting, and charged-neutral particle collisions must be discussed.

**Solution of Poisson's Equation on the Grid.** Efficient FORTRAN subprograms for solving equation 2.8 (among other separable elliptic partial differential equations) have been developed by Swarztrauber, Sweet, and Adams and made available by the National Center for Atmospheric Research via the internetwork in the FISHPAK software package (Adams and others, 1988). The FISHPAK subprograms are used to solve equation 2.8 on the grid. FISHPAK uses a cyclic reduction algorithm to solve the block tridiagonal system of equations that result from equation 2.8. The general method is described in (Sweet, 1977) while the actual computer subprograms are documented in (Swarztrauber and Sweet, 1975).

The FISHPAK subprogram HWSCYL was used to solve equation 2.8. (Swarztrauber and Sweet, 1975:37 - 59). This subprogram requires that the right-hand side of equation 2.8 reside on the grid prior to calling the subprogram. When the subprogram completes the grid contains the solution to equation 2.8 in terms of the potential. In addition, the subprogram HWSCYL requires that boundary conditions be specified. The boundary conditions can be of the following form: solution specified, normal derivative of the solution specified, or unspecified at  $r = 0$  (due to symmetry). In this case three boundary conditions (at  $r = R$ ,  $z = 0$ , and  $z = L$ ) are required, where  $R$  is the radius of the discharge tube and  $L$  is the distance between the electrodes. The boundary at  $r = 0$  is allowed to remain unspecified since, by symmetry, the normal component of the derivative of the solution vanishes.

**Boundary Conditions .** The grid used in the calculation and the boundaries upon which conditions must be specified are shown in figure 2.5. Since the voltage on each electrode is known at all times, the solution can be specified for the boundary conditions

at  $z = 0$  and  $z = L$ . Either or both electrodes may be held at a constant voltage or driven at some frequency. The voltages on the electrodes are specified by:

$$\begin{aligned} V_0 &= V_{dc_0} + V_{rf_0} \sin[2 \pi f_{rf_0} t (\Delta t)] \\ V_L &= V_{dc_L} + V_{rf_L} \sin[2 \pi f_{rf_L} t (\Delta t)] \end{aligned} \quad (2.20)$$

where  $V_0$  and  $V_L$  are the voltages on the electrodes at  $z = 0$  and  $L$  respectively,  $V_{dc_0}$  and  $V_{dc_L}$  are dc bias voltages,  $V_{rf_0}$  and  $V_{rf_L}$  are the peak driving voltages, and  $f_{rf_0}$  and  $f_{rf_L}$  are the driving frequencies in Hz.

The boundary condition at the glass wall is more complicated. If we treat the glass wall as "an infinite sticky insulator" after Hockney we can specify the normal derivative of the solution at the remaining boundary (Hockney, 1966:1829). Any charged particle which strikes the glass wall sticks to the wall -- its charge is weighted to the grid point(s) adjacent to the cell and deleted from the simulation, leaving behind a surface charge. It can be shown (see appendix A) that the normal component of the electric field within a semi-infinite dielectric with infinite dielectric constant vanishes. This will serve as the boundary condition imposed behind the surface charge which forms on the glass wall. Hence, the normal derivative of the solution will be specified:  $E_r = -\frac{\partial \phi}{\partial r} = 0$ . Figure 2.6 depicts the grid, glass wall, surface charge, and boundary condition.

In addition to specifying the conditions on the potential at the boundaries, the particle behavior at the boundaries must also be specified. The particle behavior at  $r = R$  has already been specified above. If a particle crosses the grid line at  $r = 0$ , by symmetry, the  $r$  components of the particle's position and velocity are negated. The  $z$  components are left unchanged. At the electrodes the particle behavior is specified by reflection and emission coefficients after Surendra and Graves (Surendra and Graves, 1991:145). A charged particle which comes into contact with one of the electrodes may be absorbed or reflected by the wall depending upon the comparison of a uniform random number to the



specified reflection coefficient. Particles that are not absorbed by the wall undergo specular reflection back into the discharge. Furthermore, a charged particle which strikes the wall may cause the emission of an electron from the wall. Again, a secondary electron is created depending upon the comparison of a uniform random number to the specified emission coefficient. Emitted electrons are given an initial velocity directed perpendicular to the wall with some user specified energy. In general, ions are given a zero reflection coefficient while electrons are given a zero emission coefficient.

One last word concerning the boundaries. In the non-boundary regions of the grid the electric field components are found by simply applying equation 2.18 to all interior grid points. On the radial boundaries the electric field is specified by the boundary conditions themselves (as described above). On the electrode boundaries applying equation 2.18 presents a problem in that the grid "runs out" and equation 2.18 can not be used. A simple solution used by Vender and Boswell is to estimate the normal component of the electric field at the boundary by "linear extrapolation from the two values nearest the grid point" (Vender and Boswell, 1990:726). This method is adopted for use here. Of course, the component of the electric field parallel to the electrode at the axial boundaries is zero, since the electrode is an equipotential surface.

**Particle and Field Weighting.** Birdsall and Langdon describe several methods for charge and field weighting (Birdsall and Langdon, 1991:19 - 20, 308 - 309, 336 - 337). The charge weighting schemes will be described here with the understanding that the same method is used for weighting the fields back to the particles. The goal is to weight the charge from the continuous particle locations to the discrete grid points to form the right hand side of Poisson's equation. Any of three weighting schemes may be used: nearest-grid-point (NGP), bilinear, or volume weighting (bilinear in  $r^2$ ). Birdsall and Langdon refer to the bilinear in  $r^2$  method as area weighting. Since the weighting is actually based on a cylindrical volume, the name volume weighting seems more

appropriate and will be used here, although the algorithm is similar to that described in Birdsall and Langdon (Birdsall and Langdon, 1991:336 - 337).

NGP weighting assigns all of a particle's charge to the nearest grid point. This method is efficient, since it only requires the particle's rounded position components. However, the use of NGP results in a noisy plasma -- as a particle moves across a cell the charge assigned to a single mesh point suddenly jumps from zero to the particle's charge (Birdsall and Langdon, 1991:20).

Figure 2.7 will help to explain both the bilinear and volume weighting schemes (Birdsall and Langdon, 1991:309). In bilinear and volume weighting the particle's charge is assigned to the four nearest grid points (Birdsall and Langdon, 1991:336). Referring to figure 2.7, the proportion of the charge assigned to grid point A is (Birdsall and Langdon, 1991:336):

$$\frac{\text{Area or Volume of region a}}{\text{Area or Volume of regions (a + b + c + d)}} \quad (2.21)$$

The remaining three grid points are handled in a similar manner.

**Monte Carlo Collisions.** Charged particle-neutral collisions are accomplished via Monte Carlo methods with the aid of the null collision technique. Birdsall provides a general overview of incorporating Monte Carlo collisions into particle simulations (Birdsall, 1991:79-82). Birdsall points out that (unlike the development so far) the computer particles are treated as individual particles in the collision process. So far, the computer particles have been treated as many physical particles (Birdsall, 1991:80).

In the null collision technique, a "fake" total collision cross-section is constructed which must conform to the following rules: 1) it must be greater than the sum total of all other collision cross-sections for all energies and 2) it must be proportional to the inverse of the charged particle's speed. In this way, the "fake" total collision frequency is independent of particle energy and constant for the entire simulation so that the

calculation of a cross-section for each particle at each time-step is precluded (Birdsall, 1991:82). Now that the fake total collision cross-section has been constructed, the null collision technique can be carried out.

The first step is to calculate the percentage of particles to collide each time-step:

$$P = 1 - \exp[-n_{gas} \sigma_{fake} v (\Delta t)] \quad (2.22)$$

where  $n_{gas}$  is the neutral gas number density,  $\sigma_{fake}$  is the fake total collision cross-section, and  $v$  is the particle speed (Birdsall, 1991:82). Since the fake total cross-section is given by:

$$\sigma_{fake} = \frac{k}{v} \quad (2.23)$$

where  $k$  is a proportionality constant, equation 2.22 can be calculated independent of particle speed and at the start of the simulation. Given the percentage of the total number of particles to collide with neutrals, a random subset is constructed from the total set of charged particles. The percentage is calculated at the start of the simulation, while the random subset is determined each time-step. The subset of particles to collide is selected as follows. A "skipping constant" is calculated by taking the inverse of equation 2.22 (this is calculated at the start of the simulation) (Smith, 1991). A uniform random number  $R_1$  ( $0 \leq R_1 \leq 1$ ) is drawn and multiplied by the skipping constant at the start of each time-step. This gives a new index of the first particle in the list of charged particles to collide. Subsequent particles are chosen by looping through the list, incrementing the loop index by the skipping constant each time through the loop. This procedure produces a random subset of the total set of charged particles.

Now that the subset of particles to collide is known, the type of collision must be determined. This is done by comparing the collision cross-sections relative to the fake total cross section to a uniform random number,  $R_2$  ( $0 \leq R_2 \leq 1$ ) as in Hockney and Eastwood (Hockney and Eastwood, 1988:379). Wherever  $R_2$  falls in the sequence of

relative collision cross-sections is the collision process that is carried out. An example will help to illustrate the method. Say, for instance, one would like to model two real collisions. Including the null collisions this makes a total of three possible collision processes. First, calculate the following quantities:

$$\begin{aligned} m_1 &= \frac{\sigma_1}{\sigma_{fake}} \\ m_2 &= \frac{\sigma_1 + \sigma_2}{\sigma_{fake}} \\ m_3 &= 1 - (m_1 + m_2) \end{aligned} \tag{2.24}$$

Note that the  $m_i$  sum to one, with  $0 < m_1 < m_2 < m_3 < 1$ . Next, draw the uniform random number  $R_2$ . Where  $R_2$  falls in the sequence of quantities calculated via equations 2.24 determines the collision which occurs. For  $0 \leq R_1 < m_1$ , real scattering process one occurs. For  $m_1 \leq R_1 < m_2$ , real scattering process two occurs. If  $m_2 \leq R_1 \leq 1$ , then a null collision occurs -- nothing is done (Hockney and Eastwood, 1988:379).

Once we have calculated which particles undergo which collision processes during each time-step, the only detail in the collision process left to discuss is the collision kinetics. Before describing the collision kinetics for the collision processes included in the model, the number of velocity components carried in the simulation must be mentioned. As described above, the model equations of motion require only two velocity components -- one for each dimension simulated. However, in order to properly account for the particle's kinetic energy, the third velocity component,  $v_\theta$ , is also carried. The quantity  $v_\theta$  is only altered by collision processes. This is similar to the technique used by Burger in his simulation of a one-dimensional plasma diode (Burger, 1967:660-661). As mentioned above, the particle positions are not affected by a collision. Only the particle velocities are perturbed.

The present simulation includes electron-neutral elastic, electron-neutral ionization and ion-neutral charge exchange collisions. The incorporation of the remaining collisions

is straight forward, given the basic framework constructed for the existing collisions. For elastic collisions, the scattered electrons energy is calculated via (McDaniel, 1964:24):

$$E_{electron, scattered} = E_{electron, incident} * \left(1 - \frac{2 m_e}{m_N}\right) \quad (2.25)$$

In the case of ionization, the ionization potential for the particular gas being simulated is subtracted from the total energy of the incident electron. This energy is then randomly distributed between the scattered electron and the electron created by ionization. The created ion is given the energy of a thermal ion. For an ion-neutral charge exchange collision, the ions energy is reduced to the user defined thermal ion energy. Once the energy of the constituent particles is calculated, it is distributed to the particle's three velocity components isotropically. That is, all directions of motion are made equally probable. Although the collision kinetics have been greatly simplified, they provide a start towards a more realistic representation. Specific suggestions for improvement will be made in chapter four.

A discussion of the method for specifying the collision cross-sections completes the section on particle collisions. Birdsall describes a method for specifying electron-neutral collision cross-sections (Birdsall, 1991:81). The quantities  $\sigma_{max \ ionization}$ ,  $E_{0 \ ionization}$ ,  $E_{1 \ ionization}$ , and  $E_{2 \ ionization}$  in figure 2.8 are used to describe an approximation to the electron-neutral ionization cross-section. Similarly, the quantities  $\sigma_{max \ elastic}$  and  $E_{0 \ elastic}$  in figure 2.9 are used to describe an approximation to the electron-neutral elastic collision cross-section. In addition, the fake total collision cross-section is described by the proportionality constant in equation 2.23, chosen to meet the criteria listed above for the fake total collision cross-section. The proportionality constant should be chosen to minimize the number of null collisions by making the fake total collision cross-section as close as possible to (but always greater than) the real total collision cross-section.

Although not used here, another method used by Ramos for increasing the efficiency of the null collision technique is the use of multiple fake collision cross sections in order to minimize the number of null collisions over different energy regions (Ramos, 1990:55-58). As more collision processes are added to the simulation it may be worth the added time savings to incorporate this method.

**Initial Particle Loading.** There are many choices for the method of loading the initial positions and velocities of the simulated electrons and ions. One method suggested by Birdsall is to load the particles uniformly in position and use a normalized thermal velocity distribution (Birdsall, 1991:390-391). This method was attempted with unfavorable results. At first blush it seems that almost any reasonable (devoid of large oscillations) initial phase space portrait would suffice (Vender and Boswell, 1990:726). Unfortunately, due to current memory and simulation time constraints, the simulation must be run with a limited number of particles ( $< 1.6$  million per species on the Silicon Graphics IRIS workstation used for this research). This limitation effects the allowable initial positions. If the particles are placed within the simulation uniformly in position, a large number of the electrons (which are much faster than the relatively immobile ions) initially flee to the bounding surfaces. Given enough electrons and simulation time, this would not present a problem. Regrettably, due to the small number of particles, a large percentage of the total number of electrons are lost and it is unclear whether the simulation could ever "straighten itself out." In order to offset this problem the particles are loaded so that fewer particles are put in the sheath regions, adjacent to the electrodes and glass wall. Furthermore, a number of electrons may be initially "stuck" to the glass wall (typically a few tens of electrons per grid point) to impede initial electron loss to the glass wall.

The initial particle velocities are loaded using a normalized thermal velocity distribution as in Birdsall (Birdsall, 1991:390-391). The initial speed for each particle is given by:

$$v = v_{thermal} \sqrt{-2 \log(R_3)} \quad (2.26)$$

where  $v_{thermal}$  is a user defined thermal speed and  $R_3$  is a uniform random number. Special care must be taken to exclude any  $R_3 = 0$ . The speed calculated via equation 2.26 is then divided isotropically between the velocity components (Birdsall, 1991:390-391).

**Computer Code.** The computer program which implements the model described above was written in the C programming language. The program runs on SUN SparcStations and Silicon Graphics workstations. The software does not take advantage of any system specific features so that porting the program to other computer models should be straightforward.

The source code consists of five C source files each providing a major piece of functionality. In addition, each source file has its own header file (excluding *rf.c*) that contains an interface to the functions provided by that source file (as well as any required constants, special data types, etc.). Each of the functions contained in the source files has a short description of its purpose, input parameters and output parameters. The five packages are: *particles.c*, *grid.c*, *input\_data.c*, *collisions.c*, and *rf.c*. The source code file *rf.c* is the main program, while the four other packages provide the functionality their names suggest. In addition, a header file named *pic.h* provides general constants used by all of the packages.

**particles.c.** This package defines data types, allocates storage for, and provides functions for manipulating the particle lists, loading the initial particle positions and velocities, and moving the particles each time-step.

**input\_data.c.** This package provides a function for reading the input data as well as global variable definitions for the input data. A function for calculating some constants

based on the input data is also provided. All user input is done via file. The format of the input file is described below.

**grid.c.** This package defines data types, allocates storage for, and provides functions for operating on the simulation grid. Functions for charge weighting, solving Poisson's equation (an interface to the FISHPAK routine), and calculating the electric field is provided. Since FISHPAK was written in FORTRAN and the simulation is written in C, special care was taken in writing the function that interfaces to FISHPAK. Since FORTRAN stores two-dimensional arrays in column major format and C stores them in row-major format, the grid must be converted to and from column major format each time-step.

**collisions.c.** This package provides the functionality to perform Monte Carlo collisions. Functions are provided to calculate the collision cross sections as a function of particle energy. A function is provided for determining collision types and collision kinetics based on the cross section functions and particle energy.

**Input File Format.** A sample input file is shown in appendix C. Table 2.1 indicates the meaning of each variable name as well as the units associated with these quantities.

<u>Input Variable</u>	<u>Explanation (Units)</u>
dz	z grid cell size (m).
Nz	Number of grid cells in z. $Nz * dz$ gives distances between electrodes (none).
dr	r grid cell size (m).
Nr	Number of grid cell in r. $Nr * dr$ gives radius of discharge tube and electrodes.
dt	Time-step size (seconds).
Nt	Number of time steps to simulate (none).
npr npz	The quantities npr and npz define the maximum number of particles per cell = $npr * npz$ .



MiMe	The ratio of ion mass to electron mass (none).
Ve	Speed of a thermal electron (m/s).
Vi	Speed of a thermal electron (m/s).
P	Neutral gas pressure (Torr).
Ns	Number of real particles per super particle (none).
sigma_total	The proportionality constant in equation 2.23 used to describe the fake total collision cross section.
sigma_max_ion e0ion e1ion e2ion	The next five parameters describe the electron-neutral ionization cross section as in figure 2.8.
sigma_max_elas e0elas	The next two parameters describe the electron-neutral elastic cross section as in figure 2.9.
sigma_ch_ex	Constant ion-neutral charge exchange collision cross-section ( $m^2$ ).
SecE	Coefficient to describe secondary electron emission due <u>electron</u> bombardment. Always set to 0 (none).
SecI	Coefficient to describe secondary electron emission due <u>ion</u> bombardment (none).
VSec	Velocity of a secondary electron (m).
RefE	Electron electrode reflection coefficient (none).
RefI	Ion electrode reflection coefficient (none).
Vrf0 frf0 Vdc0 VrfL frfL VdcL	The next six parameters are the constants in equation 2.20 used to describe the voltages on the electrodes (voltages in volts and frequencies in Hz).
weighting	Weighting scheme to use. 1 = NGP. 2 = Bilinear. 3 = Volume. Other = Error. (none).
Nout	Diagnostic output line every Nout time-steps (none).
Pout	Write potential on grid to file every Pout time-steps (none).
Eout	Write electron phase space file every Eout time-steps (none).

Iout	Write ion phase space file every Eout time-steps (none).
Fout	Write electric field components on grid to file every Fout time-steps (none).
Sout	Write charge on glass wall to file every Sout time-steps (none).
Cout	Write charge on grid to file every Cout time-steps (none).
Rout	Write the right-hand-side of Poisson's equation to file every Rout time-steps (none).
Tout	Update ionization diagnostic file every Tout time-steps (none).
seed	Random number generator seed. Change seed will start a new pseudo-random number sequence (none).

**Table 2.1.** Input File Description.

**Program Compilation, Linking and Execution.** The program is compiled and linked (through a command found in the source code directory) by typing *build* at the operating system command line. This produces an executable file called *rf*. In order to execute the program the following command line is executed:

```
rf input_file [electron_phase_space_file] [ion_phase_space_file] [wall_charge_file] <return>
```

where *input\_file* is of the format specified above. The command line arguments in square brackets are optional. They specify phase space files and wall charge from previous runs. This feature may be used to "warm start" the simulation from where a previous run stopped.

**Output Files.** The program produces a number of output files. Each output file name has the following format: *input\_file.time\_step.output\_file*. The *input\_file* corresponds to the input file name specified on the command line. The *time\_step* corresponds to the time-step at which the output file was created. The *output\_file* corresponds to which output file this is. The following quantities may be written to file

during a simulation: (1) potential at each grid point, (2) electron phase space, (3) ion phase space, (4) electric field components at each grid point, (5) surface charge on the glass wall, (6) weighted charge at each grid point, and (7) the right hand side of Poisson's equation at each grid point. In addition a file is created and updated which stores the location of ionizing collisions that have occurred during the simulation. Small programs were written to analyze the data contained in the phase space file to obtain the average particle velocity components, average particle energy, and average number of particles per cell. These programs will not be described.

### III. Model Verification, Experimental Results and Discussion

#### Single Particle Test

Two simple cases involving the judicious placement of a single particle within the simulated discharge tube were run to test the simulation (Smith, 1991). In case 1, a single electron was placed on the radial axis of the discharge tube and exactly midway between the two electrodes. In the second case, a single electron was again placed on the radial axis of the tube, but displaced to one side of the midway point between the electrodes. In both cases the particle was given zero initial velocity and both electrodes were held at zero potential. Both cases have an analytic solution for the motion of the electron and are thus good tests.

**Case 1.** A single electron with zero initial velocity placed on the radial axis of the discharge tube and midway between two grounded electrodes will remain at rest. This can be shown via the method of images (Feynman and others, 1964: 6-9 to 6-10). The electron has two image charges  $+e_1^0$  and  $+e_2^0$  located as shown in figure 3.1. These image charges also have images. The image charge  $+e_1^0$  has an image  $-e_1^1$ . Similarly, the image charge  $+e_2^0$  as an image  $-e_2^1$ . These images of image charges go on forever. The motion of the electron follows from the force on the electron due to the infinite number of image charges.

The force exerted on a charged particle by a second charged particle is given by Coulomb's law:

$$\vec{F}_{12} = \frac{Q_1 Q_2}{4 \pi \epsilon_0 r^2} \hat{e}_r, \quad (3.1)$$

where  $\vec{F}_{12}$  is the force on particle 1 due to particle 2,  $Q_1$  is the charge on particle 1,  $Q_2$  is the charge on particle 2,  $\epsilon_0$  is the permittivity of free space,  $r$  is the distance between the charges, and  $\hat{e}_r$  is a unit vector pointing from  $Q_2$  to  $Q_1$ . In the case at hand, the force exerted on the electron due to the infinite number of image charges is zero, since the

force due to each pair of image charges vanishes due to the symmetrical location of the images about the electron: The force on the electron due to  $q_1^i$  exactly cancels the force on the electron due to  $q_2^i$ , where  $q$  takes on values of  $+e$  or  $-e$ . Therefore, it has been shown that a single electron with zero initial velocity placed on the radial axis of the discharge tube and midway between two grounded electrodes will remain at rest.

The simulation was run with the conditions described above for 50 time steps. As expected, the particle did not move -- it remained on axis and midway between the two electrodes for the duration of the simulation. This is a good qualitative test of the field solver and particle mover. Case 2 provides a more quantitative test and insight into some of the model's limitations.

**Case 2.** The simulation was run with the same conditions as case 1 except the electron was moved slightly off the midway point between the two electrodes. The acceleration of the electron as a function of position may be calculated analytically (again using the method of images) and compared to the approximate value calculated and used by the simulation.

Figure 3.2 shows the position of the electron along with six of the infinite number of image charges. The electron is a distance  $z$  from the left electrode and consequently a distance  $L - z$  from the right electrode. We would like to find an analytic expression for the acceleration of the electron as a function of the coordinate  $z$ . Let the image charges  $q_n^i$  be labeled in the same fashion as case 1. Let  $r_n^i$  be the distance from image charge  $q_n^i$  to the electron located at  $z$ . The force on the electron due to image charge  $q_n^i$  is given by:

$$\vec{F}_n^i = \frac{q_n^i (-e)}{4 \pi \epsilon_0 (r_n^i)^2} \hat{e}_r \quad (3.2)$$

The total force on the electron due to the infinite number of images is given by:

$$\vec{F} = \sum_{i=0}^{\infty} \sum_{n=1}^2 \vec{F}_n^i \quad (3.3)$$

The distance between each image charge and the electron,  $r_n^i$ , can be expressed in terms of the location of the electron,  $z$ , and the distance between the electrodes,  $L$ , and is shown beneath each image charge in figure 3.2. Upon substitution of the first twelve  $r_n^i$  into equation 3.3 and 3.4 and simplification:

$$\vec{F} = \frac{e^2}{16 \pi \epsilon_0} \left[ -\frac{1}{z^2} + \frac{1}{(L-z)^2} - \frac{1}{(L+z)^2} + \frac{1}{(2L-z)^2} - \frac{1}{(2L+z)^2} + \frac{1}{(3L-z)^2} - \dots \right] \hat{e}_z \quad (3.4)$$

Since  $\hat{e}_z$  lies along the  $z$ -axis for every image charge, the acceleration of the electron due to all the image charges is entirely along the  $z$ -axis. Upon simplification of equation 3.4 and the use of Newton's second law, the  $z$ -component of the acceleration can be written as:

$$a_z = \frac{e^2}{16 \pi \epsilon_0 m_e} \sum_{i=0}^{\infty} \left\{ \left[ (i+1)L - z \right]^{-2} - \left[ iL + z \right]^{-2} \right\} \quad (3.5)$$

Equation 3.5 provides an exact analytic solution for the acceleration of the electron which may be used to test the accuracy of the approximate acceleration calculated by the simulation.

The acceleration used by the simulation to advance the particle from time-step to time-step may be found from the model output and equations of motion. The  $z$ -component of the electron's velocity is updated each time step via:

$$v_{z,t+1/2} = v_{z,t-1/2} + a_{z,t} \Delta t \quad (3.6)$$

where  $v_{z,t+1/2}$  is the  $z$ -component of the particle's velocity at time-step  $t + 1/2$ ,  $v_{z,t-1/2}$  is the  $z$ -component of the particle's velocity at time-step  $t - 1/2$ ,  $a_{z,t}$  is the  $z$ -component of the particle's acceleration at time-step  $t$ , and  $\Delta t$  is the size of the time-step. Equation 3.6 can be rearranged to find the  $z$ -component of the particle's acceleration at time-step  $t$ :

$$a_{z,t} = \frac{(v_{z,t+\Delta t} - v_{z,t-\Delta t})}{\Delta t} \quad (3.7)$$

To compare the analytic solution with that of the model, the simulation was run for 35 time-steps. The particle's position and velocity components were appended to an output file after each time-step. The analytic solution was calculated at each time-step using the model calculated position of the electron and thirty terms in the infinite summation of equation 3.5. *Note that the analytic solution to the acceleration is not used to separately update the particle's position.* In this way, the only errors considered are single time-step errors in the acceleration -- cumulative effects in the trajectory of the electron due to errors in the calculation of the acceleration at each time-step are not calculated. Also note that each "electron" in the simulation is actually modeled as  $10^7$  real electrons. That is, each model electron is scaled to have a charge of  $10^7 e$  and a mass of  $10^7 m_e$  (where  $e$  is the charge of an electron and  $m_e$  is the mass of an electron). The acceleration used by the model was calculated at each time-step using the model calculated velocity and equation 3.7.

Figure 3.3 shows the percentage difference between the analytically calculated acceleration and the model calculated acceleration. It is interesting to note that the percent difference reaches local maxima and minima as the electron travels towards the electrode (in this case the initial displacement was towards the left electrode so that the electron has an acceleration in the negative  $z$  direction). Figure 3.4, a plot of the electron's normalized  $z$ -component of position versus time-step, provides a clue not only to the overall source of error, but also to the source of the maxima and minima in the percent difference between the two solutions. Note that spatial grid points exist at integer values of normalized position.

From figure 3.3, the first minima in the percent difference occurs at time-step ten. One can see from figure 3.4 that this corresponds to the electron being closest to a grid point. The same is true of time-step twenty, and so on. As the electron approaches a grid

point the charge that is weighted from the electron to the grid and the acceleration that is weighted from the grid to the electron is most accurate. Although the percent difference improves near a grid point, why is the error still quite large? The answer is in the bilinear weighting scheme used in this case. Although bilinear weighting (as discussed in chapter two) reduces the noise associated with particle and force weighting, it is ill-suited for the problem at hand. When the charge due to the electron is weighted to the two nearest grid points the problem is changed from a single particle to two particles (whose individual mass and charge sum to that of the original electron) located one grid space apart. Although this "smearing" effect is permissible (and desirable) when dealing with the collective behavior of a plasma, it introduces errors (as seen in figure 3.3) into the calculation when dealing with a single particle.

One way to get around this two-for-one particle problem is by using the NGP weighting scheme. Since the particle is maintained as a single particle whose charge is weighted wholly to the nearest grid point, one would expect the difference between the analytic solution and the model solution to decrease as the electron approaches a grid point. The results for NGP weighting with otherwise the same conditions as above are shown in figures 3.5 and 3.6. Note that when the particle is close to a grid point the percent difference between the analytic and model solution improves over bilinear weighting. *However*, when the particle gets far from a grid point the error grows to greater than thirty percent -- much worse than bilinear. This is the result of the whole of a particle's charge being weighted to a grid cell which can be up to half a grid cell from the actual position of the particle.

The results of both single particle tests give confidence in the proper functioning of the model. Furthermore, case 2 provides some insight into a limitation of the model. In particular, the simulation's strength is not in modeling single particle effects.



## Experimental Results and Discussion

**Noise Problem.** A problem with the two-dimensional model prevents running the model to convergence and obtaining quantitatively meaningful data. This problem is associated with noise in the potential in the grid cells on radial axis. This section explains the cause of this noise. Also, a method is developed which allows quantitatively meaningful analysis of some of the model results.

Before attributing the cause of the noise, a description of the problem is presented. The circumstances surrounding the noise on the grid are as follows. During the first ten RF periods some noise in the potential is seen on the radial axis of the grid. This noise does not extend very far towards the radial wall (perhaps a few grid cells). This initially small amount of noise in the potential corresponds to a much larger than normal electric field in the bulk. This gives rise to an anomalous heating of the electrons in the bulk. During the course of the simulation, this heating artificially increases the ionization rate in the bulk on radial axis. This rise in plasma density tends to increase the noise, which in turn further increases the plasma density. By the beginning of the eleventh RF cycle the noise in the potential is quite large and the plasma density on axis is growing by leaps and bounds. Figure 3.7.a shows a plot of the potential as a function of position within the discharge tube at the beginning of the eleventh RF cycle. Figure 3.7.b shows a one-dimensional slice of the same potential on the radial axis. By this time the on-axis potential is quite noisy.

As explained above, the model uses a uniform radial grid to compute the field quantities. This is believed to be the cause of the noise and can be explained as follows. The volume elements used to calculate the charge density at grid points on the radial axis are eight times smaller than the adjacent volume elements just one radial grid cell away (see equation 2.10 and 2.11). Since the number of simulation particles in the two grid

cells are approximately equal, this disparity in the size of the volume elements leads to a disparity in the charge densities associated with the two grid points -- the charge density of an on-axis grid point is eight times larger than that found one radial grid cell away. This large increase in charge density is believed to give rise to the noise in the potential. This claim is supported by figure 3.8 which shows four plots of potential as a function of position which were generated by loading sixteen cells with equal numbers of electrons and ions. The particles were loaded randomly in position within each grid cell (therefore, each grid cell is overall neutral). The electrodes are held at zero potential. In each plot the same number of real particles in a grid cell is maintained by varying the number of simulation particles and the number of real particles per simulation particle. For instance, if the number of simulation particles is increased by a factor of ten the number of real particles per simulation particle is decreased by a factor of ten. Figures 3.8.a - 3.8.c shows the effect of increasing the number of computer particles on the noise on the grid for sixteen on-axis grid cells. As expected, as the number of computer particles is increased the noise in the potential is reduced. Figure 3.8.d should now be compared to figure 3.8.c. For equal numbers of computer particles the on-axis noise in the potential is a factor of ten greater than the off-axis noise. This data supports the above explanation for the source of the noise.

Given the above, running the present two-dimensional model to convergence is impossible. Furthermore, the results for times prior to the large increase in number density and potential (in addition to not being converged) are quantitatively unusable due to the anomalous heating. Nevertheless, after the simulation has run for ten RF cycles many of the qualitative features of the discharge are evident and can be commented on. In order to do some quantitative analysis (short of incorporating a non-uniform radial grid or going to a cartesian geometry) the model was converted to a one-dimensional axial model. This was accomplished in short order by using only one component of position

(axial distance between the two electrodes) and two velocity components (an axial component and a component perpendicular to the axial component). The solution of Poisson's equation is simplified in one dimension. Most other components of the simulation were used without (or with only minor) modification. In this respect, dropping back to one-dimension for quantitative analysis provides a good method for validating most of the code given the present problems of running in two dimensions. Also, the one-dimensional model represents a discharge where the radial boundary is assumed to be located at  $r = \infty$ , thus providing a limiting solution for comparison to the two-dimensional model with a finite radial boundary. After all, one of the primary motivations in moving to a two-dimensional model is to determine the effect of the radial boundary on a discharge's plasma processing characteristics (via ion motion in the sheaths). As the discharge tube radius is reduced, one would expect its effect on the sheath ions to increase. Once the noise in the two-dimensional model is corrected, the effects of varying the radius of the discharge can be determined.

The remainder of this chapter is organized as follows. First, the experimental conditions for the simulation runs are described. Second, one-dimensional results are presented with comparison to previous models and theory. Third, two-dimensional results will be shown caveated by the above discussion. Quantitative analysis is performed on the one-dimensional data since it does not suffer from the noise problem. The qualitative features of the two-dimensional data are highlighted with comparisons to the one-dimensional runs. Furthermore, comment is made on ion motion in the sheaths as it pertains to plasma processing applications (ion anisotropy and uniformity). Although no conclusions can be drawn from this specific two-dimensional data, it illustrates the relevant issues and motivates further development of the model.

**Experimental Conditions.** The discharge discussed in this section (unless otherwise stated) consists of a helium-like gas within a discharge tube with 4 cm electrode

separation. For two-dimensional runs the discharge tube radius is 2 cm. The ion mass is  $7344 m_e$  and the collision cross-sections closely approximate those of helium. The electron-neutral collision cross-sections are based on experimental data compiled by Kieffer (Kieffer, 1973:1-7). A constant (independent of energy) ion-neutral charge exchange collision cross-section of  $1.5 \times 10^{-19} \text{ m}^2$  is used (Surendra and Graves, 1991:145). The left electrode ( $z = 0$ ) is driven sinusoidally at 10Mhz between  $\pm 500 \text{ V}$  with no DC bias (see equation 2.20). The right electrode ( $z = 4 \text{ cm}$ ) is held at zero potential. The neutral gas pressure is 250 mtorr. The electrons and ions are loaded as discussed in chapter two (ions with a thermal speed of  $1.094 \times 10^3 \text{ m/sec}$ , electrons with a thermal speed of  $1.186 \times 10^6 \text{ m/sec}$ ). For ions the electrodes are perfectly absorbing -- when an ion strikes an electrode it is always absorbed. On the other hand, electrons are reflected in 25% of their collisions with the electrodes. Charged particle bombardment of the electrodes causes no secondary particle emission.

The non-physical parameters (grid and time-step sizes) were chosen to satisfy the following relations (Hockney and Eastwood, 1988:32):

$$\begin{aligned} \omega_p (\Delta t) &<< 2 \\ \Delta &\leq \lambda_D \end{aligned} \tag{3.8}$$

where  $\omega_p$  is the electron plasma frequency,  $\Delta t$  is the time-step size,  $\Delta$  is the grid spacing, and  $\lambda_D$  is the Debye length. The discharges considered here have a plasma density of a few  $10^{15} \text{ m}^{-3}$  and bulk electron temperatures of a few eV. This gives a Debye length of a few  $10^{-4} \text{ m}$  and an electron plasma frequency of a few  $10^9 \text{ rad/sec}$ . For the one-dimensional runs a grid spacing of  $10^{-4} \text{ m}$  and time-step 0.1 nsec were chosen to satisfy relations 3.8 (due to memory and run-time constraints a grid spacing four times larger than this was used in the two-dimensional runs). At ten MHz driving frequency the choice of time-step size conveniently gives 1000 time-steps per RF cycle. In order to maintain the discharge geometry 400 grid cells are used. In the one-

dimensional runs anywhere from 10,000 - 40,000 simulation particles per species were used. Although the data was less noisy when more simulation particles were used the physical quantities (potential, plasma density, etc.) were comparable (for the same conditions) over all ranges of number of simulation particles used.

The one-dimensional simulations were run for 250 - 500 RF cycles. Tracking the total number of simulation particles over time gave an initial indication of convergence -- when the total number of particles remained constant over a couple of hundred RF cycles (within one or two percent of the total number of particles) the simulation was assumed converged. In the case of the one-dimensional model the limiting factor in attaining convergence is the time it takes for the ions in the center of the discharge to reach the electrodes (Vender and Boswell, 1990:725). Simulations started with a plasma density which is too low or too high demand longer run times dictated by the rate of loss or production. One can use the time it takes for an ion in the center of the discharge to reach an electrode as an estimate of a time characteristic of convergence. For the conditions stated above this corresponds to approximately 5.0  $\mu\text{sec}$  (50 RF cycles). Thus, a characteristic time for reaching convergence is some number of ion transit times ( $\approx 50$  RF cycles) dictated primarily by how close the initial bulk plasma density is to the converged solution.

**One-Dimensional Results.** Two one-dimensional simulation cases are presented. First, the results of a one-dimensional run with the parameters described above are discussed. Second, the results are presented from a one-dimensional run with the same parameters as the first, except that *no ion-neutral collisions* are included. A comparison of the two runs provides a good example of the importance of ion collisions on the sheath properties of the RF glow discharge.

Figures 3.9 and 3.10 show the potential and electric field (respectively) as a function of position within the discharge at various times in the RF cycle. Note the action of the

sheaths in response to the electrode's changing potential. The sheath at the left electrode vanishes at  $\omega t / 2\pi = 0.25$  while the sheath at the right electrode vanishes at  $\omega t / 2\pi = 0.75$ , where  $\omega$  is the RF frequency in rad/sec, and  $t$  is time in sec.

Figure 3.11 shows the charged particle densities as a function of position within the discharge at three times in the RF cycle. As previously discussed, the electrons are excluded from the region adjacent to an electrode at those times in the cycle when a sheath is formed between the electrode and the plasma. As the sheath contracts the electrons enter the previously forbidden region. When the sheath has completely vanished some electrons reach the electrode as indicated in the non-zero electron number density at the left electrode in figure 3.11.c. The average electron energy as a function of position within the discharge for various times in the RF cycle is shown in figures 3.12. Much can be determined from figure 3.12 about the response of the electrons to the time-varying field in the discharge. Figure 3.12.a shows the average electron energy at the beginning of the RF cycle. Note that the energy is not symmetric -- the average electron energy near the right plasma-sheath boundary is greater than the energy near the left plasma-sheath boundary. This can be explained by following the electron energy through a half-cycle. Figures 3.12.b through 3.12.e show the average electron energy at  $\omega t / 2\pi = 0.125, 0.25, 0.375$ , and  $0.5$ . It can be seen that at  $\omega t / 2\pi = 0.5$  the same lack of symmetry is apparent, except that the higher energy electrons are near the left electrode. Let's follow the electrons into in the sheath, starting with figure 3.12.a. At this time the electrons which have made it into the region near the left electrode have (on average) higher energies than the bulk electrons. At first thought this seems unreasonable. After all, (referring to figure 3.10.a) there is no field in the sheath region at this time that will support accelerating the electrons to such a high energy. It turns out that only those high energy electrons (previously in the bulk) make it into the left most portion of the discharge at this time in the cycle. At  $\omega t / 2\pi = 0.25$  the slower electrons have had a

chance to enter the region and the average energy decreases slightly. At this point the sheath is about to reform. As the sheath advances (figures 3.12.d and e) the electrons in the sheath are swept out of the sheath region, gaining energy from the sheath. This explains the lack of symmetry at the beginning and middle of the RF cycles. Between the middle and the beginning of the cycle the entire process is repeated, except at the right electrode. Consequently, those electrons at the right plasma-sheath boundary are left with higher average energies (figure 3.12.a). This finding (and explanation) as well as an observed average bulk electron energy of approximately 5 eV and plasma density in the center of the discharge of  $3.4 \times 10^{15} \text{ m}^{-3}$  is consistent with the work of others under similar conditions (Surendra and Graves, 1991:146, 150).

Figure 3.11 also shows that the ion density is not modulated by instantaneous changes in the electric field. Even as the sheath vanishes and reforms the ion density remains fairly constant. This is due to the large mass of the ions as compared with that of the electrons -- at this high driving frequency the ion density responds to a period average field which continually draws ions to the electrodes.

Figure 3.13 shows the average ion energy as a function of position within the discharge at the beginning (figure 3.13.a) and midway through (figure 3.13.b) an RF cycle. Note that the average ion energy is not symmetric during the cycle. Figure 3.13.a corresponds to a time *just after* the sheath at the left electrode has fully formed and the sheath at the right electrode has vanished. In this manner, the ion energy responds to a half-cycle average -- during the half-cycle when a sheath is formed the ions in that sheath region gain more energy than the ions at the opposite end of the discharge.

Note that the average ion energy at the left electrode in figure 3.13.a is approximately 30 eV. This is much less than the time average potential available to the ions during the preceding half-cycle. This is due to ion-neutral collisions which preclude most of the ions from reaching the wall with all of the energy available from the sheath. The fast ions

in the sheath collide with slow neutrals and in the process give up energy to the neutrals. This can be seen in figure 3.14 which is a  $z-v_z$  phase space plot of ions in the sheath adjacent to the left electrode at the beginning of an RF cycle. The ions in the sheath with the most energy at their respective positions form a line of ions which have not yet undergone a collision. If one extends a straight line through this line of ions towards the electrode, the line intersects the electrode at about  $9 \times 10^4$  to  $10^5$  m/sec. This corresponds to roughly 175 to 210 V. Thus, the ions in the left sheath (at least at the beginning of the cycle) must have responded to an average potential of around 200 V (this is supported below by the simulation run without ion-neutral collisions).

The average number of collisions an ion will undergo while traversing the sheath,  $\bar{C}$ , may be calculated given the collision cross-section,  $\sigma_i$ , neutral density,  $N_n$ , and the sheath length,  $d$ :

$$\bar{C} = d N_n \sigma_i \quad (3.9)$$

Since the ion collision cross-section used in this simulation is independent of energy (a constant value of  $1.5 \times 10^{-19} \text{ m}^2$ ),  $\bar{C}$  may be calculated for all ions. Given the numerically found sheath length of 0.65 cm (at the start of the RF cycle) and a neutral density of  $8 \times 10^{21} \text{ m}^{-3}$  (0.25 torr) this gives (on average) 7.8 collisions for each ion during its travel across the sheath. Thus, the average ion energy at the wall being only 15% of the maximum wall energy is reasonable given this degree of ion collisionality in the sheath.

Next, the results from a simulation with the same conditions as above, but with no ion-neutral collisions, are presented. Figure 3.15 shows the average ion energy at the start of an RF cycle as a function of position within the discharge. As in the previous case, the energy is not symmetric about center of the discharge. Unlike the previous case, the average energy at the left electrode is 222 eV -- the ions don't experience any energy



reducing collisions as they travel in the sheath towards the electrode. The 222 eV ion energy at the left electrode roughly corresponds to the maximum value of ion wall energy for the case with ion collisions. The  $z-v_z$  phase space plot in figure 3.16 corresponds to the beginning of an RF cycle and shows the ions being accelerated through the sheath, experiencing no energy reducing collisions. The ions which have not attained the maximum energy are presumed to have been born in the sheath as a result of electron-neutral ionization.

Since the ions do not undergo collisions in the sheath they are more readily lost to the electrodes. This results in a lower plasma density as indicated in figure 3.17. This decrease in plasma density has implications on the sheath structure. Figure 3.18 shows the electric field at the beginning of an RF cycle. Note that the sheath length at the beginning of the RF cycle has increased to well over 1 cm as compared to the value of 0.65 cm found in the case with ion collisions. The increased sheath length with the absence of ion collisions can be explained as follows. Increased ion collisionality in the sheath reduces the ion energy as seen in figures 3.13 and 3.15. In order to maintain the same ion flux, the ion density must increase for increasing ion collisionality (as seen in figure 3.11 and 3.17). This increase in ion density for increasing ion collisionality results in a larger electric field gradient,  $\frac{\partial^2 \phi}{\partial x^2}$ , via Poisson's equation. For the same applied voltage this requires a smaller sheath length. Therefore, all other things equal, one expects the sheath length to decrease and the ion density to increase for increasing ion collisionality (Sheridan and Goree, 1991:2801).

Before moving on to the two dimensional results, the results from a parameter study on the effect of varying the applied voltage is presented. The experimental conditions are the same as above with ion collisions included. The applied voltage is varied from 100 to 1000 V. The plasma density at the center of the discharge and the sheath length are measured as a function of applied RF voltage. As noted above, the primary factor in

convergence time is the time it takes to achieve the correct bulk plasma density for the given discharge conditions. The results presented here can be used, among other things, as an aid in choosing the initial conditions. Figure 3.19 shows the plasma density in the center of the discharge as a function of applied RF voltage along with a best fit line. Over the range of applied voltages the plasma density is approximately proportional to the applied voltage. This finding does not agree with the results of Vender and Boswell (see equation 2.0) for their simulation of atomic hydrogen. The major differences in the two simulations are that the ionization potential of hydrogen is approximately 10 eV less than that of helium, and they did not include elastic collisions in their model. The sheath length at the beginning of an RF cycle as a function of applied voltage is shown in figure 3.20. The sheath length is fairly constant over the range of applied voltages for all but the lowest voltages in agreement with Vender and Boswell.

**Two Dimensional Results.** The two-dimensional model was run with the same conditions as above with ion-neutral charge exchange collisions. Also, the discharge radius is set to 2 cm. Although no conclusions can be drawn from this data due to the problems sighted above, a comparison of the results with the above one-dimensional data, as well as investigating the ion motion in the sheaths, is worthwhile.

Figure 3.21.a through 3.21.c show the potential as a function of position in the discharge at  $\omega t / 2\pi = 0.25, 0.5$ , and  $0.75$ . In these plots, the left electrode is driven and is at  $z=0$  and the right electrode is at  $z=4$  cm, as before. The discharge tube wall is at  $r=2$  cm. A qualitative comparison to the previously presented one-dimensional data (see figures 3.9) shows a similar axial profile of the potential. The on-axis noise is especially evident at  $\omega t / 2\pi = 0.5$ . The radial profile of the potential is discussed below.

As previously discussed, of importance to RF plasma-assisted processing is the motion of the ions in the sheaths. As such, the remainder of this section is devoted to examining the ion motion in the sheaths in light of the axial and radial fields. Figure 3.22

shows the average ion radial velocity as a function of position within the discharge at the beginning of an RF cycle. In the plasma bulk the ions have small radial velocity components (as well as small total energies). As the ions enter the sheath they gain radial velocity. Upon continuing in the sheath the average radial velocity decreases. This is presumed to be due to the increase in collision frequency with increasing velocity -- as the ions gain energy from the sheath they are more likely to undergo a collision thereby reducing their total energy. Since the amount of the radial potential difference in the sheath is hard to determine from figures 3.21, a one-dimensional plot at constant  $z = 3.5$  cm at  $\omega t / 2\pi = 0.25$  is shown in figure 3.23. This corresponds to an axial position just inside the sheath at this time in the RF cycle. One can see a large potential drop in going from  $r = 0$  to the discharge wall. This explains the increase in radial velocity at the plasma-sheath boundary. Most of this large potential drop is due to the fact that the simulation has only run for ten RF cycles -- the electrons and ions are still diffusing to the glass wall at independent rates. Unlike the electrons, the slower ions have not had a chance to reach the glass wall. Therefore, the wall is more negatively charged than it would be at some later time after the ions have had a chance to set up a space charge electric field that promotes diffusion of both species at the ambipolar rate.

The average ion energy as a function of axial position within the discharge at constant  $r = 2.4$  mm at the beginning of an RF cycle is shown in figure 3.24. Note the average ion energy at the left electrode of just over 30 eV and the asymmetry similar to the one-dimensional case with ion collisions. Figure 3.25 shows the average ion energy across the left electrode. Two-dimensional data like this is required to determine the degree of uniformity of ion energy deposition across the wafer platen.

Figure 3.26 shows the average ratio of the radial and axial velocity components for ions at the left electrode ( $z = 0$ ) at the beginning of an RF cycle. This plot provides data on the directionality of ions at the electrode. Note that for values of radius near  $r = 0$  the

ions have velocities directed primarily perpendicular to the electrode. As the glass wall is approached through increasing values of  $r$ , the average radial velocity component increases to approximately 18% of the average axial component. This type of data has important implications on the plasma processing characteristics of a discharge.

Further evidence of the anomalous heating due to the noise in the potential is observed through the average electron energy in the center of the discharge in the two-dimensional run. The observed average bulk electron energy of approximately 12 eV is over twice as large as the value of 5 eV reported in the above one-dimensional data and by other researchers under similar conditions.

### **Summary of Results**

A simple test case involving a single particle was compared to the theoretical solution with good results. Furthermore, interesting observations regarding the limitations of particle models were made. The single particle tests give confidence that major portions of the model (potential solver, field solver, particle and field weighting, and portions of the particle mover) perform correctly.

A pair of one-dimensional discharge runs were presented that provide insight into the effect of ion collisionality on the characteristics of the discharge's sheath structure. A proportional scaling of plasma density with applied RF voltage was found for voltages over the range of 100-1000 V at 10 MHz driving frequency. Problematic two-dimensional simulation data was presented. Although no conclusions can be drawn from this data it provided an interesting comparison to the one-dimensional data as well as an example of the types of data a two-dimensional simulation of RF glow discharges makes available.

#### **IV. Suggestions and Recommendations**

This chapter is a list of required and suggested improvements to the model. Each subsection heading is phrased as a suggestion and roughly ordered by importance. A basic method for carrying out the suggestion is given in the text. Also, an assessment of the level of difficulty of implementing the recommendation is provided.

In terms of general suggestions (not specific to the model developed for this research), a fluid model should be obtained.

##### **Incorporate a Non-Uniform Radial Grid**

It has been suggested above that a non-uniform radial grid will reduce the noise in the potential on the radial axis of the grid. By forming the radial grid so that every volume element is equal, the large increase in volume at the first radial grid cell will be precluded.

Since the current subprogram in FISHPAK will only handle a uniform radial grid, another Poisson solver is required. It has been found that a Poisson solver that uses a non-uniform radial grid can be constructed by using some of the lower level FISHPAK subprograms and a coordinate transformation. The incorporation of a non-uniform radial grid also requires that some of the other algorithms be revisited. For instance, the charge and field weighting algorithms will require modifications. Also, finite differencing the potential to find the radial electric field components becomes a bit more complicated since each grid cell does not have the same radial length.

Before incorporating the non-uniform grid, some thought should be given to maintaining the relation governing the choice of grid spacing in equation 3.2. If this relation is held for the first grid cell, depending upon the radius of the simulated discharge tube, the size of the cells near the glass wall become increasingly small and the total number of cells increases. Furthermore, the accuracy of the finite differenced radial

electric field components suffers near the radial axis. Also, the accuracy of weighting the charge to the grid and the field components to the charged particles suffers.

As a quick first step one could simulate a 2D cartesian system. Of course, curvature effects are lost in this approach.

### **Incorporate Realistic System Boundaries**

The current model incorporates a cylindrical glass wall which is "butted up against" the circular electrodes. This geometry was chosen primarily based on the simplicity of the resulting boundary conditions. A more realistic discharge geometry should be adopted along with the option for a grounded conducting wall instead of the currently implemented glass wall. The added complexity in incorporating the more realistic geometries is in solving Poisson's equations with electrodes that are not on the boundaries.

### **Incorporate Accurate Modeling of Collision Kinetics**

The current modeling of collision kinetics is over simplified. Birdsall outlines a method for doing the energy balance and finding the new velocity components based on an approximation to the differential scattering cross section (Birdsall, 1991:81). This method has been used by Surendra and Graves and is suitable for noble gases (Surendra and Graves, 1991:145) Given that the basic structure for collision processes exists, inclusion of the more detailed calculation is straightforward and should be incorporated.

### **Optimize the Code**

Work should be done to optimize the code for run-time. As the model was coded, run-time was a secondary consideration. Emphasis was put on ensuring the code was correct and readable. So that longer computer runs can be made, the code should execute as fast as possible. First, a code profiler should be used to determine the portions of the

code where a majority of computation time is spent. These portions of the code should then be considered for run-time optimization.

It was noted above that the C to FORTRAN interface requires that the two-dimensional array used to store the grid quantities be converted from row major format to column major format and back to row major format each time-step. This is an immediate candidate for optimization. Unfortunately, the remedy for this situation requires that either the model be recoded in FORTRAN or the Poisson solver be recoded using C. Before either of these alternatives are done, the relative amount of time spent converting between storage formats should be determined. It may turn out that it is a small fraction of the total time in the time-step loop and optimizing other portions of the code may have more pay-off.

### **Port the Model to a Faster Computer with Large Main Memory**

Since the software does not take advantage of any system specific features, porting the code to other computer systems will be straightforward. Depending upon the computing resource available, this may allow simulation runs involving more particles and a more accurate grid spacing. Furthermore, once the above mentioned problems are corrected, quantitative comparisons to previous work and theory can be made for fully converged 2D runs.

### **Include the Effects of an Externally Applied Magnetic Field**

External magnetic fields are used in some devices to confine the plasma. These effects can be included by modifying the particle mover to include the magnetic field term in the Newton-Lorentz equation of motion.

### **Add External Circuit Elements**

Currently, the simulation does not include a model of an external circuit. The complexity of adding an external circuit simulation to the particle model has not been

investigated and its impact on computer run-time is not yet known. Given this uncertainty, more research into this area is required before an external circuit is added to the existing model. As a first step, Lawson provides a general outline of adding an external RLC circuit to a particle simulation (Lawson, 1989:267-272).



## Appendix A: Electric Field Within a Semi-Infinite Dielectric

In this appendix it will be shown that the normal component of the electric field within a semi-infinite dielectric (due to a point charge opposite the dielectric) becomes vanishingly small for large dielectric constant. Using the method of images and following the development of Becker and Sommerfeld, consider the configuration shown in figure A.1 (Becker, 1964:99-100; Sommerfeld, 1964:63-64). Shown is a particle of charge  $e$  in air (region 1 of dielectric constant  $\epsilon_1$ ) opposite a semi-infinite dielectric (region 2 of dielectric constant  $\epsilon_2$ ) along with images of charge  $-e'$  and  $e''$ . The potential within the dielectric is obtained by considering only image charge  $e''$  at point A and as if the dielectric occupied all space (Becker, 1964:99):

$$\phi_2 = \frac{e''}{4 \pi \epsilon_2 r} \quad (\text{A.1})$$

The potential in region 1 is due to the real charge at A and the image charge at B (Becker, 1964:99):

$$\phi_1 = \frac{e}{4 \pi \epsilon_1 r} - \frac{e'}{4 \pi \epsilon_1 r'} \quad (\text{A.2})$$

By applying the appropriate boundary conditions expressions for the image charges may be obtained. First, the boundary condition on the normal component of the electric displacement vector,  $\vec{D}$ . Let  $x = 0$  be at the interface and  $\hat{x} // -\hat{n}$  so that the boundary condition on  $\vec{D}$  at  $x = 0$  becomes (Sommerfeld, 1964:63):

$$\epsilon_1 \frac{\partial \phi_1}{\partial x} = \epsilon_2 \frac{\partial \phi_2}{\partial x} \quad (\text{A.3})$$

Carry out the following derivatives (Sommerfeld, 1964:63):

$$\frac{\partial}{\partial x} \left( \frac{1}{r} \right) = -\frac{x-a}{r^3} \quad \& \quad \frac{\partial}{\partial x} \left( \frac{1}{r'} \right) = -\frac{x+a}{r'^3} \quad (\text{A.4})$$

so that equation A.3 can be rewritten as:

$$-\frac{(x-a)e}{r^3} + \frac{(x+a)e'}{r'^3} = -\frac{(x-a)e''}{r^3} \quad (\text{A.5})$$

If equation A.5 is evaluated at  $x = 0$  one obtains the following expression (Becker, 1964:100):

$$e + e' = e'' \quad (\text{A.6})$$

Next, apply the boundary condition on the potential, namely

$$\phi_1 = \phi_2 \text{ at } x = 0 \quad (\text{A.7})$$

which gives the following expression (Becker, 1964:100):

$$e - e' = \frac{\epsilon_1}{\epsilon_2} e'' \quad (\text{A.8})$$

Equations A.6 and A.8 can then be used to find the image charge at point A in terms of the real charge at point A and the dielectric constants (Becker, 1964:100):

$$e'' = e \frac{2 \epsilon_2}{\epsilon_1 + \epsilon_2} \quad (\text{A.9})$$

Equation A.9 can now be used to find the normal component of the electric field within the dielectric. For  $x < 0$ :

$$E_{2z} = e \frac{(a-x)}{(\epsilon_1 + \epsilon_2) r^3} \quad (\text{A.10})$$

In the limit of region 2 having infinite dielectric constant the normal component of the electric field within region 2 vanishes.

## Appendix B: Sample Input Data File

dz	2e-4
Nz	200
dr	2e-4
Nr	75
dt	1e-10
Nt	10000
npr	6
npz	6
MiMe	7344.0
Ve	1.0e6
Vi	2.5e3
P	300e-3
Ns	8.0e4
sigma_total	7.5e-14
sigma_max_ion	3.5e-21
e0ion	24.6
elion	70.0
e2ion	110.0
sigma_max_elas	5.5e-20
e0elas	4.0
sigma_ch_ex	1.5e-19
SecE	0.0
SecI	0.3
VSec	5.93e5
RefE	0.25
RefI	0.0
Vrf0	500.0
frf0	1e7
Vdc0	0.0
VrfL	0.0
frfL	0.0
VdcL	0.0
weighting	2
Nout	50
Pout	10000
Eout	10000
Iout	10000
Fout	10000
Sout	10000
Cout	0
Rout	0
Tout	0
seed	12556789

## Appendix C: Diagrams

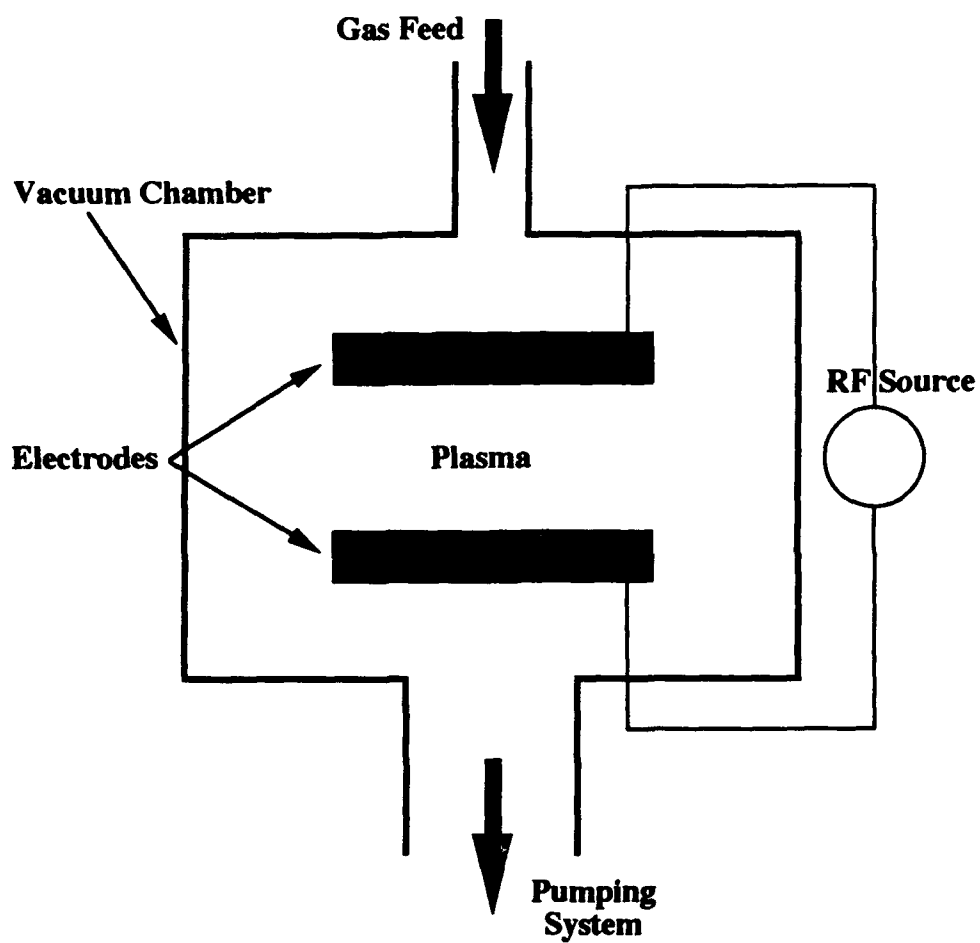


**Figure 1.1.** Schematic of a typical RF glow discharge (Flamm and Herb, 1989:15).

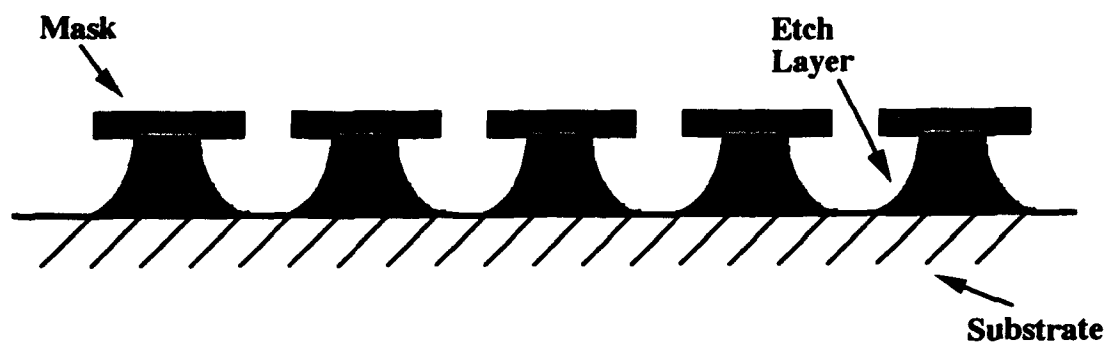


**Figure 1.2.a.** Characteristics of the isotropic, wet etched pattern (National Research Council, 1991:36).

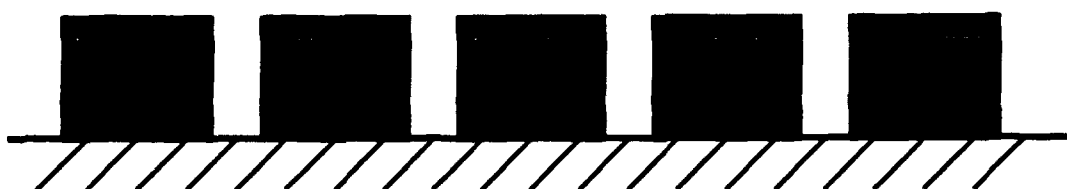


**Figure 1.2.b.** Characteristics of the anisotropic, dry etched pattern (National Research Council, 1991:36).

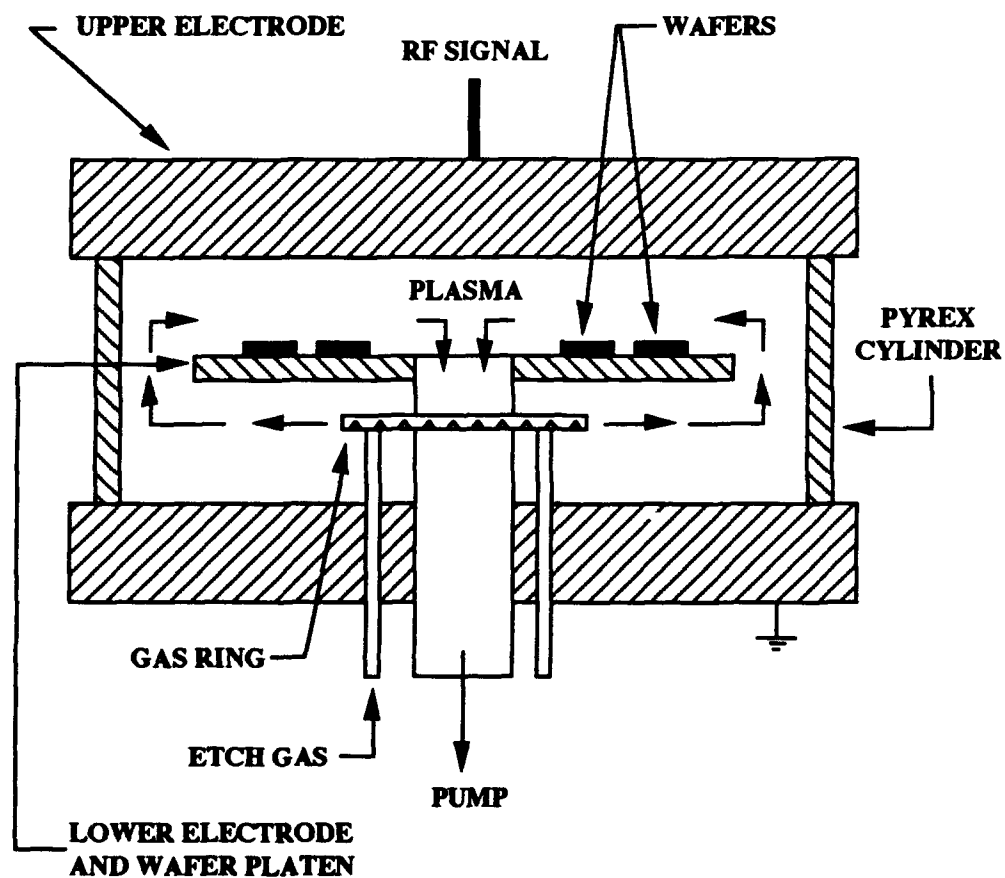
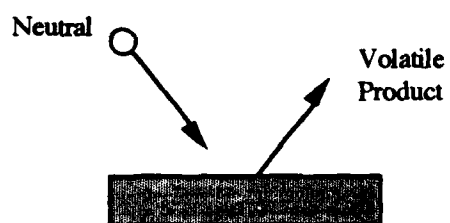
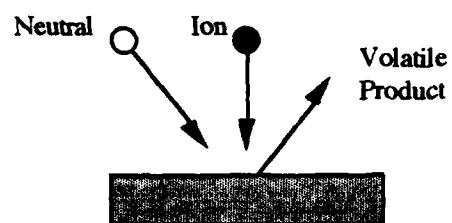


**Figure 1.3.** Schematic of the "Reinberg reactor." Note the radial gas flow feature. This design was patented by Reinberg in 1975 (Flamm and Herb, 1989:66).

### Neutral Free Radical Etching



### Ion-Assisted Etching



### Sputter Etching

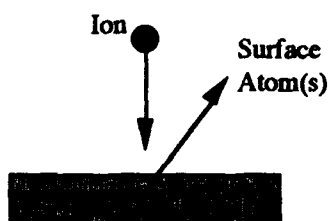


**Figure 1.4.** Basic plasma assisted etching mechanisms (Flamm and Herb, 1989:19).

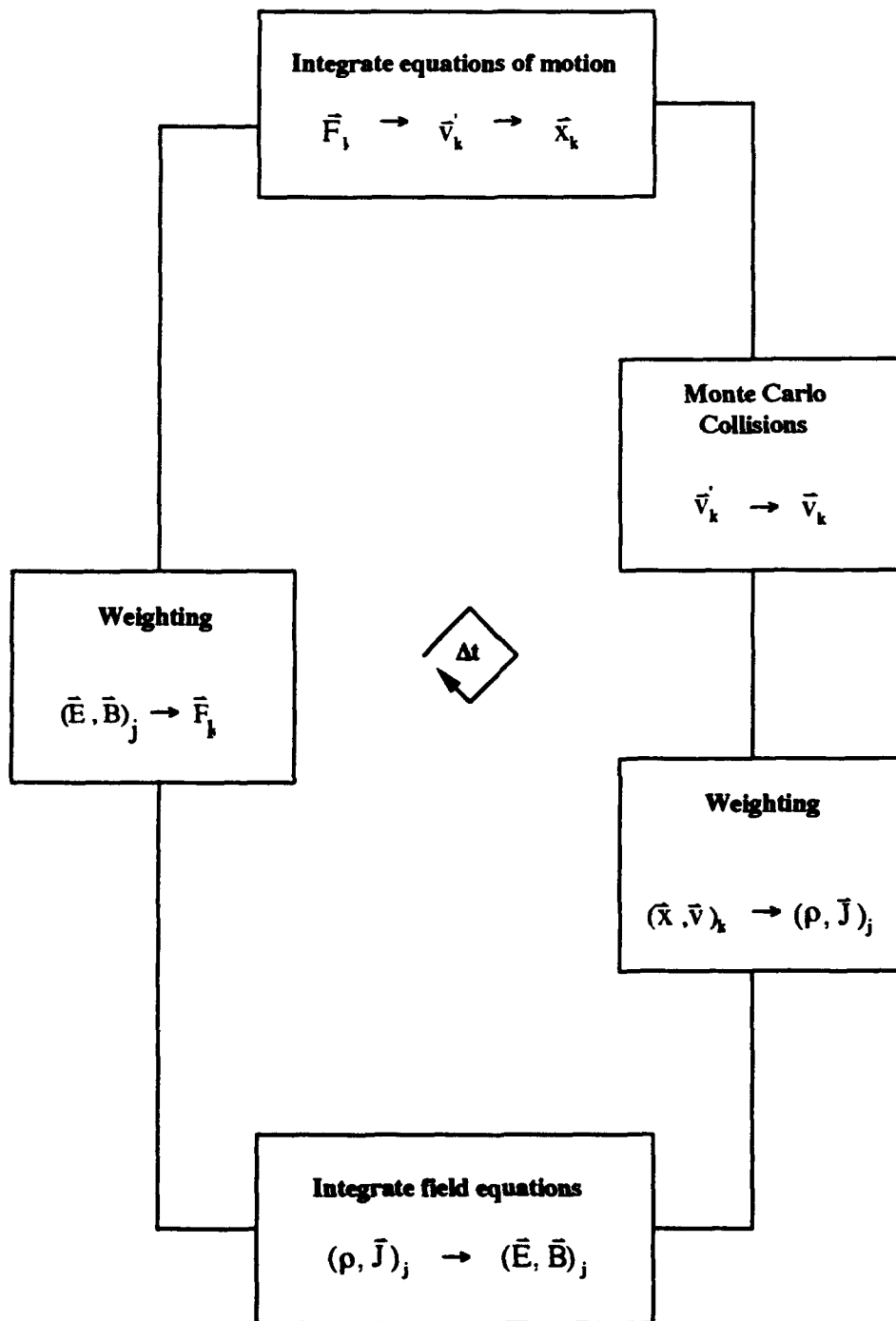


**Figure 2.1.** Computational cycle used in particle simulations with Monte Carlo collisions (Birdsall, 1990:81).



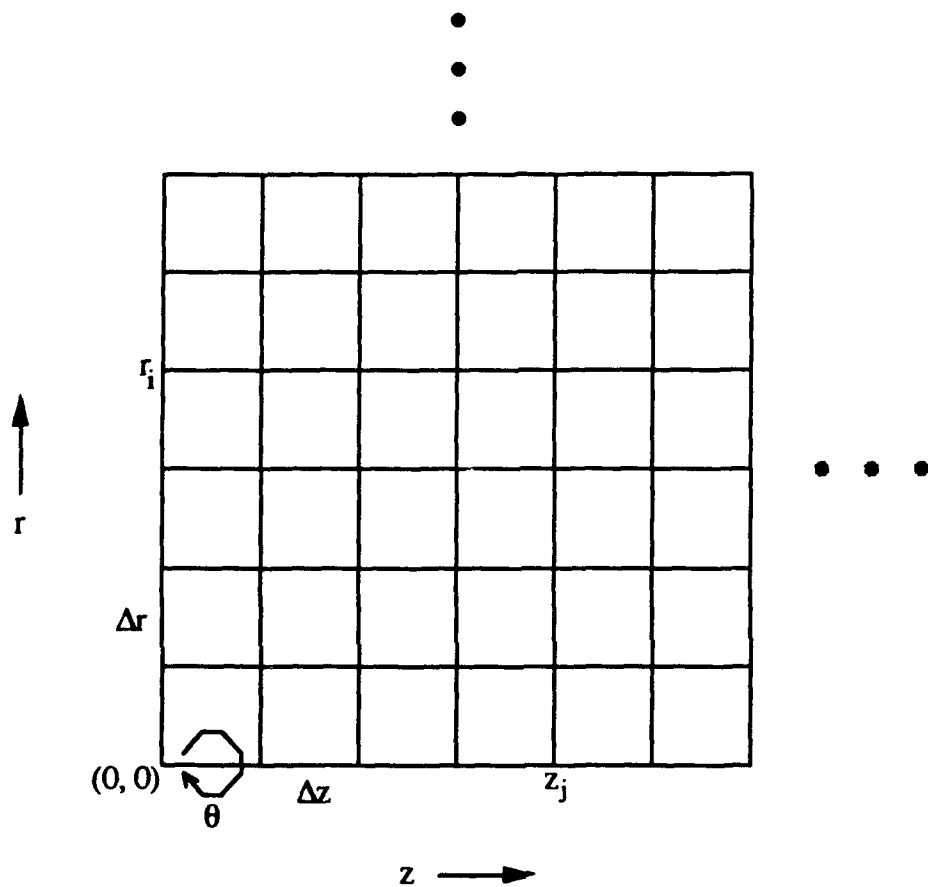


**Figure 2.2.** Spatial grid used in the model. Charge, charge density, potential, and electric field components are calculated at each grid point.

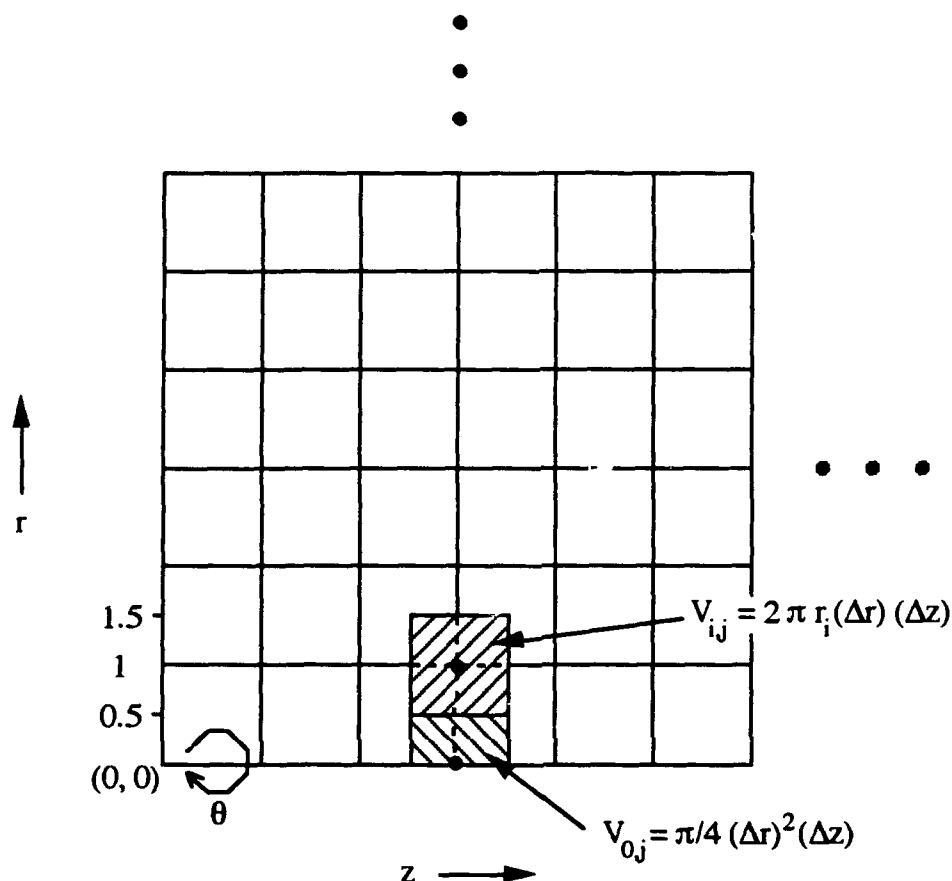


**Figure 2.3.** Volume elements used in forming the charge density. The charge density is weighted to the dots centered on the column elements at the grid points. The volume elements associated with on-axis grid points have a different form than the off-axis elements (Birdsall and Langsdon, 1990:333).

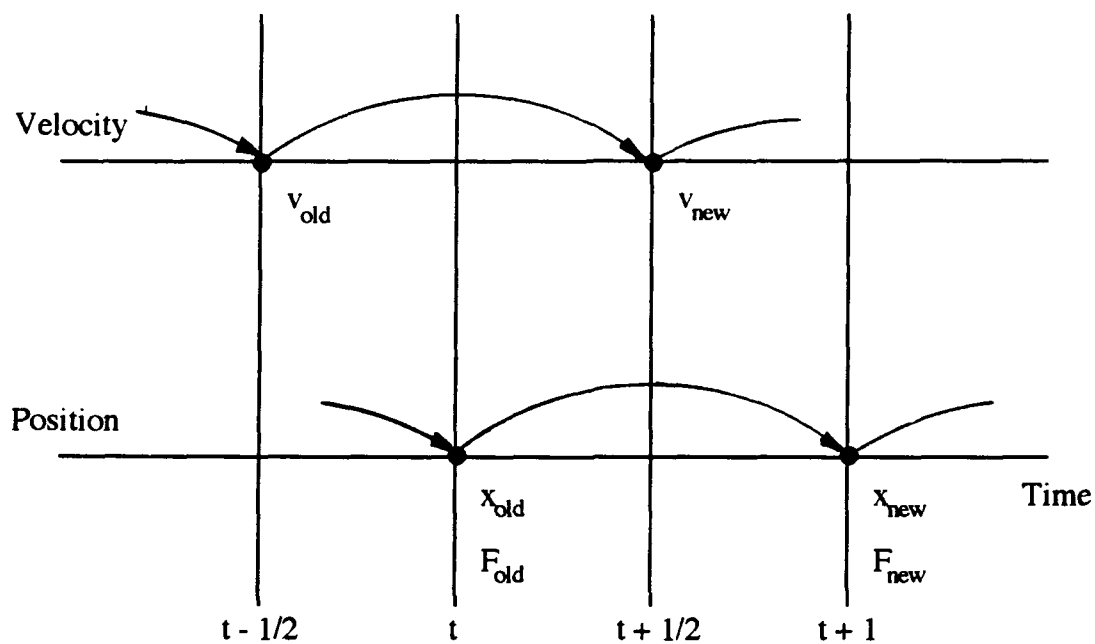


**Figure 2.4.** Pictorial representation of the leapfrog integration scheme. Note that the forces and positions are known at integral time-steps while the velocities are known at half-integral time-steps (Birdsall and Langsdon, 1991:13).

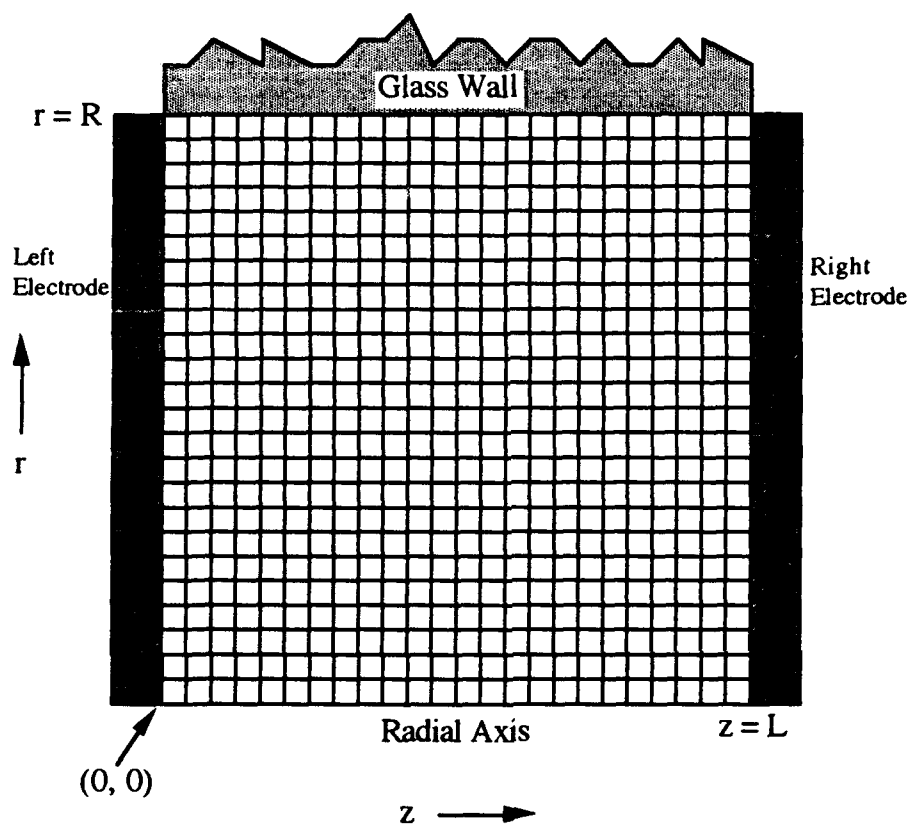


**Figure 2.5.** Grid with boundaries shown. The boundary at  $z = 0$  corresponds to the left electrode while the boundary at  $z = L$  corresponds to the right electrode. The boundary at  $r = R$  is the glass wall of the discharge tube.

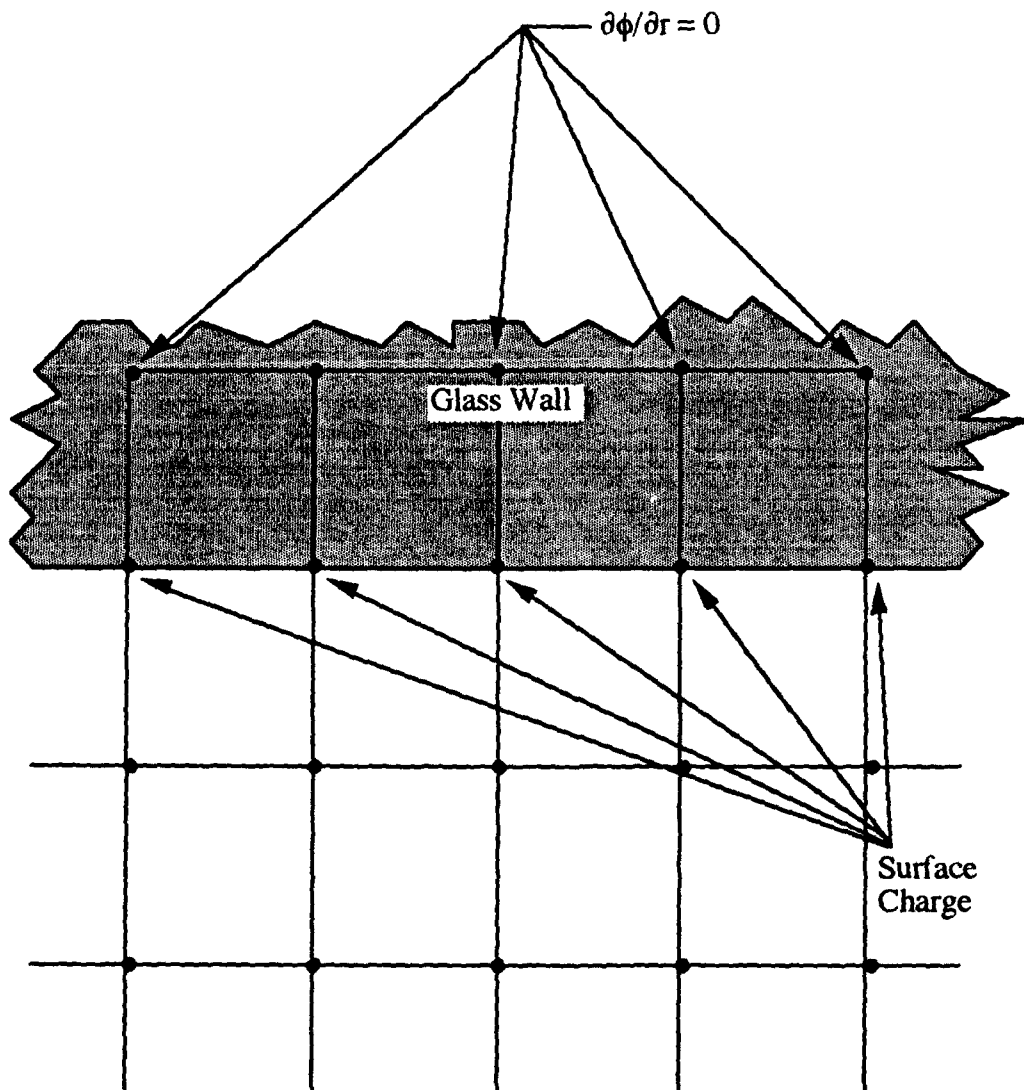


**Figure 2.6.** Boundary at  $r = R$ . A surface charge accumulates in the grid points at the glass wall, behind which the normal components of the electric field is set to zero (Hockney, 1966, 1829).

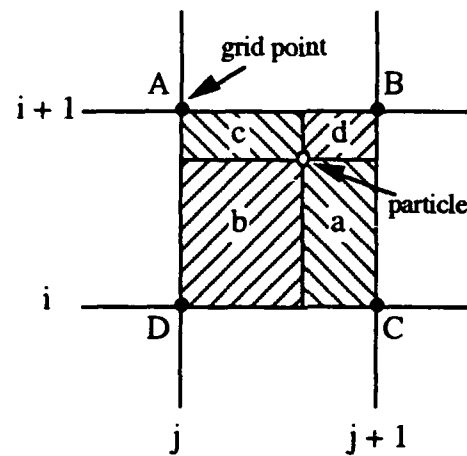


**Figure 2.7.** Diagram used to explain the bilinear and volume weighting schemes (Birdsall and Langdon, 1991:309).

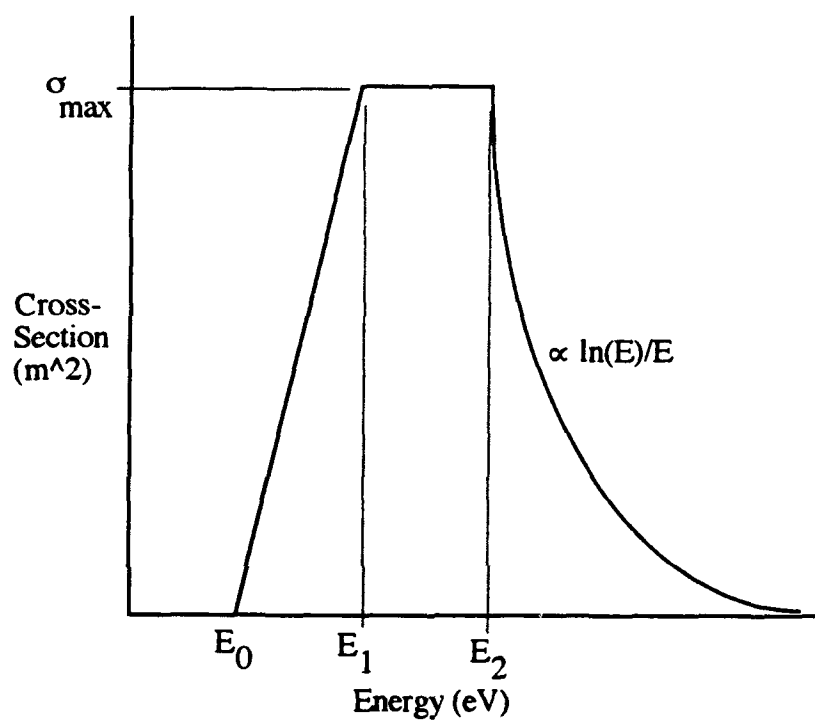


**Figure 2.8.** Form of ionization collision cross-section with parameters discussed in text (Birdsall, 1991:81).

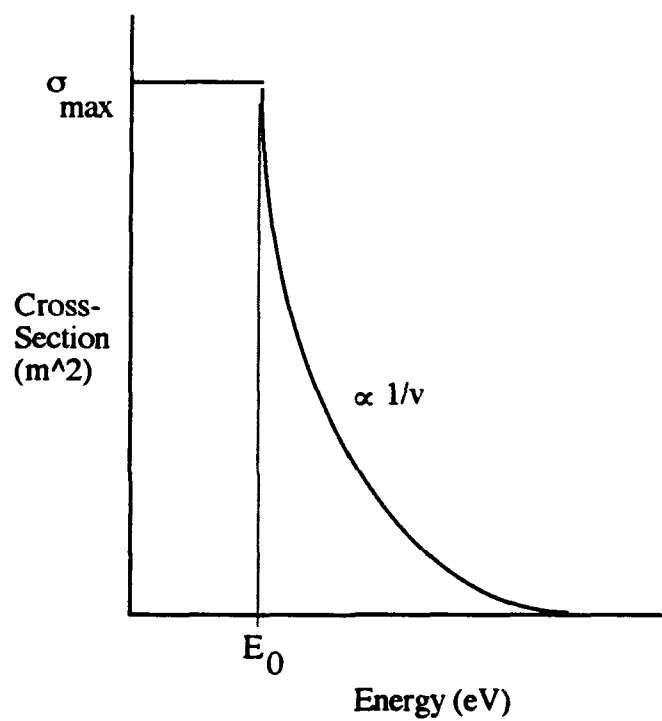


**Figure 2.9.** Form of elastic collision cross-section with parameters discussed in text (Birdsall, 1991:81).



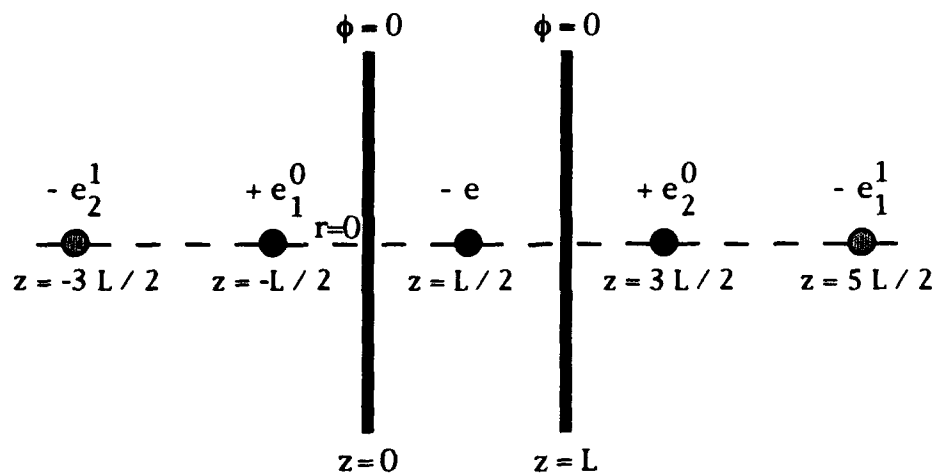


**Figure 3.1.** Location of electron, grounded electrodes and first four image charges for single particle test case 1.

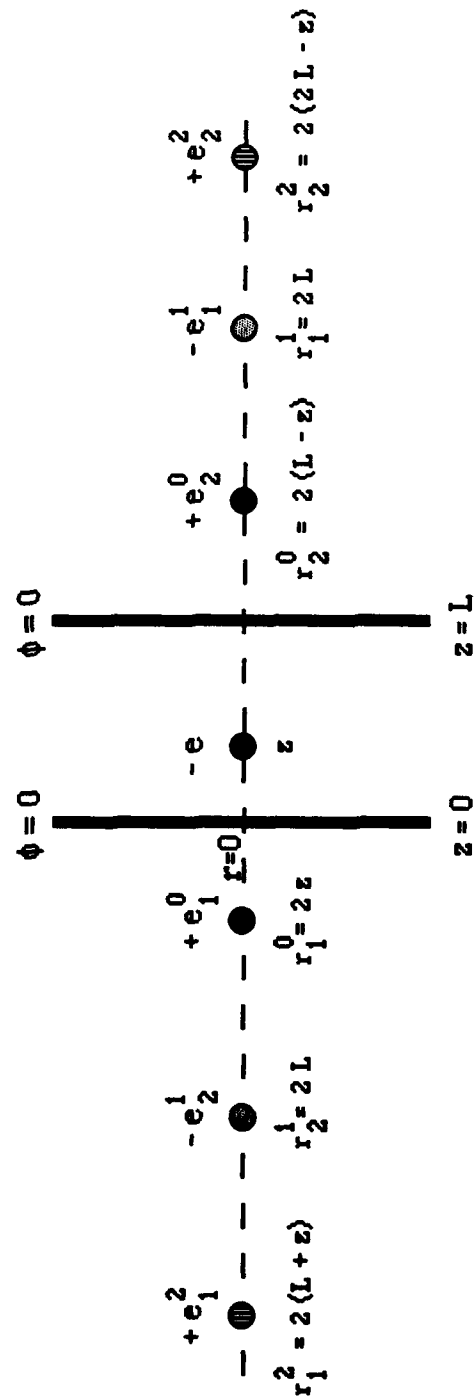


**Figure 3.2.** Location of an electron, grounded electrodes, and six image charges for single particle test case 2. The distance beneath each image charge indicate distance of the image from the electron at  $z$ .

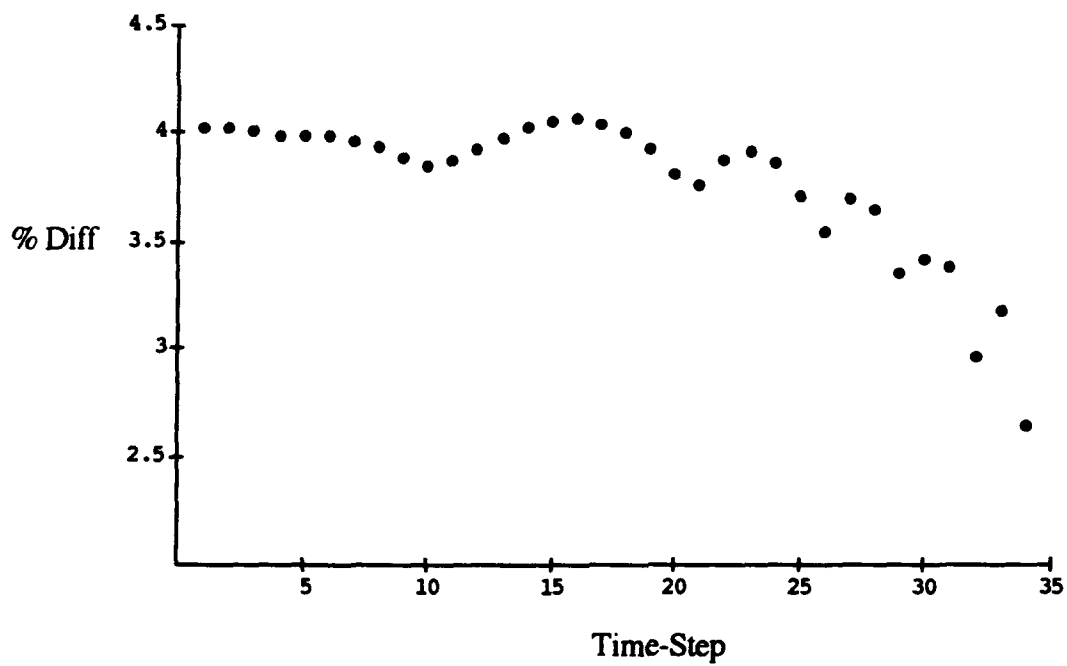


**Figure 3.3.** Percent difference between analytically calculated and model calculated acceleration vs simulation time-step for single particle test case 2 using bilinear weighting.

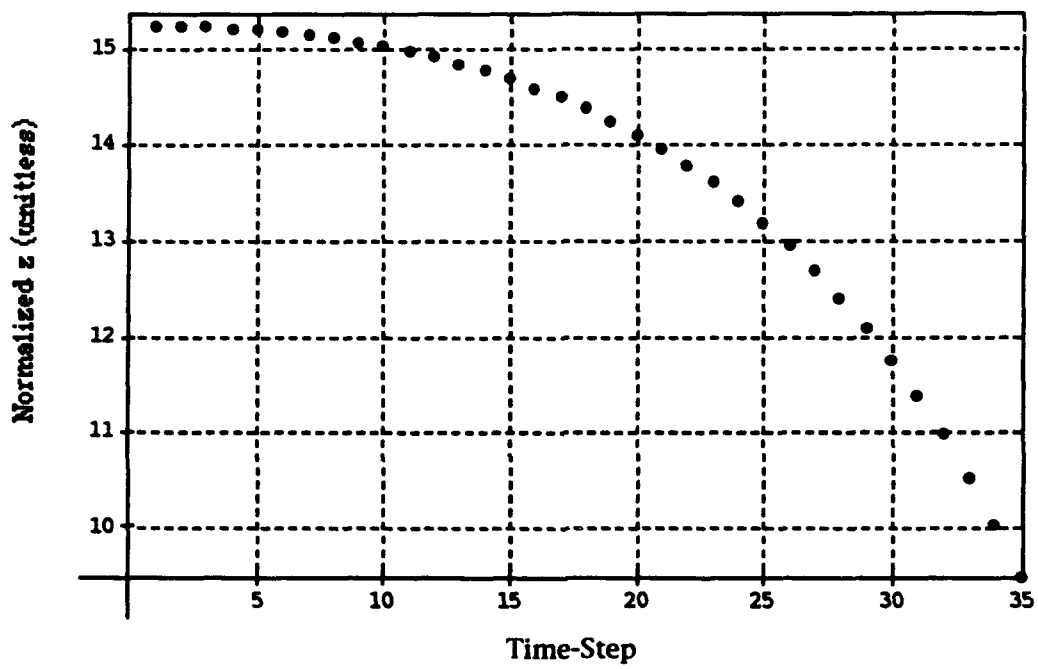


**Figure 3.4.** Normalized z-component of position vs simulation time-step for single particle test case 2 using bilinear weighting.

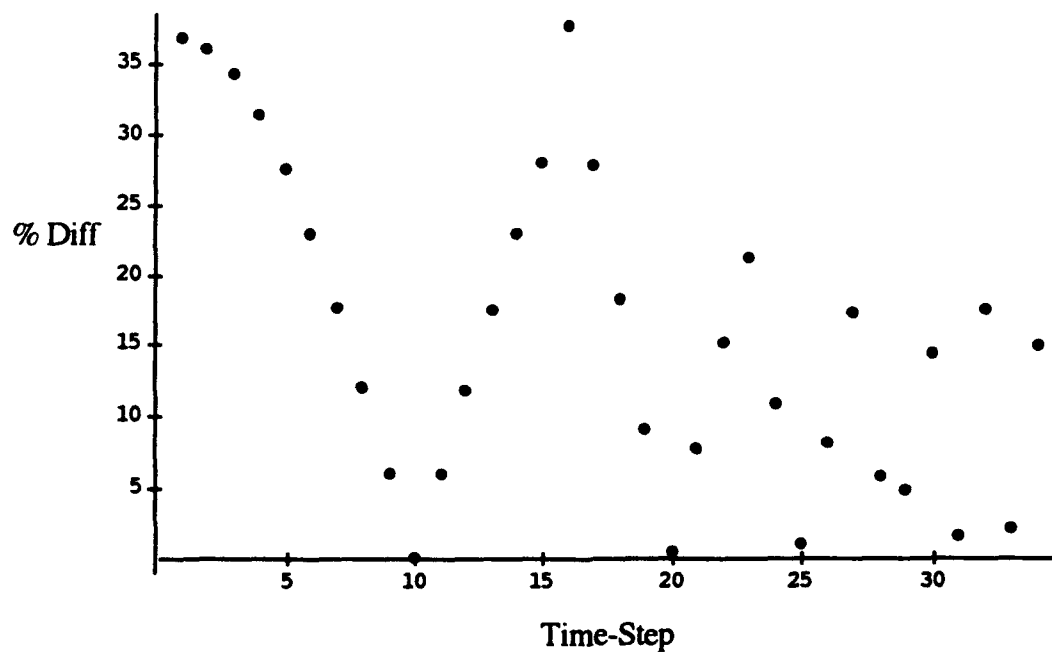


**Figure 3.5.** Percent difference between analytically calculated and model calculated acceleration vs simulation time-step for single particle test case 2 using NGP weighting.

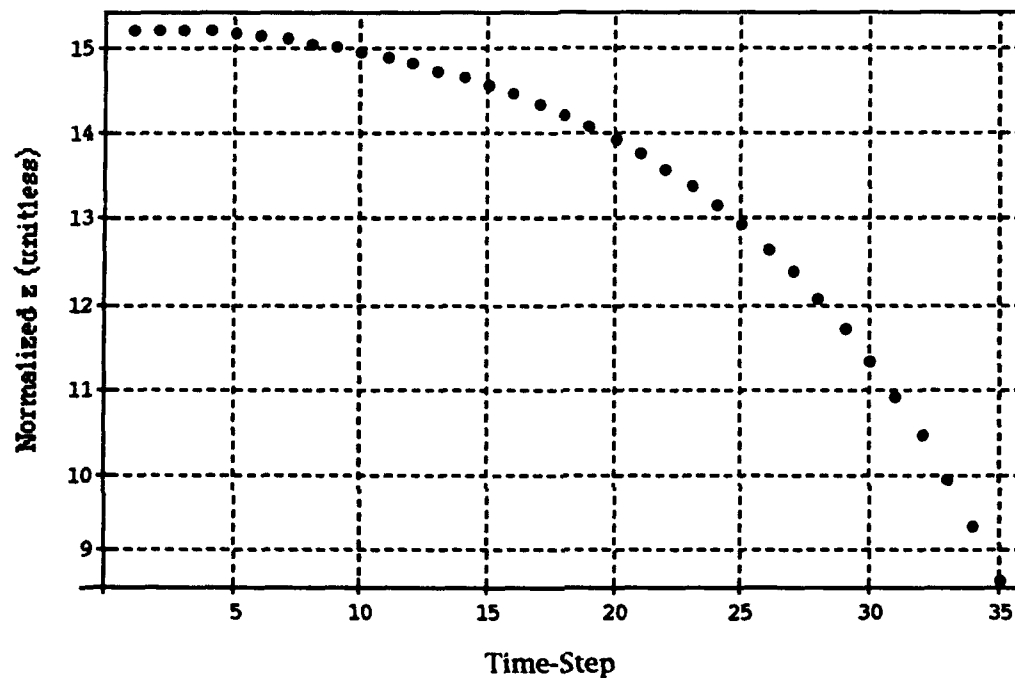


**Figure 3.6.** Normalized z-component of position vs simulation time-step for single particle test case 2 using NGP weighting.

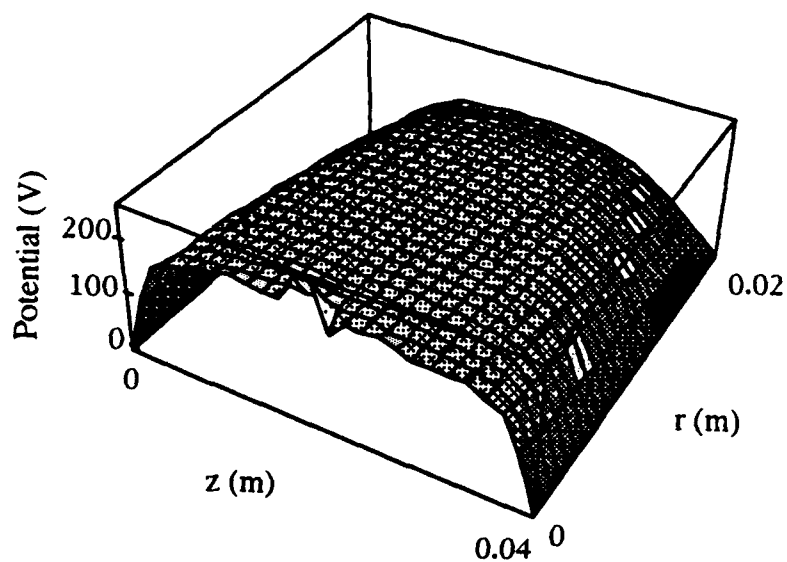


**Figure 3.7.a.** Potential at the start of the eleventh RF cycle. Note the on-axis noise.

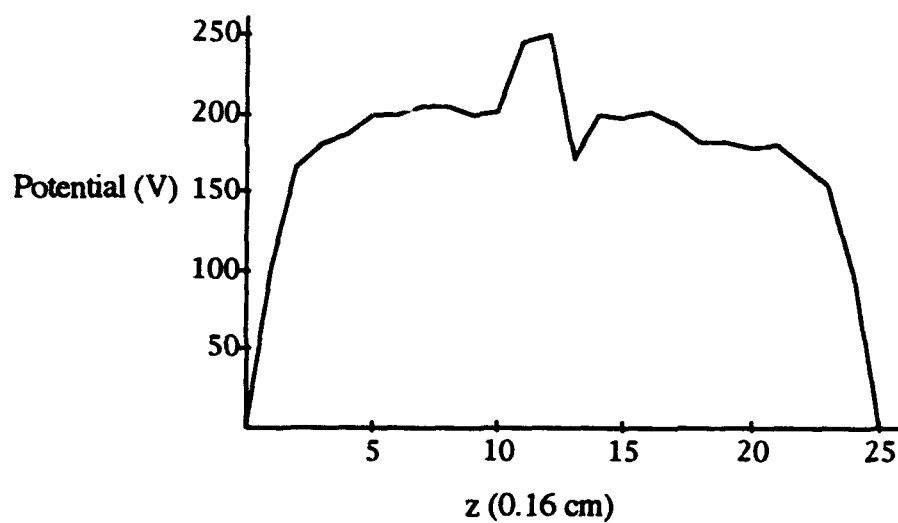


**Figure 3.7.b.** One dimensional slice at constant radius ( $r = 0$ ) of potential shown in figure 3.7.a.

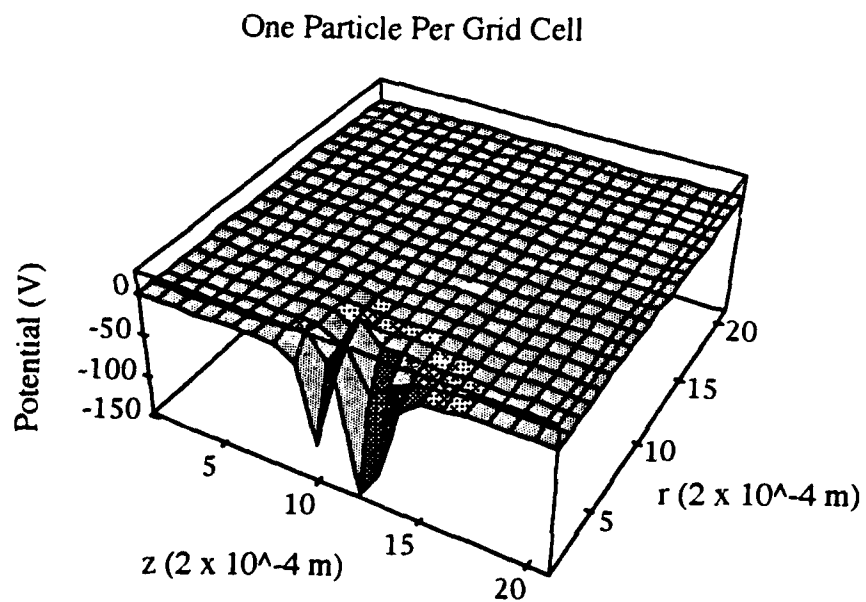


**Figure 3.8.a.** Potential for conditions discussed in chapter three with one particle per grid cell.

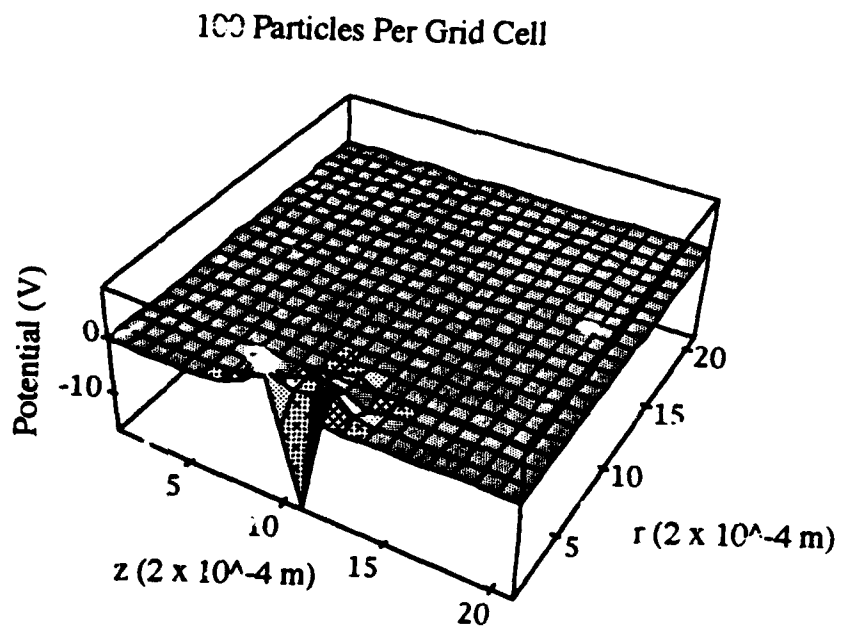


**Figure 3.8.b.** Potential for conditions discussed in chapter three with 100 particles per grid cell.



1000 Particles Per Grid Cell

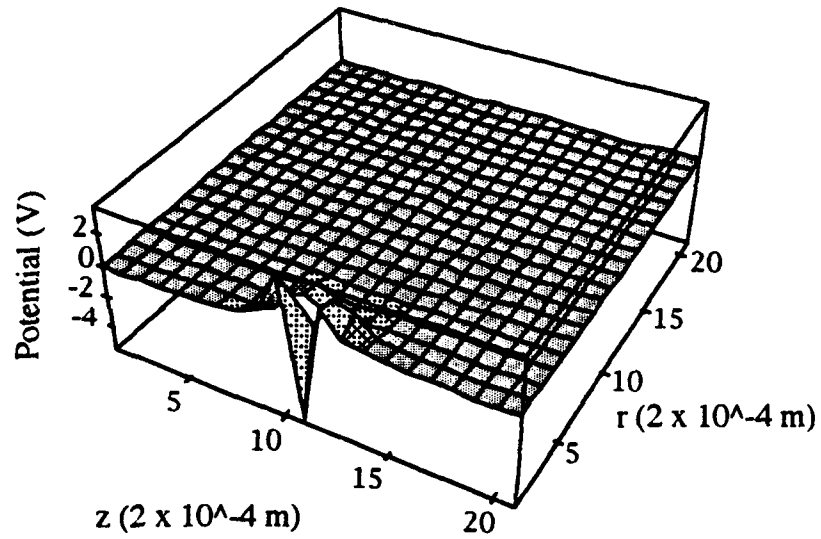


**Figure 3.8.c.** Potential for conditions discussed in chapter three with 1000 particles per grid cell.

1000 Particles Per Grid Cell

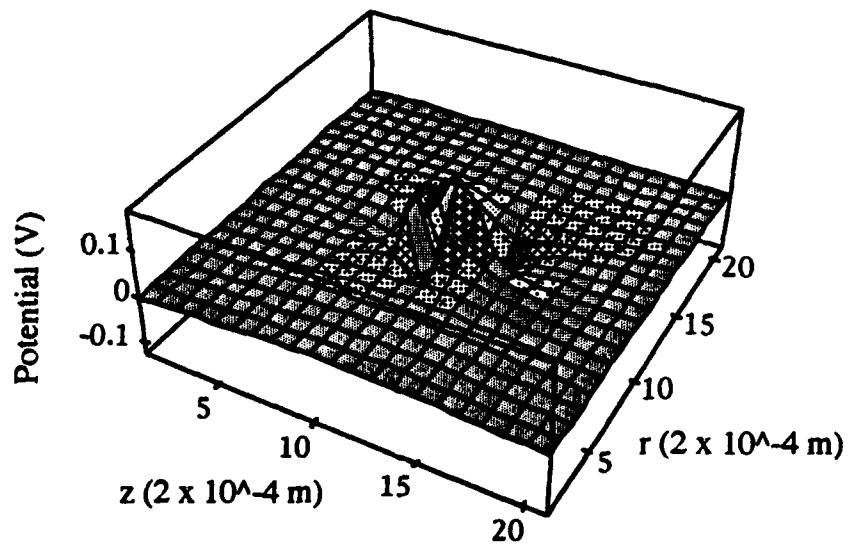


**Figure 3.8.d.** Potential for particles placed off-axis with 1000 particles per grid cell.

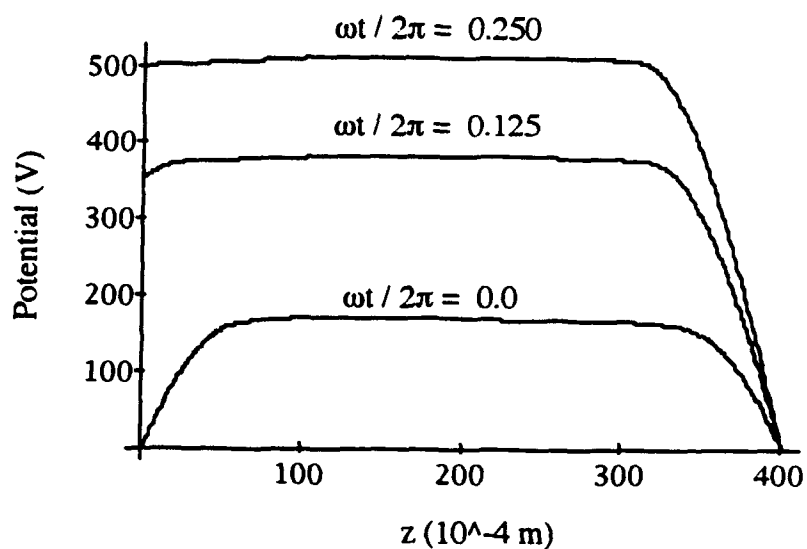


**Figure 3.9.a.** Potential as a function of position within the discharge at three times between the beginning and one-quarter of the way through the RF cycle.

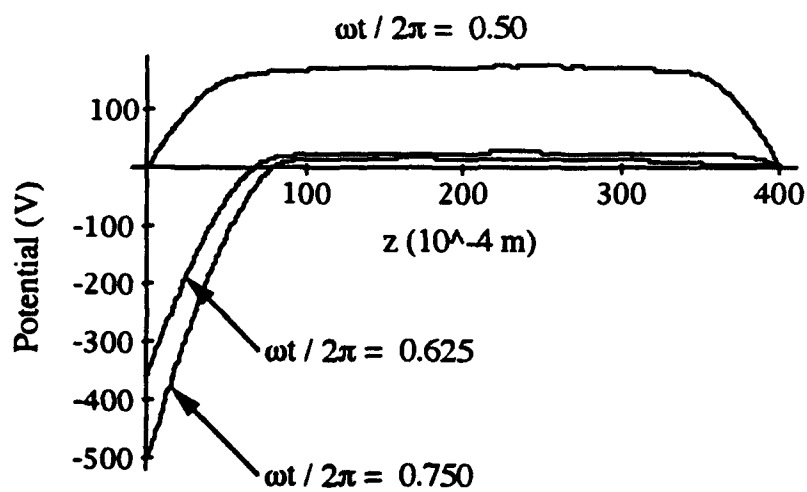


**Figure 3.9.b.** Potential as a function of position within the discharge at three times between one-half and three-quarters of the way through the RF cycle.

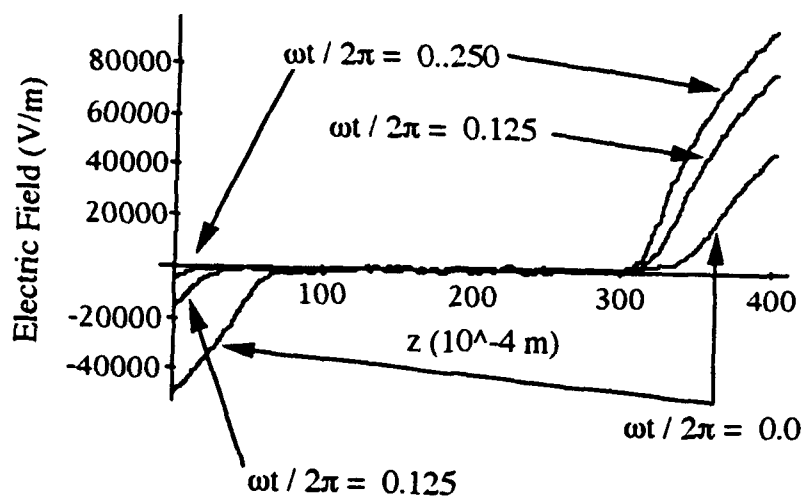


**Figure 3.10.a.** Electric field as a function of position within the discharge at three times between the beginning and one-quarter of the way through the RF cycle.

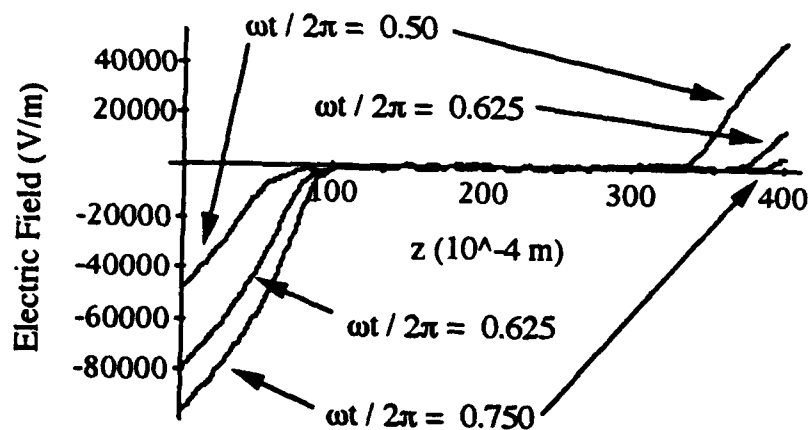


**Figure 3.10.b.** Electric field as a function of position within the discharge at three times between one-half and three-quarters of the way through the RF cycle.

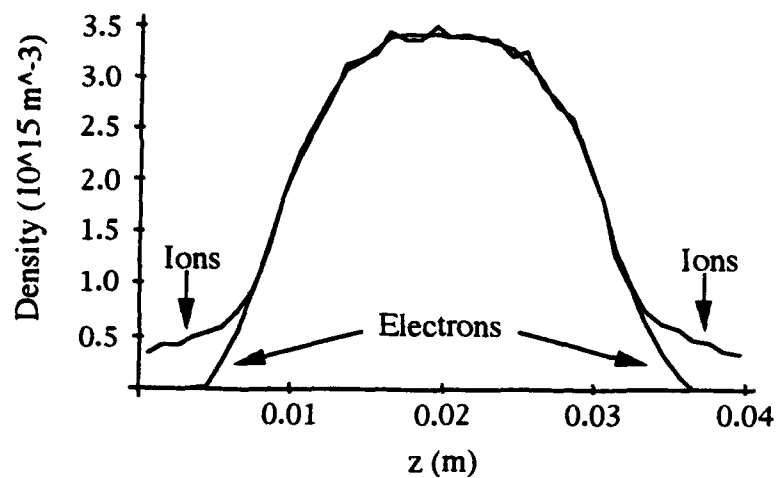


**Figure 3.11.a.** Charged particle densities as a function of position in the discharge at the beginning of an RF cycle.

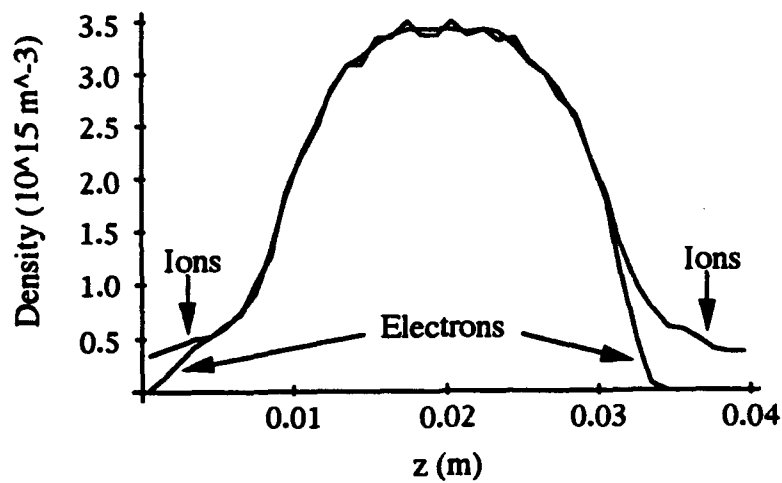


**Figure 3.11.b.** Charged particle densities as a function of position in the discharge one-eighth of the way through an RF cycle.

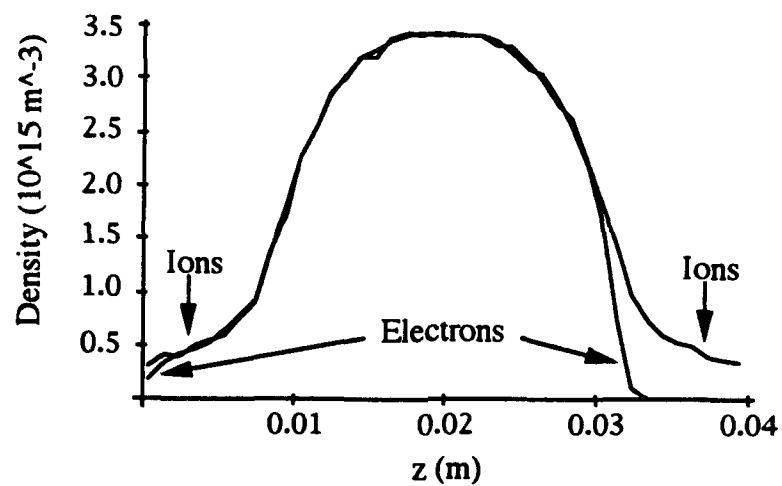


**Figure 3.11.c.** Charged particle densities as a function of position in the discharge one-quarter of the way through an RF cycle.

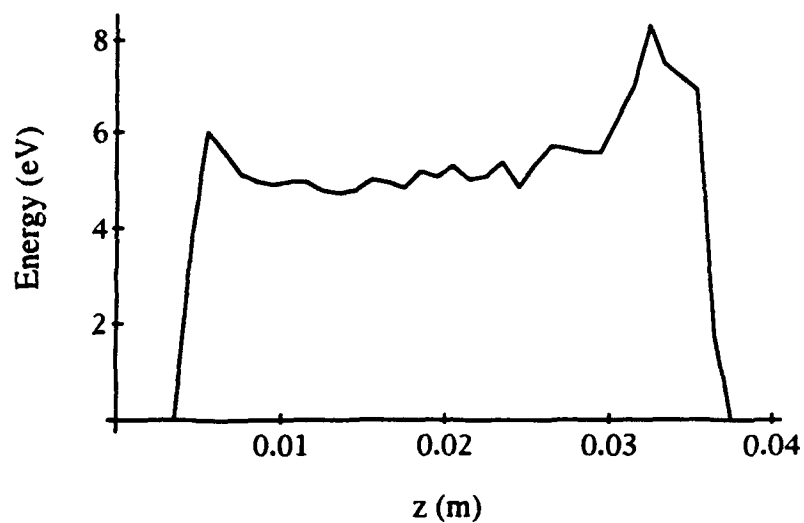


**Figure 3.12.a.** Average electron energy as a function of position within the discharge at  $\omega t / 2\pi = 0.0$ .

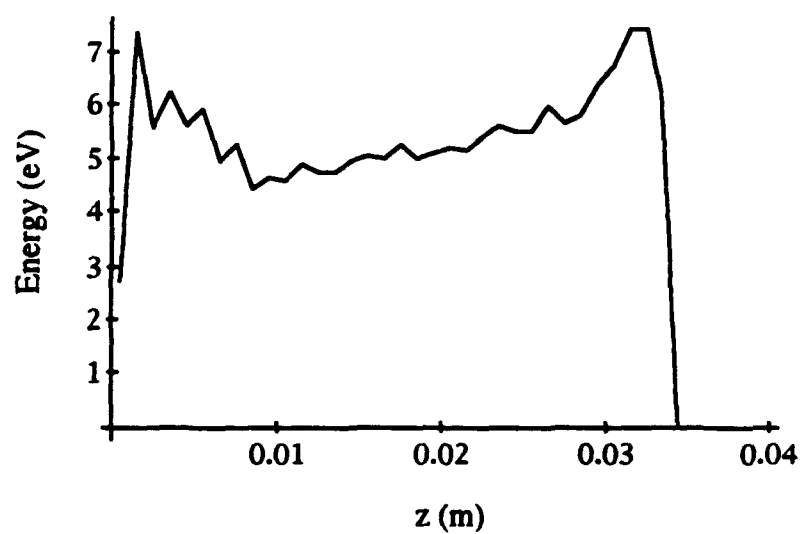


**Figure 3.12.b.** Average electron energy as a function of position within the discharge at  $\omega t / 2\pi = 0.125$ .

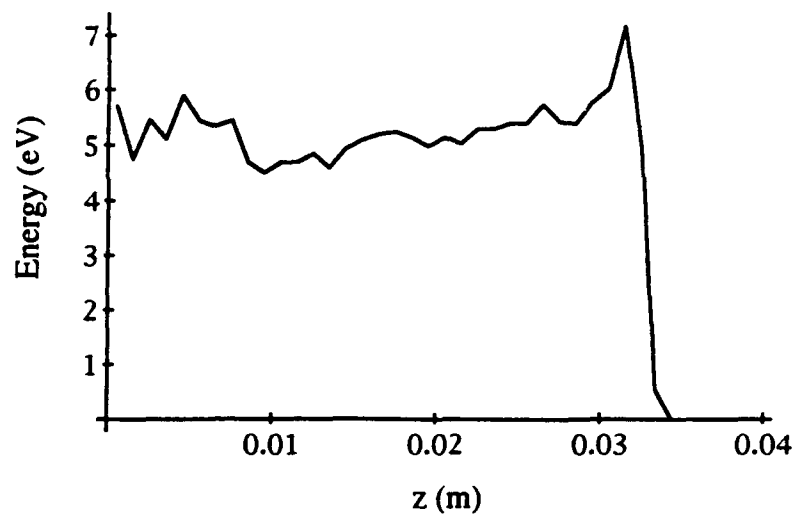


**Figure 3.12.c.** Average electron energy as a function of position within the discharge at  $\omega t / 2\pi = 0.25$ .

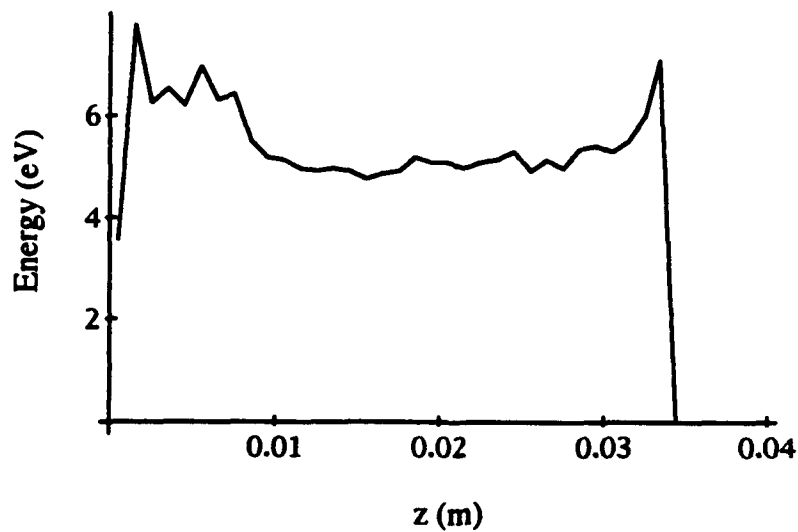


**Figure 3.12.d.** Average electron energy as a function of position within the discharge at  $\omega t / 2\pi = 0.375$ .

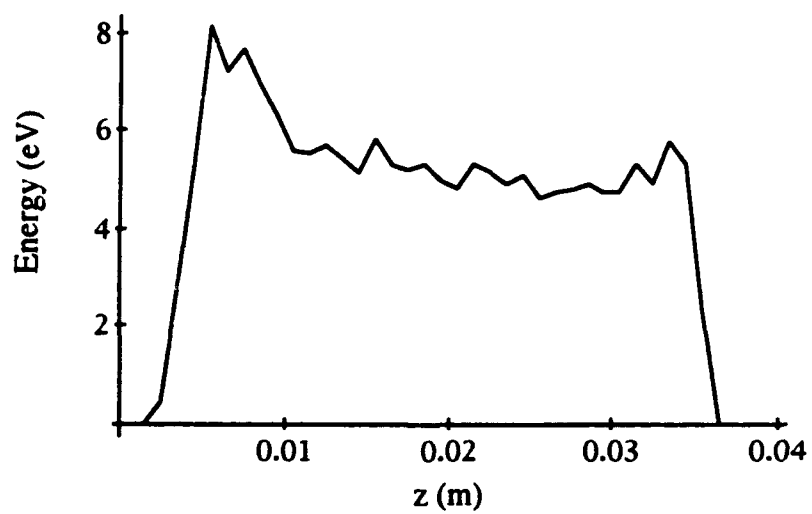


**Figure 3.12.e.** Average electron energy as a function of position within the discharge at  $\omega t / 2\pi = 0.5$ .



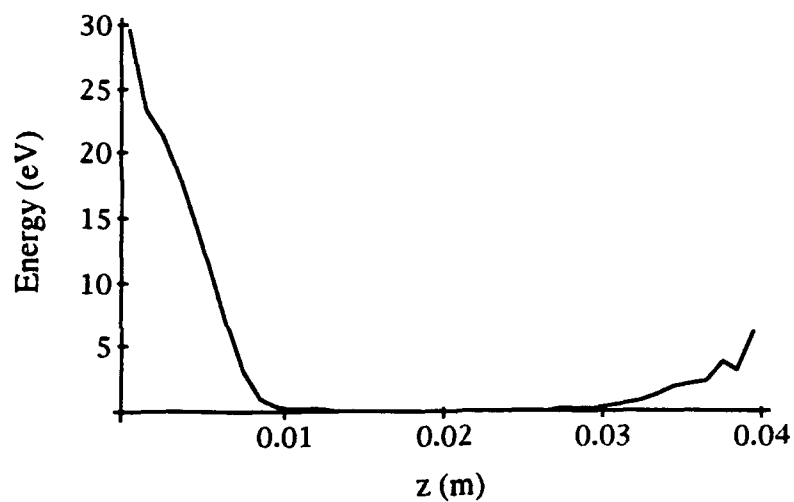


**Figure 3.13.a.** Average ion energy as a function of position within the discharge at beginning of RF cycle.

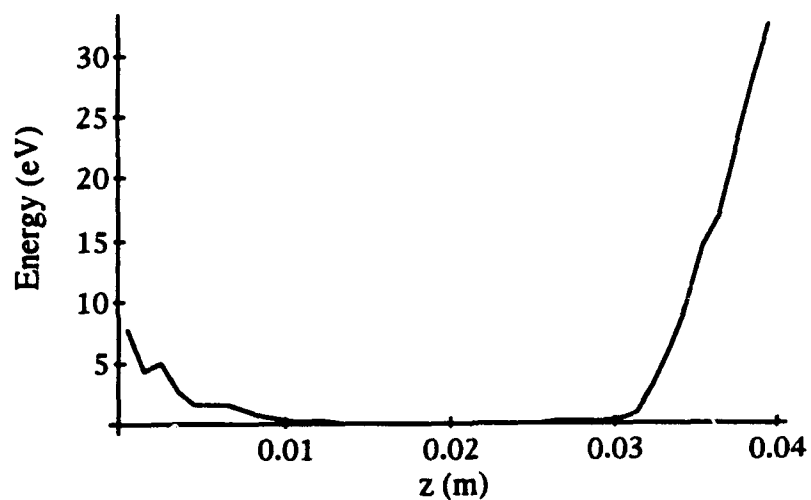


**Figure 3.13.b.** Average ion energy as a function of position within the discharge midway through the RF cycle.

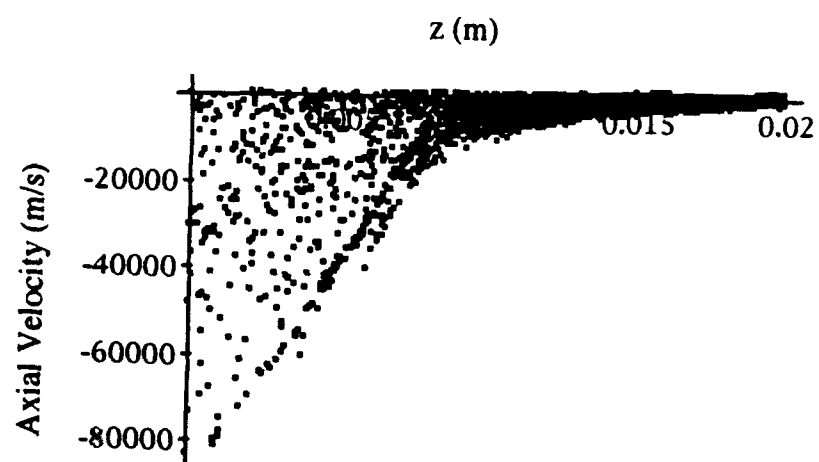


**Figure 3.14.** Ion  $z$ - $v_z$  phase space for the left half of the discharge ( $0 \text{ m} \leq z \leq 0.02 \text{ m}$ ).

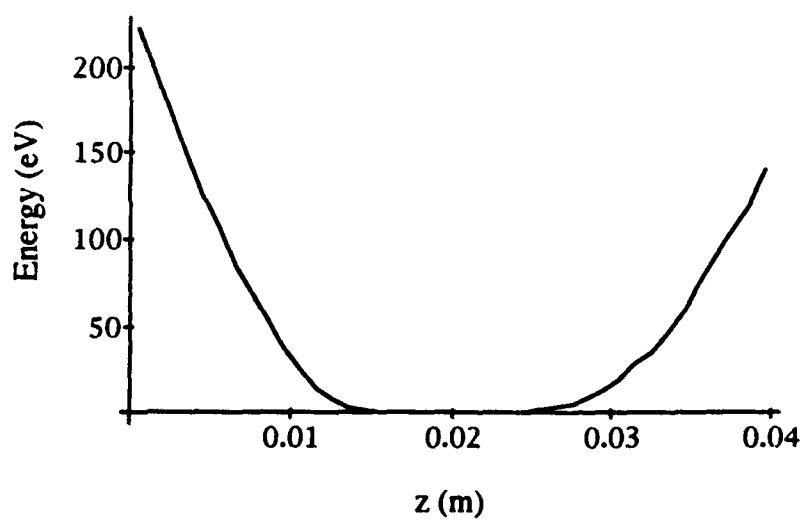


**Figure 3.15.** Average ion energy at the beginning of the RF cycle as a function of position within the discharge for the case with no ion collisions.

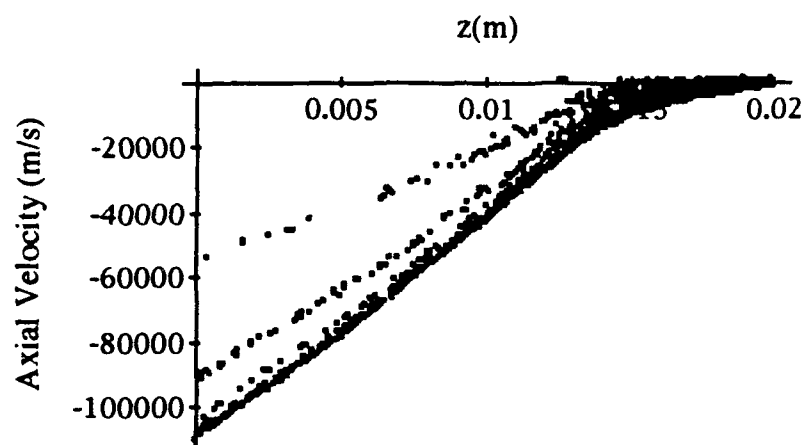


**Figure 3.16.** Ion  $z$ - $v_z$  phase space at the beginning of the RF cycle for the case with no ion collisions for the left half of the discharge ( $0 \text{ m} \leq z \leq 0.02 \text{ m}$ ).

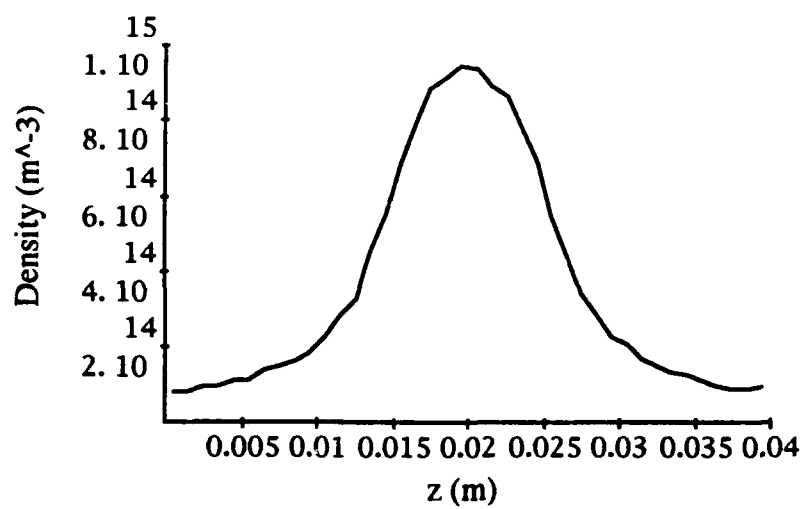


**Figure 3.17.** Average ion density at the beginning of the RF cycle as a function of position within the discharge for the case with no ion collisions .

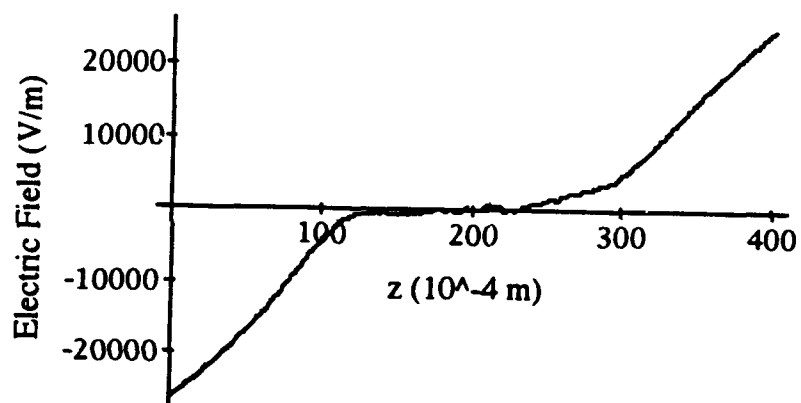


**Figure 3.18.** Electric field at the beginning of the RF cycle for the case with no ion collisions.

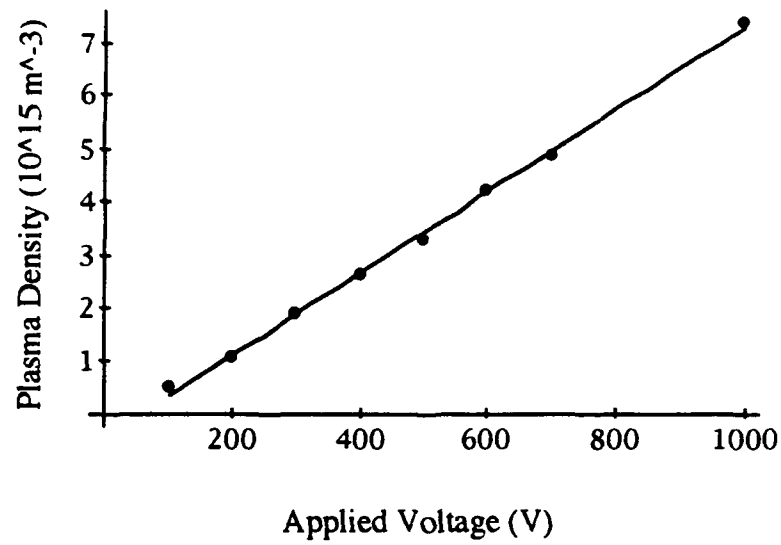


**Figure 3.19.** Plasma density as a function of applied voltage with the fit line  $n \propto V_{RF}$  shown .

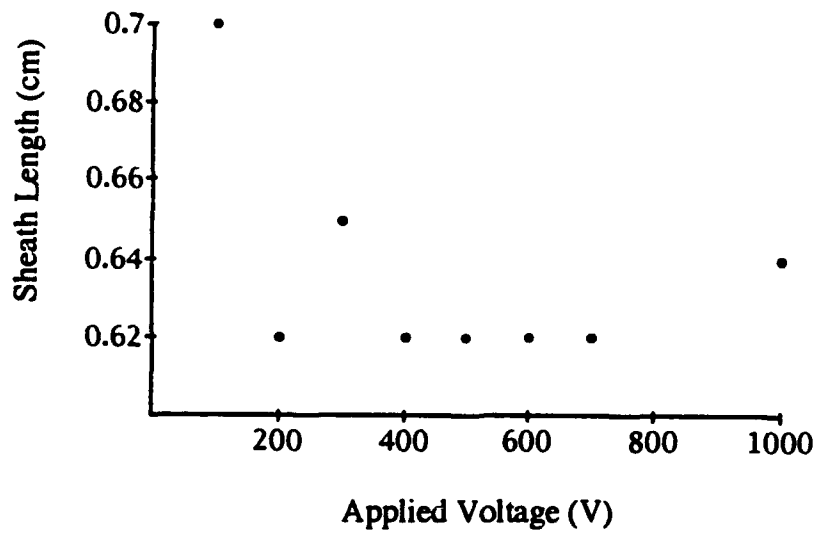


**Figure 3.20.** Sheath length (at  $\omega t / 2\pi = 0$ ) as a function of applied voltage.

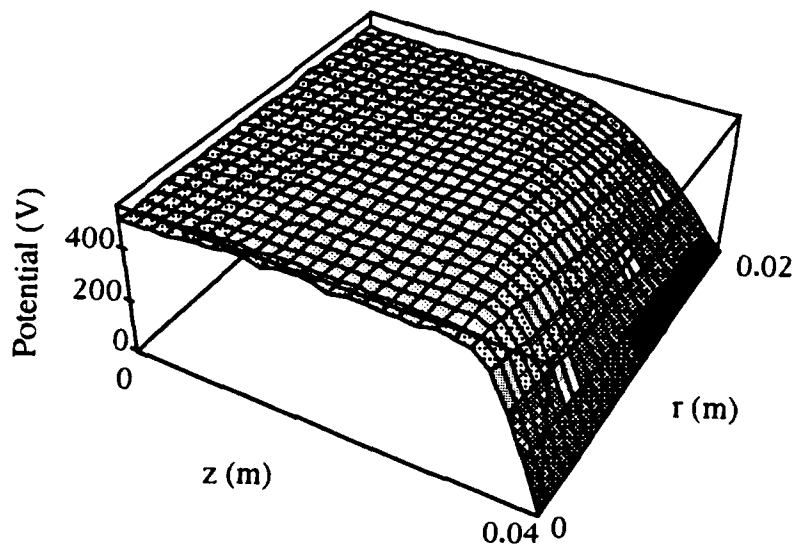


**Figure 3.21.a.** Potential as a function of position within the discharge at  $\omega t / 2\pi = 0.25$  for the two-dimensional case.

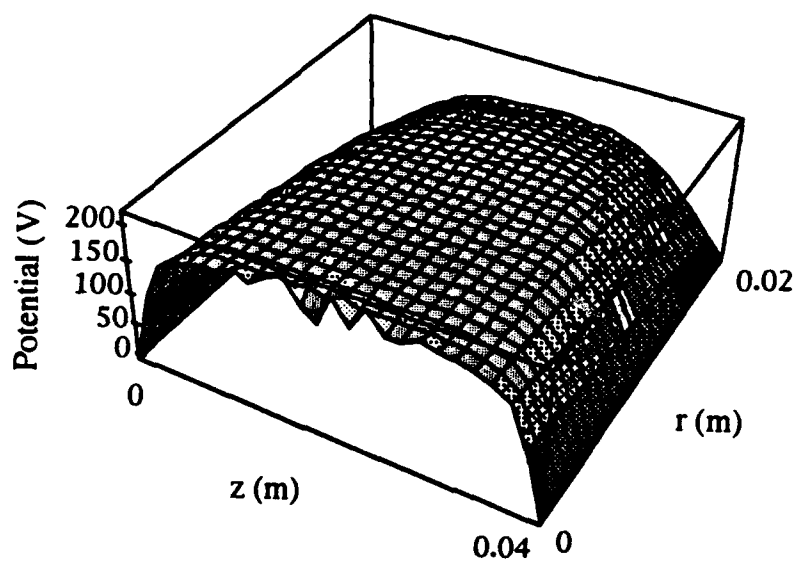


**Figure 3.21.b.** Potential as a function of position within the discharge at  $\omega t / 2\pi = 0.5$  for the two-dimensional case.



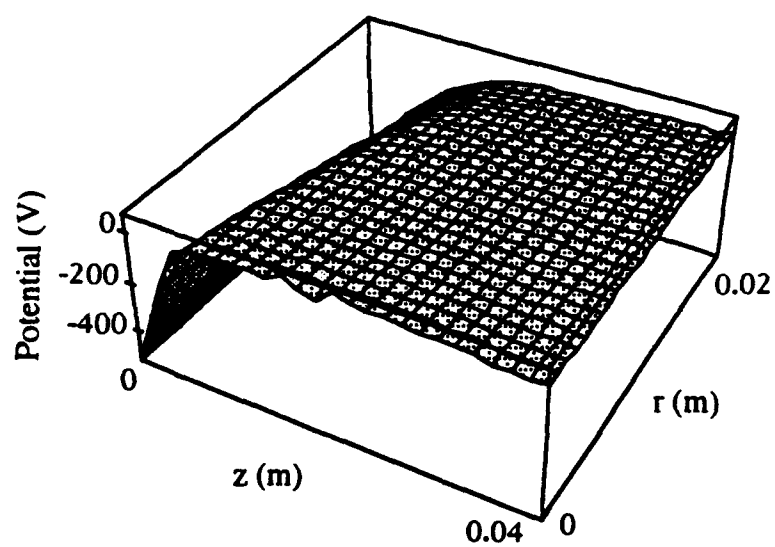


**Figure 3.21.c.** Potential as a function of position within the discharge at  $\omega t / 2\pi = 0.75$  for the two-dimensional case.

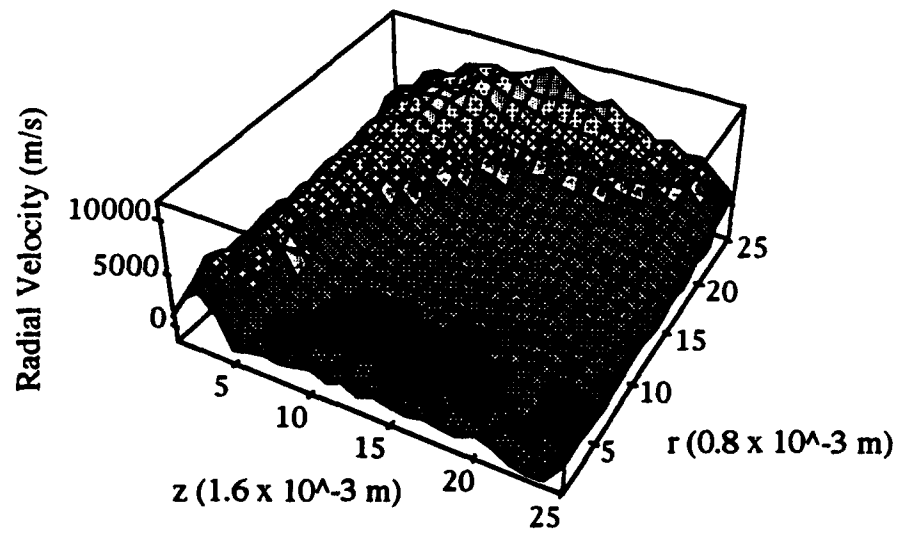


**Figure 3.22.** Average ion radial velocity as a function of position within the discharge at the beginning of an RF cycle for the two-dimensional case.

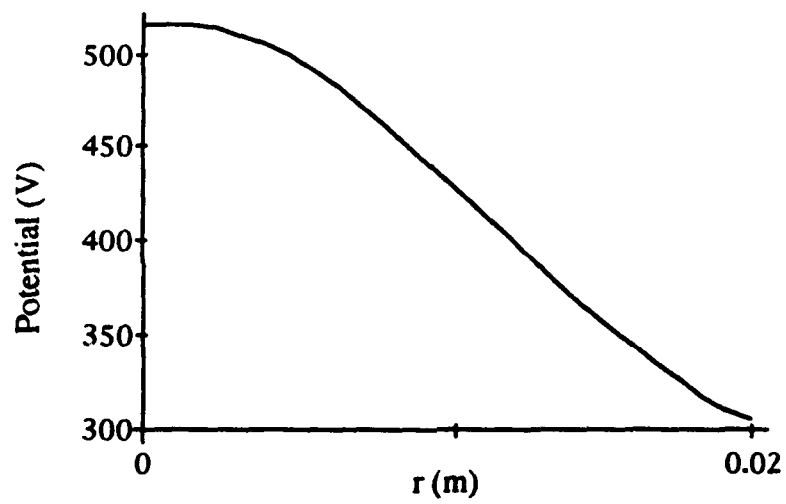


**Figure 3.23.** One-dimensional radial profile of the potential at constant  $z = 3.5$  cm at  $\omega t / 2\pi = 0.25$  for the two-dimensional case.

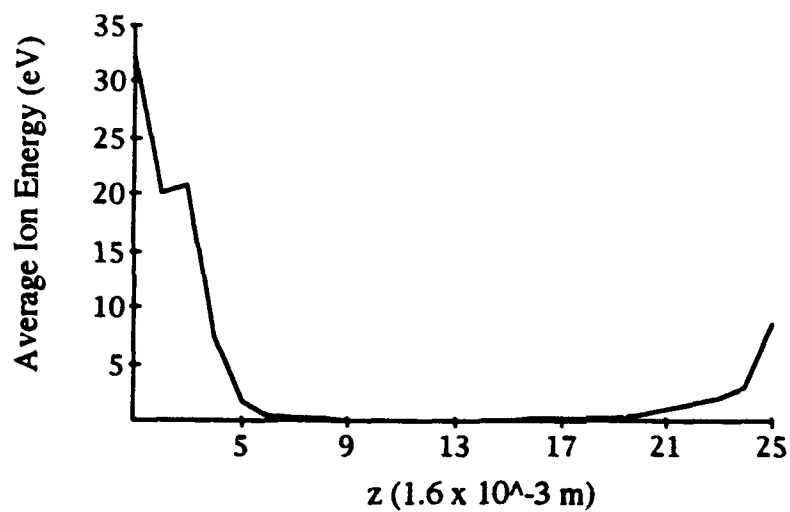


**Figure 3.24.** Average ion energy as a function of axial position within the discharge at constant  $r = 2.4$  mm at the beginning of an RF cycle for the two-dimensional case.

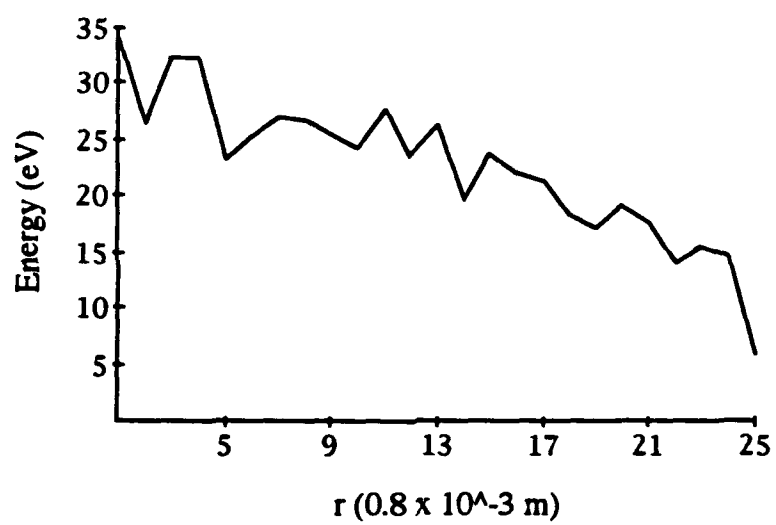


**Figure 3.25.** Average ion energy across the left electrode for the two-dimensional case.

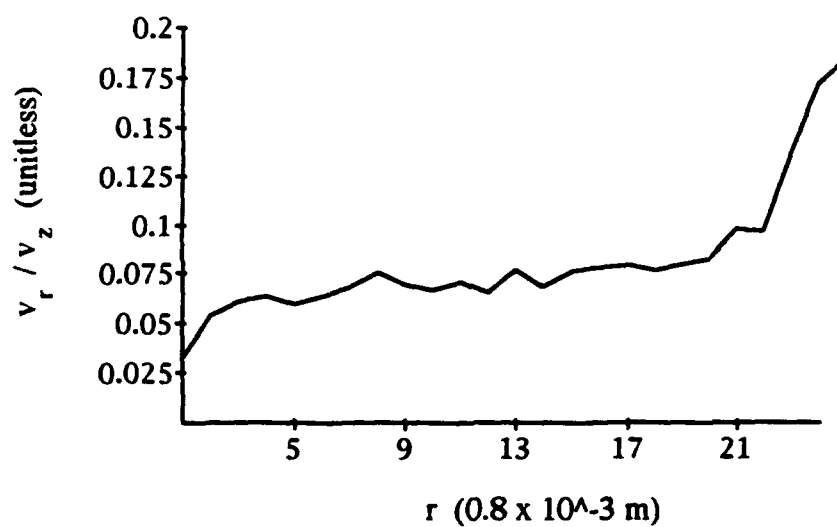


**Figure 3.26.** Average ratio of the radial and axial velocity components for ions at the left electrode ( $z = 0$ ) at the beginning of an RF cycle for the two-dimensional case.

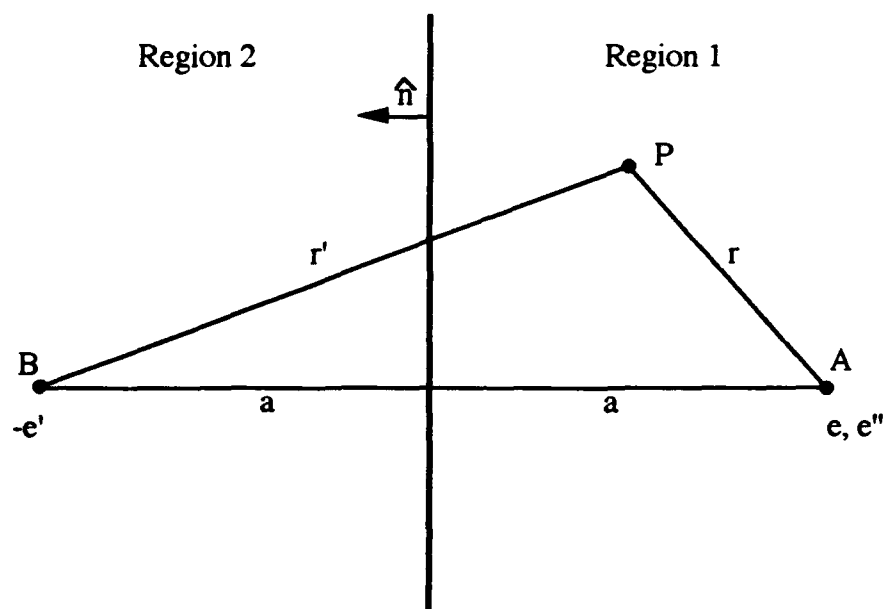


**Figure A.1.** Diagram referred to in appendix A (Becker, 1964:99-100).

## Bibliography

- Adams, John, and others. *FISHPAK A Package of FORTRAN Subprograms for the Solution of Elliptic Partial Differential Equations., version 3.2* Computer Source Code. Boulder, CO: National Center for Atmospheric Research, November, 1988.
- Barnes, Michael Scott. *Computer Modeling of RF Glow Discharges for the Study of Plasma Processing in Microelectronics*. Ph.D. dissertation. The University of Michigan, 1988 (ON 8812855).
- Becker, Richard. *Electromagnetic Fields and Interactions*. New York: Dover Publications, Inc., 1964.
- Birdsall, C. K. "Particle-in-Cell Charged Particle Simulations, Plus Monte Carlo Collisions With Neutral Atoms, PIC-MCC," *IEEE Transactions on Plasma Science*, 19: 65 - 85 (April 1991).
- Birdsall, C. K and Langdon, A. B. *Plasma Physics via Computer Simulation*. Bristol: IOP Publishing Ltd., 1991.
- Boeuf, J. P. and Belenger Ph. "Fundamental Properties of RF Glow Discharges: An Approach Based on Self-Consistent Numerical Models," *Non-Equilibrium Processes in Partially Ionized Gases (NATO ASI Series)*, edited by M. Capitelli and J. M. Bardsley. New York: Plenum, 1990.
- Boswell, R. W. and Morey, I.J. "Self-Consistent Simulation of a Parallel-Plate RF Discharge," *Applied Physics Letters*, 52: 21 - 23 (January 1988).
- Burger, Peter. "Elastic Collisions in Simulating One-Dimensional Plasma Diodes on the Computer," *The Physics of Fluids*, 10: 658 - 666 (March 1967).
- Feynman, Richard P. and others. *The Feynman Lectures on Physics, Volume II, Mainly Electromagnetism and Matter*. Reading, MA: Addison-Wesley, 1964.
- Flamm, Daniel L. and Herb, G. Kenneth. "Plasma Etching Technology -- An Overview," *Plasma Etching An Introduction*, edited by Daniel L. Flamm and Dennis M. Manos. Boston: Academic Press, Inc., 1989.
- Golant, V.E., and others. *Fundamentals of Plasma Physics*. NY: John Wiley and Sons, 1980.
- Goldstein, Herbert. *Classical Mechanics*. Reading, MA: Addison-Wesley, 1980.
- Gill, E.W.B and Donaldson, R.H. "The Sparking Potential of Air for High-Frequency Discharges." *Philosophical Magazine and Journal of Science*, 12: 719-726 (July-December, 1931).
- Hockney, R.W. *The Computer Simulation of Anomalous Plasma Diffusion and the Numerical Solution of Poisson's Equation*. Ph.D. dissertation. Stanford University, 1966.



- Hockney, R. W. "Computer Experiment of Anomalous Diffusion." *Phys. Fluids*, 9: 1826 - 1835 (September, 1966).
- Hockney, R. W. and Eastwood, J. W. *Computer Simulation Using Particles*. Bristol: IOP Publishing Ltd., 1988.
- Kieffer, L.J. *A Compilation of Electron Collision Cross Section Data for Modeling Gas Discharge Lasers*. Joint Institute for Laboratory Astrophysics Report. University of Colorado, 30 September 1973.
- Lawson, William S. "Particle Simulation of Bounded 1D Plasma Systems," *Journal of Computational Physics*, 80: 253-276 (February 1989).
- McDaniel, E.W. *Collision Phenomena in Ionized Gases*. NY: J. Wiley and Sons, 1964.
- National Research Council, Panel on Plasma Processing of Materials, Plasma Science Committee. *Plasma Processing of Materials: Scientific Opportunities and Technological Challenges*. Washington: National Academy Press, 1991.
- Ramos, David O. *A Simulation of Electric Field Driven Electron Drift Limited by Collisions with Gas Mixtures Using a Monte Carlo Null Collision Technique*. Thesis Defense. Wright State University, 1990.
- Sheridan, T.E. and Goree, J. "Collisional Plasma Sheath Model." *Phys. Fluids B*, 10:2796-2804 (October 1991).
- Shohet, J. Leon. "Plasma-Aided Manufacturing." *IEEE Transactions on Plasma Science*, 19: 725 - 733 (October 1991).
- Smith, Helen. "Application of PIC (Particle-in-Cell) Calculations to Plasma Physics." Presentation to AFIT faculty members. Australian National University Canberra, November 1991.
- Sommerer, Timothy J. "Models of Low Pressure Plasma-Aided Materials Processing." *Paper presented at American Institute of Aeronautics and Astronautics 23rd Plasma Dynamics and Lasers Conference*. General Electric, Corporate Research and Development, Schenectady, NY, July 1992.
- Sommerfeld, Arnold. *Electrodynamics*. New York: Academic Press, 1964
- Surendra, M. and Graves, D.B. "Particle Simulations of Radio-Frequency Glow Discharges." *IEEE Transactions on Plasma Science*, 19: 144 - 157 (April 1991).
- Swarztrauber, Paul and Sweet, Roland. *Efficient FORTRAN Subprograms for the Solution of Elliptic Partial Differential Equations*. NCAR Technical Note TN-109+IA. Boulder, CO: National Center for Atmospheric Research, July 1975.
- Sweet, Roland. "A Cyclic Reduction Algorithm for Solving Block Tridiagonal Systems of Arbitrary Dimension," *SIAM J. Numerical Analysis*, 14: 706 - 720 (September 1977).

Vender, David and Boswell, Rod W. "Numerical Modeling of Low-Pressure RF Plasmas," *IEEE Transactions on Plasma Science*, 18: 725 - 732 (August 1990).

## **Vita**

Captain Eric John Bennett was born on 25 January 1963 in Sussex, New Jersey. He graduated from Minisink Valley High School in Slate Hill, New York in 1981 and attended Ithaca College in Ithaca, New York, graduating with a Bachelor of Arts in Physics in 1985. Eric received a reserve commission in the USAF in 1985 at the ROTC detachment at Cornell University, Ithaca, New York. Upon commissioning, he served at Hanscom AFB, Massachusetts in the Electronic Systems Division's Strategic Defense Initiative Program Office. While stationed at Hanscom AFB he held a number of positions ranging from Source Selection Executive Officer to Project Manager and earned a Master of Science in Computer Science from Rivier College in Nashua, New Hampshire. In May 1991 he entered the School of Engineering at the Air Force Institute of Technology.

Permanent Address: PO Box 67  
Jacobs Rd  
Westtown, NY 10998

# REPORT DOCUMENTATION PAGE

Form Approved  
OMB No. 0704-0188

Public reporting burden for this collection of information is estimated to average 1 hour per response, including the time for reviewing instructions, searching existing data sources, gathering and maintaining the data needed, and completing and reviewing the collection of information. Send comments regarding this burden estimate or any other aspect of this collection of information, including suggestions for reducing this burden, to Washington Headquarters Services, Directorate for Information Operations and Reports, 1215 Jefferson Davis Highway, Suite 1204, Arlington, VA 22202-4302, and to the Office of Management and Budget, Paperwork Reduction Project (0704-0188), Washington, DC 20503.

1. AGENCY USE ONLY (Leave blank)		2. REPORT DATE 1 Dec 92	3. REPORT TYPE AND DATES COVERED Thesis	
4. TITLE AND SUBTITLE A Two-Dimensional Particle Simulation of Parallel Plate Radio-Frequency (RF) Glow Discharges			5. FUNDING NUMBERS	
6. AUTHOR(S) Eric J. Bennett, Captain, USAF				
7. PERFORMING ORGANIZATION NAME(S) AND ADDRESS(ES) Air Force Institute of Technology Engineering Physics Department WPAFB, OH 45433			8. PERFORMING ORGANIZATION REPORT NUMBER  AFIT/GEP/ENP/92D-1	
9. SPONSORING / MONITORING AGENCY NAME(S) AND ADDRESS(ES) Wright Labs / POOX Aero Propulsion and Power Directorate WPAFB, OH 45433			10. SPONSORING / MONITORING AGENCY REPORT NUMBER  N/A	
11. SUPPLEMENTARY NOTES				
12a. DISTRIBUTION / AVAILABILITY STATEMENT  Approved for public release; distribution unlimited			12b. DISTRIBUTION CODE	
13. ABSTRACT (Maximum 200 words)  A two-dimensional model of parallel plate RF glow discharges was developed to study discharge phenomena important in plasma assisted processing of materials. The particle-in-cell method is used to calculate the trajectories of computer particles under the influence of both self and applied fields. Monte Carlo methods using the null collision technique are used to model collisions between charged particles and neutral gas atoms. Results of computer experiments are presented with special emphasis placed on ion motion in the sheath regions. Experimental results show some qualitative agreement with one-dimensional model results. Further work required to gain quantitative agreement is outlined.				
14. SUBJECT TERMS  Plasma Processing, Radio-Frequency, Glow Discharge, Simulation			15. NUMBER OF PAGES 109	
			16. PRICE CODE	
17. SECURITY CLASSIFICATION OF REPORT  UNCLASSIFIED	18. SECURITY CLASSIFICATION OF THIS PAGE  UNCLASSIFIED	19. SECURITY CLASSIFICATION OF ABSTRACT  UNCLASSIFIED	20. LIMITATION OF ABSTRACT  UNLIMITED	